UNIVERSITY OF CALIFORNIA

Santa Barbara

A Methodology and Analysis of Inoculation in Additive Aluminum Alloys

A dissertation submitted in partial satisfaction of the

requirements for the degree Doctor of Philosophy

in Materials

by

John Hunter Martin

Committee in charge:

Professor Tresa M. Pollock, Chair

Professor Carlos G. Levi

Professor Anton Van der Ven

Professor Frederic Gibou

December 2018

The dissertation of John Hunter Martin is approved.

Professor Carlos G. Levi

Professor Anton Van der Ven

Professor Frederic Gibou

Professor Tresa M. Pollock, Committee Chair

September 2018

A Methodology and Analysis of Inoculation in Additive Aluminum Alloys

By

John Hunter Martin

For Dana and Scarlett

Acknowledgements

The research in this dissertation would not have been possible without the support, whether financial, scientific, or emotional, of multiple people and organizations. I would first like to thank my wife, Dana, and daughter, Scarlett, for their expertly balanced level of encouragement and frustration during this academic journey, producing a uniquely motivating atmosphere at home. I knew that taking on PhD research while working and commuting would be difficult, but Dana was always accommodating to my late nights, busy weekends, and constantly shifting dates on when I thought I would actually be finished. Dana also had an undeniable mark on the content of this dissertation. As an excellent graphic designer, Dana always made herself available to help produce figures for papers and even this dissertation with the expressed stipulation that I not explain anything. This dissertation would truly not be the work it is without Dana.

I would next like to thank my advisor, Tresa Pollock, for taking a chance on accepting me into her group. I came in with a highly unusual methodology of enrollment and a dense schedule that required balancing both work and school. Professor Pollock agreed not only to this, but also allowed me to pursue studies in additive manufacturing which was itself a new area of study in the Pollock group. I complicated this further by wanting to work on aluminum alloys, but Professor Pollock was always encouraging. There are not many advisors who would have agreed to such a mess of a situation, but I feel incredibly lucky to have been a part of the Pollock group at UCSB and have benefited substantially from the mentoring provided by Professor Pollock.

I must also thank HRL Laboratories for the financial and scientific support for this research. HRL offers a program where, as an employee, I could purse an advanced degree while maintaining employment, which is as difficult as it sounds, but an excellent opportunity. This research has been a successful implementation of this program, but that is directly related to the support I received from management and the technical team. I will start by thanking Alan Jacobsen and Bill Carter for initially agreeing to let me pursue this degree along with Leslie Momoda and Bill Jeffery. Though the structure of the company has changed this management support has continued with support from Jake Hundley, Leslie Momoda, Geoffrey McKnight, and Parney Albright. There was also a substantial amount of experimental work completed to support this research. I cannot thank Brennan Yahata enough for his support in experimental operations and analysis during this research. As my office mate, we have had innumerable discussions which have substantially advanced this research. I must also thank Toby Schaedler, Eric Clough, Randall Schubert, Julie Miller, Jake Hundley, and Christian Neuhaus for additional technical support and discussions throughout this research. Additionally, multiple interns at HRL have contributed to this research including Justin Mayer, Robert Mone, and Ekaterina Stonkevitch. I would like to also thank the administrative staff, particularly the legal and export departments, for their help in clearing the many presentations and papers produced during the course of this research.

While much of the material production and analysis for this research was completed at HRL, the research facilities at UCSB were instrumental in capturing many important data sets for this dissertation. Some early experimental work was completed utilizing facilities in the material processing lab with the help and guidance of Deryck Stave. Preparing pure

aluminum for microscopy is not always easy, but luckily Marissa Lafata had multiple recommendations that aided in developing effective polishing routines. I could also not have captured many of the microscopy images in this dissertation without the aid of the microscopy facilities at UCSB. I would like to thank Mark Cornish for initial training on the SEMs and his excellent care of the equipment. I would also like to thank Victoria Miller and Andrew Polonsky for training in collecting EBSD data sets. Patrick Callahan was also instrumental in capturing STEM and TEM data for this dissertation which enabled confirmation of many of the crystallographic driven nucleation predictions. I cannot thank Patrick enough for his expertise in preparing and analyzing some of the aluminum samples for analysis, and helping to provide some critical data sets.

I would next like to thank the remainder of my committee, Carlos Levi, Anton Van der Ven, and Frederic Gibou. I have not always had the most conventional schedule for preliminary and qualifying exams, but you have always been accommodating and available to review the progress of this research. Additionally I would like to thank the Materials department administrative staff for being so helpful.

In addition to the many individuals mentioned above, I would also like to thank the entire Pollock group for their help throughout the years. While, I did not spend a substantial amount of time on campus compared to the traditional graduate student, the Pollock group was always available to have fruitful scientific discussions. The Pollock group is not only a truly remarkable collection of scientists and engineers, but also an excellent group to work alongside. The diversity of projects and technologies being investigate helped me to gain a more complete understanding of material science that would not have been possible without such intelligent and dedicated individuals.

Last, but not least, I would like to thank my parents, whose support throughout the years gave me the multitude of opportunities necessary to reach this point. The values my parents instilled in me have given me the needed determination to pursue this degree and I would not be the person I am today without their guidance. I was never an easy child, but they managed to harness my stubborn determination into a positive academic and post-academic career. I hope to have the same success with Scarlett.

Without the help of these people and organizations, I would not have been able to successfully complete this dissertation. I am eternally grateful for all of their support. This has been an exciting, frustrating, enlightening, long, and rewarding journey and I am happy I was able to share it with such an amazing group of people.

Curriculum Vitae

John Hunter Martin

Education

University of California, Santa Barbara *Santa Barbara, CA* 2014 - 2018
PhD Materials

University of Washington *Seattle, WA* 2005 - 2009
Bachelor of Science, Materials Science and Engineering
Division I Athlete: Rowing

Research Experience

HRL Laboratories LLC. *Malibu, CA* July 2013-Present
Research Staff

- Leader of metal additive manufacturing group, and member of the Materials & Microsystems Lab with focus on improving core competencies in metallurgy
- Developing and enabling new alloy systems for additive manufacturing and other processing routes through control of solidification and microstructure
- Metallic nanoparticle synthesis and functionalization for use in fabrication of high performance bulk metallic materials
- Developed low thermal conductivity and low heat capacity thermal materials
- Assist and advise on metallurgy related questions within the lab

Xtalic Corp. *Marlborough, MA* March 2011-June 2013
Research and Development Engineer

- Worked with small team to develop lightweight nano-crystalline aluminum alloys for high performance applications, including ballistic protection
- Testing, characterization, and analysis of new materials
- Associated scientist with MIT Institute for Soldier Nanotechnology
- Assisted developing small scale processing system as precursor for pilot scale system
- Managed and maintained specialized equipment (2 positive pressure glove box systems, and associated vacuum systems, XRD, metallurgical prep, and micro-hardness testing)
- Member of internal safety committee, developed air sensitive material safety procedures and coordinated HAZOP studies

Modumetal Advanced Nanolaminated Alloys *Seattle, WA*
Project Manager August 2009 - February 2011

- Lead R&D for Corrosion Department; Cadmium and hard chrome replacements
- Coordinated material testing: Corrosion, abrasion, hydrogen embrittlement, fatigue, etc.
- Managed multiple projects simultaneously

Project Engineer June 2009 - August 2009

- Handled product development for single system
- Provided general program support

Lead Research Intern/Mechanical Testing and Verification Intern June 2008 - June 2009

- Developed new alloys and processing techniques
- Mechanical testing of armor materials
- Assisted R&D with PhD Scientists

Teaching Experience

University of California, Santa Barbara *Santa Barbara, CA* Summer 2018
Guest Lecturer: Introduction to Materials; Materials 101

University of California, Santa Barbara *Santa Barbara, CA* Spring 2016
Teaching Assistant: Graduate Kinetics of Materials

Publications

- **J. H. Martin**, B. D. Yahata, J. A. Mayer, R. D. Mone, E. Stonkevitch, J. A. Miller, J. M. Hundley, P. Callahan, and T. M. Pollock, "Grain Refinement Mechanisms in Additively Manufactured Nanofunctionalized Alloys", *In Preperation*
- **J. H. Martin**, B. D. Yahata, E. C. Clough, J. A. Mayer, J. M. Hundley, and T. A. Schaedler, "Additive Manufacturing of Metal Matrix Composites via Nanofunctionalization," MRS Communications, Vol. 8, Issue 2, 2018, pg 297-302,
- **J. H. Martin**, B. D. Yahata, E. C. Clough, R. D. Mone, J. A. Mayer, E. Stonkevitch, R. C. Schubert, J. A. Miller, J. M. Hundley, T. A. Schaedler, and T. M. Pollock, "Recent advances in additive manufacturing of high strength 7000 series aluminum," Adv. Mater. Process., vol. 176, no. 1, 2018.
- **J. H. Martin**, B. D. Yahata, J. M. Hundley, J. A. Mayer, T. A. Schaedler, and T. M. Pollock, "3D printing of high-strength aluminium alloys," Nature, 2017.
- **J. H. Martin**, D. S. Ashby, and T. A. Schaedler, "Thin-walled high temperature alloy structures fabricated from additively manufactured polymer templates," Mater. Des., vol. 120, 2017.
- Z. C. Eckel, C. Zhou, **J. H. Martin**, A. J. Jacobsen, W. B. Carter, and T. A. Schaedler, "Additive manufacturing of polymer-derived ceramics.," Science, vol. 351, no. 6268, pp. 58–62, 2016.

Selected Conference Presentations

- **J.H. Martin**, B.D. Yahata, R.D. Mone, E. Stonkevitch, J.M. Hundley, T.A. Schaedler, T.M. Pollock, "Enabling new additive alloys through solidification control" TMS 2018
- **J.H. Martin**, B.D. Yahata, E.C. Clough, J.M. Hundley, T.A. Schaedler, T.M. Pollock, "Microstructure control in additive manufacturing of aluminum alloys" MS&T 2017
- **J.H. Martin**, B.D. Yahata, T.M. Pollock, "Discovery of new grain refiners utilizing crystallographic data" TMS 2017
- **J.H. Martin**, B.D. Yahata, E.C. Clough, J.M. Hundley, T.A. Schaedler, T.M. Pollock, "Microstructure control in additive manufacturing of aluminum alloys" TMS 2017
- **J.H. Martin**, B.D. Yahata, E.C. Clough, J.M. Hundley, T.A. Schaedler, T.M. Pollock, "Microstructure control in additive manufacturing of aluminum alloys" MS&T 2016
- **J.H. Martin**, E.C. Clough, T.A. Schaedler, "Architected high temperature alloy truss cores" AeroMat 2016
- >10 additional presentations as co-author

Patents

- **JH Martin**, TA Schaedler, BD Yahata, "Spherical nanoparticle hydrides, and methods for making the same" US Patent 9,994,445
- **JH Martin**, JA Kolodziejska, JJ Vajo, JA Graetz, CS Roper "Method of electroless deposition of aluminum or aluminum alloy, an electroless plating composition, and an article including the same" US Patent 9,803,283
- AF Gross, AP Nowak, TA Schaedler, **JH Martin** "Nanoparticle-coated multilayer shell microstructures" US Patent 9,738,788
- TA Schaedler, JM Hundley, **JH Martin**, CS Roper, EC Clough "Curved high temperature alloy sandwhich panel with a truss core and fabrication method" US Patent 9,731,471
- TA Schaedler, AF Gross, AP Nowak, **JH Martin**, JA Kolodziejska "Thermal barrier materials and coatings with low heat capacity and low thermal conductivity" US Patent 9,719,176
- >15 additional pending patent applications

Professional Memberships

The Minerals, Metals, & Materials Society 2014 – Present
Member: Additive Manufacturing Committee
Symposium Organizer: "Additive Manufacturing: Materials Design and Alloy Development," TMS 2019

ASM International 2016 – Present

Awards/Recognition

Edison Award Silver Medalist 2018
"Microstructure Control for High Performance Additive Materials"

Outstanding IR&D Program – HRL Laboratories 2017
Program Principle Investigator

Paper of the Year – HRL Laboratories 2016 & 2018

Principle Investigator: NAVAIR SBIR Contract January 2010 - July 2010
Title/Phase: Innovative Nanolaminated Coating for High Strength Arresting Gear Components, Phase 1, Proposal No. N093-180-0956

Dale Carnegie Leadership Training for Managers January 2010

Volunteer Work

Mentor for Washington High School Aerospace Scholars Summer 2009

Abstract

A Methodology and Analysis of Inoculation in Additive Aluminum Alloys

by

John Hunter Martin

Metal additive manufacturing, or 3D printing, has the potential to be an incredibly disruptive technology for the fabrication and integration of complex components in a variety of industries, ranging from automotive and aerospace to medical devices and sporting goods. Until recently, additive manufacturing of metals was mostly used for non-critical or prototyping applications, however a global push for improved energy efficiency via light weighting and topological optimization, as well as reduced cost via lower material waste and near net-shape fabrication, is pushing metal additive manufacturing out of the prototype stage and into full scale production. This has led to a large investment in development of additive metals technologies, however this has mostly been focused on the improvement of additive equipment with a focus on better repeatability, quality, and throughput. There has been relatively little focus on improvements of the materials which are used in additive manufacturing, which have been limited to a few "weldable" alloy systems such as Al10SiMg, Ti6Al4V, and Inconel 718. While these alloy systems have provided a good first step in development of the additive industry, they are extremely limited when compared to the >5000 different alloy compositions available in either cast or wrought forms. This limitation is driven by the unique processing conditions of additive manufacturing which differ significantly from conventional bulk material production developed over centuries, if not millennia. This dissertation investigates the unique solidification conditions present during additive manufacturing of aluminum alloys and attempts to understand how novel

inoculant methodologies may be used to not only control microstructure evolution of model unalloyed aluminum systems but extend the available alloy systems beyond what was previously considered amenable to the additive process.

The potential scope of additive manufacturing both from a technological and applications space is vast. Therefore, this dissertation is focused on a single additive processing route (laser powder bed fusion) and alloy system (aluminum). Aluminum was chosen after an investigation of available additive alloys indicated that the aluminum alloys, in particular, provided the lowest additive material strength (~200MPa, AlSi10Mg) vs their wrought counterparts (>400 MPa, 7000 Series Al). This is driven by the high crack susceptibility of many high strength aluminum alloys during solidification. It was hypothesized, and has been indicated in the literature, that formation of fine equiaxed microstructures can decrease the susceptibility of these systems to solidification cracking. Until now, microstructure control in additive was limited to parametric manipulation of print parameters, however this has been difficult to broadly implement across all alloy systems. This research leveraged the concept of inoculation to aid in the control of microstructure and improve the processing of additive aluminum alloys. This dissertation has been organized to provide the necessary background information to understand the solidification conditions present in laser powder bed fusion and a methodology for inoculation of additive alloys and mechanistic discussion utilizing a model unalloyed aluminum system. Finally, this dissertation will demonstrate that utilization of this inoculation approach can in fact eliminate the crack susceptibility of high strength aluminum alloys (Al7075 and Al6061) and produce crack free additive aluminum with strengths 2X that of the most common commercial Al10SiMg alloy system.

Table of Contents

List of Figures

List of Tables

Chapter 1

Introduction

Metal additive manufacturing (AM), or 3D printing, has the potential to transform design and fabrication of structural components, disrupting multiple industries[1–3]. During additive manufacturing material is deposited layer by layer to build up a part of arbitrary geometry **(Figure 1.1)**. Conventional processing routes such as casting or machining are limited by process specific design criteria or line of sight manufacturing which limits the potential geometries. Additive manufacturing overcomes these limitations by starting with powder or wire material at a finer scale than the target geometries being built and locally melting or sintering these together to build the component from the ground up. As such nearly any geometry can be created[4].

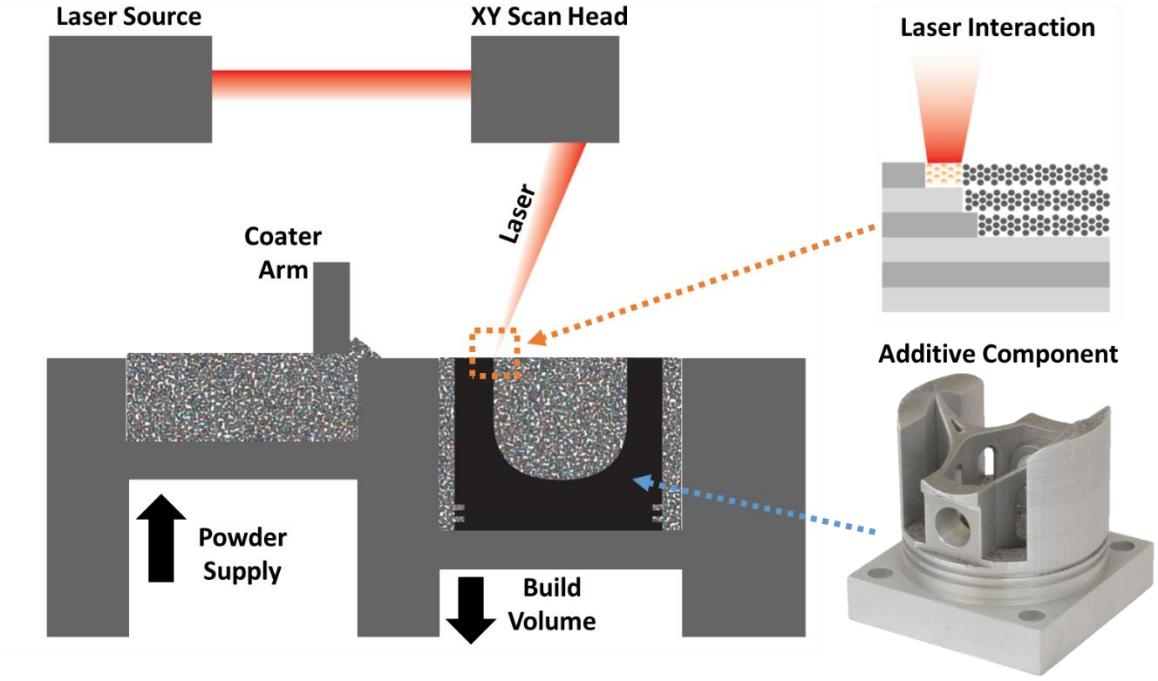

Figure 1.1: Schematic of the Laser Powder Bed Fusion Process. A laser is generated either as a continuous pulsed beam. The most common laser systems generally consist of a ytterbium fiber laser with a wavelength of about 1µm. The laser is emitted into an optical scan head which utilizes a mirror to raster the laser and melt the metal powder at the desired location on the surface of the build volume. The laser melts an individual layer of powder fusing it to the preceding layer. When the layer is complete the build volume descends by one layer height and the powder supply elevates by at least one layer height (sometimes more depending on the dosing factor). A coater arm then pushes the powder from the powder supply to the build volume and spreads a uniform layer of powder to prepare for melting of the next layer. This process repeats until the build is complete. The build volume is raised up and excess powder is removed to reveal the final additive component.

Additive manufacturing was originally developed and patented by Chuck Hull in 1984 and commercialized by 3D Systems Inc. for production of plastic components[5]. This technology used a UV light source to locally cure photosensitive resin layer by layer building a final part. While a revolutionary manufacturing methodology, the materials were originally relegated mostly to prototype fabrication. The software developed to enable the first additive manufacturing, namely the ability to slice 3D drawings into 2D images which can be converted into laser curing paths, was extremely important to the early development of the technology. The "stereolithography" file format, or STL, was developed for 3D Systems as a way to convert computer-aided designs (CAD) into triangulated surface

geometries which could be represented in a simple text form and simply processed into laser paths for each layer[6]. This was subsequently applied to selective laser sintering, where plastic particles where directly sintered into a final part, similar to **Figure 1.1**. Carl Deckard and Joseph Beaman, at the University of Texas, then applied this technology to sintering metal powders in 1989, which began the development of metal additive manufacturing[7].

While historically used as a prototyping technology, recent advances in machine and material quality has changed this dynamic, enabling a new manufacturing route for components with optimized geometries, lower material usage, and enhanced part performance. The opportunity to use additive manufacturing industrially is driving a large increase in investment and the expected market for additive alloy systems is expected to grow significantly in the next 10 years. This is particularly true for additive aluminum alloys, where the demand for lightweight high strength aluminum is expected to increase, along with the diversity of industries currently interested in additive manufacturing, **Figure 1.2**.

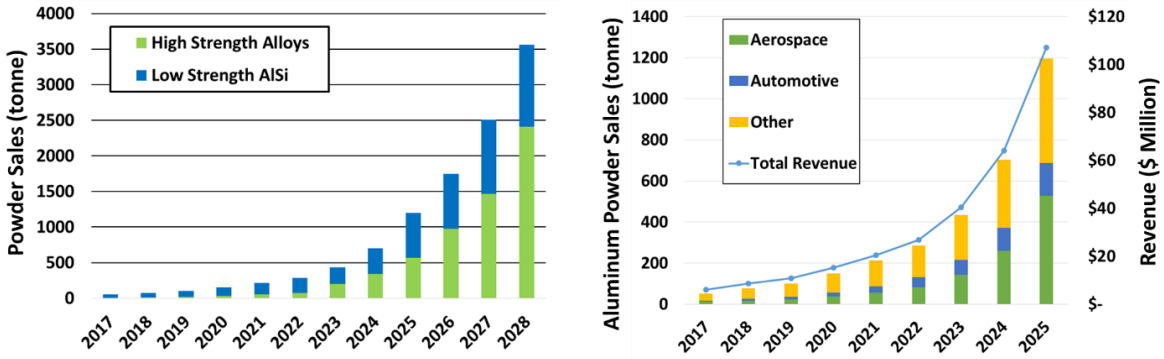

Figure 1.2: Market Trends in Additive Aluminum Alloys. **(Left)** Expected demand for additive aluminum alloys. **(Right)** Expected demand for aluminum alloys by industry and the expected trend in market size. The demand for high strength (i.e. 7000 & 2000 alloys) is expected to increase substantially. This is driven by an increased need in the aerospace industry, however the automotive industry will likely increase as well due to increasing fuel economy regulations. Other industries include recreational sports and tooling which are also expected to increase substantially in their use of additive aluminum alloys[8].

There have been multiple high profile reports related to the advantages of additive manufacturing, with potential benefits including part count reduction and simplification in design, demonstrated by GE Aviation's fuel injector nozzle[9], weight reduction in Airbus's door bracket redesign with topological optimization[10], and material reduction with Boeing's titanium fabrication[11]. Of note is that metal additive manufacturing success stories have been mostly related to the aerospace industry where weight reduction is of key importance. These early applications do not yet indicate that additive, as a manufacturing process, is fundamentally changing general approaches to manufacturing[12]. There remain many obstacles to broad adoption of the additive process, including defect inclusion, surface finish, and the suite of "printable" alloys[13–16]. The latter is of particular interest to this research effort as the number of available alloys is significantly limited (**Figure 1.3**)[3,17,18]. This is related to the relative age of the technology, current industrial need, and the unique processing conditions of additive manufacturing, which are incompatible with many alloy systems.

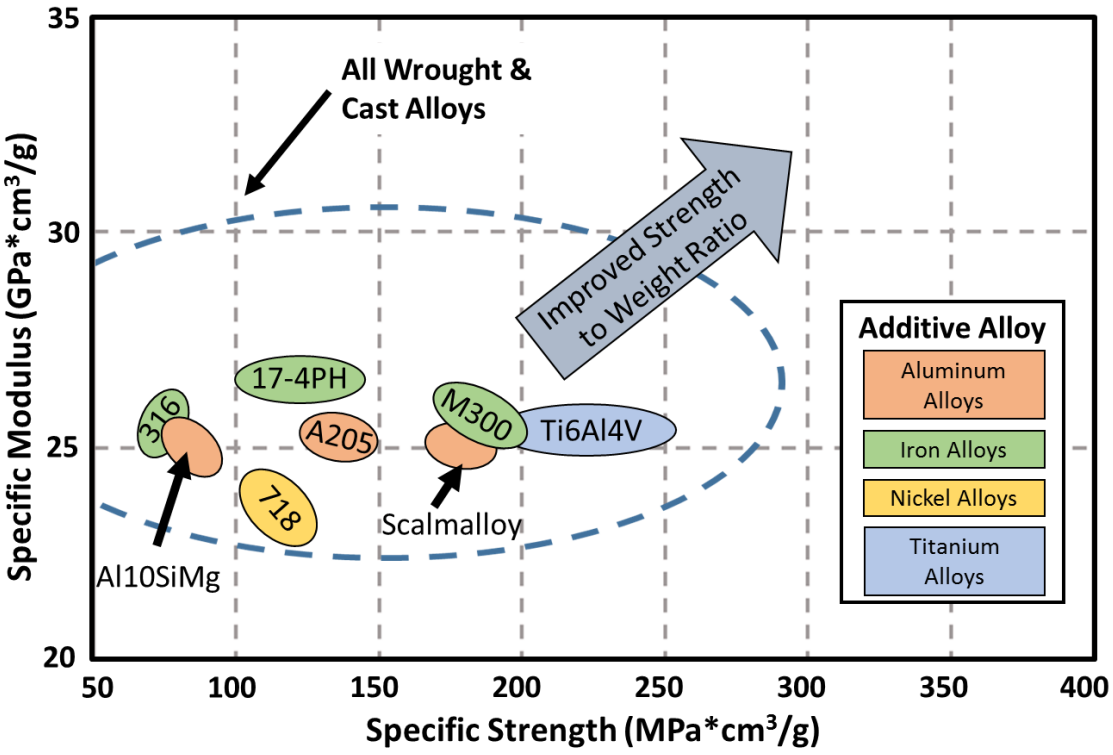

Figure 1.3: Specific Properties of Additive Alloys vs Conventionally Processed Alloys. Material properties of all wrought and cast alloy systems is based on an evaluation of common material properties in the Materials Handbook Desk Edition[19]. Additive alloy material properties are based on an evaluation of reported material properties in the Senvol Additive Materials database[20] and openly available information on A205 development[21,22].

The aluminum alloy systems are of particular interest for this dissertation. The demand for high strength additive aluminum is expected to increase exponentially[8] (**Figure 1.2**), but the only moderate to high strength options are A205[21] and Scalmalloy[23](**Figure 1.3**), both of which rely on high cost alloying elements (silver and scandium, respectively)[22]. The development of these alloys has been driven by the need for aluminum alloy systems that can accommodate the additive process. Typical high strength wrought aluminum alloys of the 7000 and 2000 series with yield strengths >400 MPa are not readily amenable to the additive process, due to cracking during solidification[22,24,25]. The cracking phenomenon during solidification of high strength aluminum has been known for over a century and is attributed to the composition of these

alloy systems[26–28]. In order to overcome the cracking issue it is hypothesized that controlling the microstructure during solidification can eliminate the cracking phenomenon. In order to accomplish this in additive manufacturing, this dissertation will investigate the solidification pathways in additive manufacturing along with inoculation methodologies to exert control over solidification in metal additive manufacturing.

1.1 Types of Metal Additive Manufacturing

Metal additive manufacturing has evolved significantly over the past decade and can now take many different forms. The specific method of additive manufacturing can have significant impacts on the material properties and geometric tolerances possible with the different techniques[2,3,18,29]. The former is dominated by the energetic mechanism used to fuse the material while the latter is controlled by the smallest dimension of the feedstock and method by which the material is added to the build area. **Table 1.1** provides a list of the most common additive techniques along with a brief description of each technique.

Table 1.1: List of Common Metal Additive Manufacturing Processes[30]**.**

ASTM Description	Other Common Names	Feedstock Form	General Description
Binder Jetting		Powder	A write head selectively drops a binder to stick particles together in the final shape of the component. After binding the excess powder can be removed, a de-binding step occurs and the green part is sintered
Directed Energy Deposition (DED)	Laser Engineered Net Shaping (LENS), Electron Beam Freeform Fabrication (EBF^3)	Powder, Wire	Powder or wire is fed our of a nozzle and locally melted by a laser or electron beam and the part is build up by successive passes of the feed nozzle
Material Extrusion	Fused Deposition Modeling (FDM), Fused Filament Fabrication (FFF)	Powder in a Thermoplastic Binder	A thermoplastic filament with metal powder is extruded through a heated nozzle. After the part is build, a de-binding and sintering step occur.
Material Jetting	Robocasting, Direct Ink Writing (DIW)	Paste or Suspension	A nozzle extrudes a paste or suspension of particulates and is then sintered.
Powder Bed Fusion (PBF)	Selective Laser Sintering (SLS), Selective Laser Melting (SLM), Direct Metal Laser Sintering (DMLS), Electron Beam Melting (EBM)	Powder	A layer of powder is spread over a build plate and a laser or electron beam locally melts or sinters the powder together based on the component geometry for the given layer. This is repeated with successive powder layers until the build is complete.
Sheet Lamination	Ultrasonic Consolidation (UC), Ultrasonic Additive Manufacturing (UAM), Laminated Object Manufacturing (LOM)	Sheet or Foil	Sheets or foils are fused to preceeding layers through ultrasonic heating. Layers may be pre-cut to shape or only local fused and excess un fused material can be removed after the build is complete.

While many of the manufacturing techniques listed in **Table 1.1** are industrially available, this dissertation is mainly focused on the Selective Laser Melting (SLM) process, which is currently the most common metal additive manufacturing process. During this process, shown schematically in **Figure 1.1,** a thin layer of powder is spread from a powder supply piston to the build piston where a laser selectively melts the powder to fuse the material to the previous layer, building up a complex geometry part. The laser power can range from 50-1000W and is generally a Yb-Fiber laser with a spot size between 50-200µm[31]. The laser systems typically have a wavelength of approximately 1070 nm and melt the metal through energy absorption. The amount of absorbed energy is directly related to the metal absorptivity at the applied wavelength and the power of the beam. Material type, as well as, particle and melt-pool geometry can impact the amount of energy absorbed and therefore the thermal behavior during melting and solidification[32]. Faceted powders can act as mirrors reflecting more energy. Additionally higher applied energy forms a

deeper melt zone, creating a cavity for which reflected radiation is not reflected out of the melt-pool but instead reabsorbed by the adjacent molten metal[32]. The laser must raster back and forth over an area to completely melt the layer to the target geometry. Multiple strategies on how this is accomplished exist. This most common strategies and input parameters are shown in **Figure 1.4**, however novel strategies beyond this have been developed including discrete point melting[33] and fractal scanning[34].

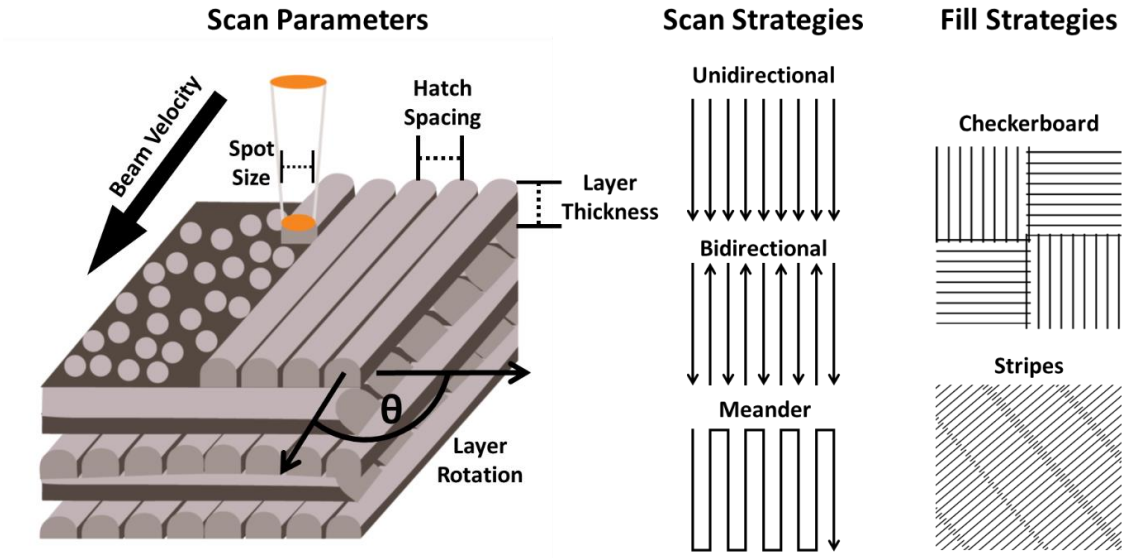

Figure 1.4: Schematic of Common Scan Parameters and Strategies used During SLM. The scan parameters dictate the amount of material which is melted or re-melted in each pass of the laser. The Scan and Fill Strategies impact the thermal build up during processing. In unidirectional and bidirectional scanning the laser power is turned off between each pass while the meander strategy keeps the laser on. The Fill strategies have some overlap with the adjacent filled area to ensure each area is fused to the adjacent. Multiple different strategies can be implemented throughout the build and these can be changed even within the same layer depending on the input parameter files.

During this process multiple parameters are controlled including but not limited to layer thickness, scan overlap, beam speed, and scan path. This provides a nearly infinite number of processing parameter combinations for which the additive process can be utilized. Due to the layer by layer process, parameters are optimized to increase the processing speed while still fully fusing the material with a minimal amount of defects. Although the selective laser melting process is described here, many of the same parameters are important

for all the additive processes listed in **Table 1.1**. However this work will focus solely on the selective laser melting approach.

The idea of a rastering energy source locally melting and fusing metal together is not new. Welding and brazing with local directed energy sources have been utilized for centuries[35]. As such, many of the constraints observed in welding are applicable to additive manufacturing, including solidification and stress induced cracking[36–38]. This has limited the available additive alloys to those which are considered "weldable" without the aid of filler metals[18]. Overcoming these limitations will enable a drastic increase in the available alloy systems for additive manufacturing, as well as enabling lower cost higher strength alloy systems.

1.2 Conventional Manufacturing vs Additive Manufacturing

Additive technology is fundamentally different from conventional manufacturing technologies which have remained relatively unchanged for millennia, including casting, forging, and machining. In casting, liquid metal is poured directly into a mold resembling the target component shape. Forging requires cold or hot working of the material to deform the raw material into a final shape. Machining is often applied to both cast and forged components as well as raw ingots to add precision features by removing excess material using either cutting or grinding tools. Each of these techniques can produce high quality parts for a variety of industries. Additionally, the thermomechanical effects and range of microstructures and properties of these processes are relatively well defined along with the fundamental limitations.

1.2.1 Cast vs Wrought Aluminum Materials

The combination of materials, properties, and accessible processing parameter space ultimately limits all processing approaches systematically decreasing the types of alloys and geometries which can be produced in each process. Casting alloys have specific restrictions on wall thicknesses to accommodate solidification shrinkage, gravitational and flow effects, as well as accounting for any slag and other defects which may be incorporated in the liquid metal[39]. This results in casting molds with varying complexity depending on the final geometry. Multiple risers and gates may be required to accommodate the final geometry and can require significant post-casting machining. Furthermore there are limitations in the types of alloys which can be cast. Casting alloys typically have a short solidification range to reduce the tendency for cracking and hot tearing, a phenomenon which will be discussed more in Chapter 5.

Alloy systems with large solidification ranges are generally processed as wrought alloys which can be forged or machined to produce the final geometry[40]. Wrought alloys can start as a cast ingot but undergo thermomechanical processing to produce a final high strength polycrystalline material. Wrought alloys are given unique designations for the amount of work-hardening imparted as well as any associated heat treatments. These controls have been codified over decades of analysis and provide designers with a known set of boundary conditions for both component geometry and physical properties. Wrought alloys can then be forged or machined into a final component. In many cases wrought alloys can also be heat treated to change the mechanical properties of the material at the end of the processing path. Multiple tempers exists for both wrought and cast materials[40].

The availability of thermomechanical processing for wrought materials means the available alloy compositions can be extremely broad. Additionally more complex microstructures are possible, which can enhance strength beyond that of many casting alloys. However the required post-processing with forging and machining can limit the achievable geometries of the final component. Certain geometries, such as thin walls, are often difficult to forge due to the elongation required in the material to form without cracking[41]. This has been solved for some very specific alloy compositions where deep draw forming[42] and superplastic deformation[43] are possible. Additionally, due to the force required to deform the material, certain overhang and other intricate geometries are difficult to produce without highly specialized tooling. In most cases these features are added after forging by machining applications.

Machining has advanced significantly in recent decades with improved computer aided tool design and new cutting tools such as diamond end mills[44]. Unfortunately many of the fundamental geometric limitations still remain. Mainly, in order to remove a portion of material, a cutting tool must be able to access the area for removal. This can range from highly difficult with multiple tool set-ups required to functionally impossible. The increased use of computer aided topological optimization in the design of geometrically complex component with enhanced strength to weight ratios, tends to create geometries which are extremely difficult and/or costly to machine[4].

1.2.2 Additive Manufacturing

Additive manufacturing provides a route to complex geometries without the fundamental geometric limitations of machining. The layer by layer process, when combined with removable support structures or leveraging the support of the powder bed

(**Figure 1.5**), can produce large overhangs or nearly closed porosity[4]. After completion of the build, supports can be broken off and residual powder can be removed leaving a final complex geometry.

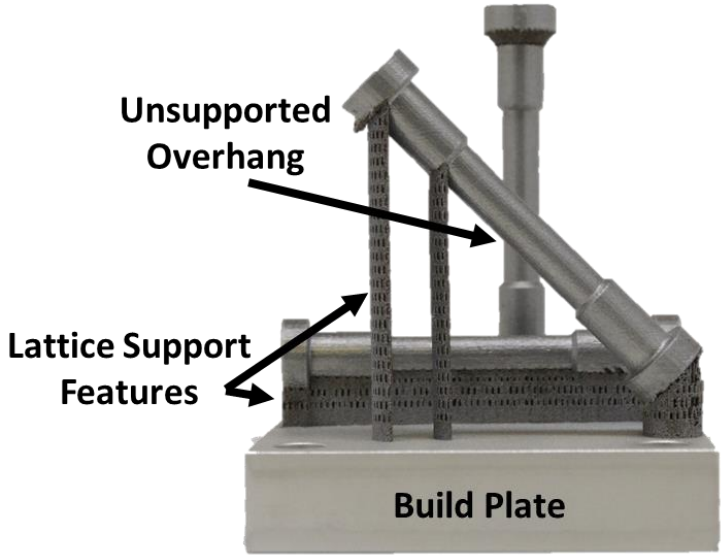

Figure 1.5: Example Additive Build with Supports. These standard tensile coupons were produced from Al10SiMg on a Concept Laser M2 system using the provided CL31 parameter set. They were built at 3 orientations, X, Z, and 45°, to highlight different support strategies. The lattice supports shown allow for easy removal with a band saw and then the surfaces can be cleaned up using grinding of conventional machining. Long overhangs, as in the XY specimen, require full support, while overhangs ≥45° (as shown in above) to the build plate can typically be processed without supports.

While additive manufacturing is often described as a process with full geometric freedom this is not entirely true[45]. While processing the material is being locally heated and melted, therefore the shrinkage and stress associated with this type of processing must be accounted for. In some cases, areas of the build can accumulate large residual stresses which can fracture support structures, the part, or even the build plate, resulting in a component that is a different geometry than desired. Different scan strategies (**Figure 1.4**) along with build heating have been proposed to reduce the accumulated thermal stress[46–48]. Build heating, either through direct resistive heating of the build plate or scanning of the build volume with the energy source (laser or electron beam), lowers the thermal

gradients during solidification and decreases component distortion[1]. Build plate heating can also avoid or induce deleterious phase formation, which may impact mechanical properties or induce residual stress if the associated phase formation has a large volumetric change[49]. While solving the residual stress issue is not directly addressed in this work, controlling the microstructure during solidification can impact the amount of retained residual stress and plasticity of the built part, potentially minimizing this effect.

This dissertation focuses on the alloy limitations of additive manufacturing. As with casting, and by extension welding, the part produced is in the final/near-final geometry and any wrought type processing steps cannot be completed to alleviate any solidification issues without changing the as-built geometry. Furthermore there is limited thermal post processing which can introduce new microstructures, as with wrought alloys, resulting in limited control over the final material properties. Additive manufacturing therefore requires alloy systems that are both highly crack resistant and solidify in the ideal final microstructure for the final component requirements.

1.3 Process-Structure-Property Relationships

Understanding the process-structure-property relationship of any material and manufacturing technique is extremely important to understanding how a material will behave in service. Every material will behave differently when subjected to an applied process, producing a different microstructure, which in turn leads to different material properties. Microstructure driven variations in properties can affect everything from corrosion, strength, fatigue, and fracture toughness. As described above, conventional processes and materials have required decades, in some cases centuries, to define these relationships to produce highly repeatable and predicable material properties. Additive

manufacturing is a fundamentally new process, but many of the lessons learned in developing these relationships for other processes can be applied to that of additive manufacturing.

Described with more detail in Chapter 2, the microstructure of a solidifying material can be controlled by manipulating the thermal gradients and solidification velocity (**Figure 1.6**)[50,51]. This directly impacts the type of grain structure in the final component, and whether it assumes a columnar or equiaxed morphology. The former is more susceptible to cracking[52–54], while the latter provides improved isotropic properties[55]. Additionally, decreasing the size of the grains can result in increased ambient temperature strength due to the Hall-Petch effect[56].

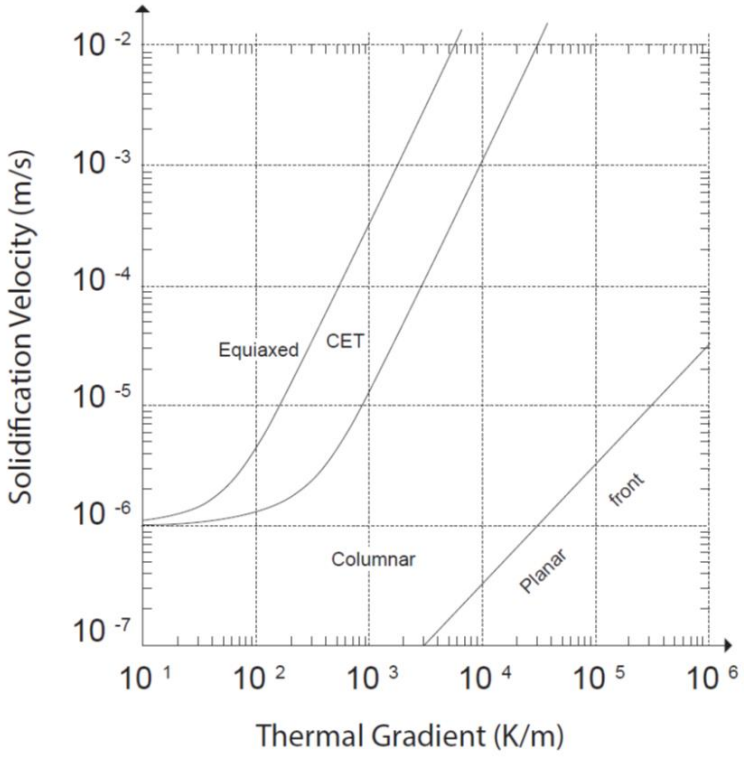

Figure 1.6: Solidification Velocity and Thermal Gradient Microstructure Map. Controlling the solidification velocity and thermal gradient can induce a columnar to equiaxed transition (CET). Additive manufacturing has a high thermal gradient due to a point energy source typically inducing a highly columnar microstructure. Figure adapted from Dantzig and Rappaz[51].

Parametric control of microstructure has been highly investigated recently due to the large number of variables available in additive manufacturing[57,58]. A list of common parameters which can be manipulated are outlined in **Table 1.2**. This is not meant to be a complete list and evolving machine configurations and print modalities continue to expand this list. Additionally these are used cumulatively to design a scan strategy and may be manipulated spatially during component fabrication to produce a variety of thermal conditions depending on part geometry. The parameters shown in **Table 1.2** are mostly continuous variables, in that they can be adjusted to several significant figures independent of each other, providing a nearly infinite number of parameter permutations, it is therefore conceivable that an infinite number of potential solidification paths exists.

Table 1.2: List of Common Variables in Powder Bed Fusion Processes.

Beam Controls	Atmosphere	Machine Configuration	Material Constraints
- Power - Speed - Spot Size - Scan Strategy - Fill Strategy - Hatch Overlap - Fill Overlap - Contours - Layer Rotation - Exposure Sequence	- Gas Type (e.g. Argon, Nitrogen) - Gas Purity (e.g. O_2 & H_2O impurities) - Gas Flow Velocity - Laminar vs. Turbulent Flow - Filtration Rate	- Layer Thickness - Build Volume Size - Build Plate/Volume Temperature - Coater Speed - Coater Type (Roller vs Wiper)	- Composition - Particle Size Distribution - Particle Shape Distribution - Absorptivity

Parameter based solidification control has been described by Dehoff et al. (2015)[58], and process structure maps, focused on power and velocity, are beginning to be developed by Beuth et al (2013)[57]. These are highly important studies and indicate the potential control possible in additive manufacturing. Unfortunately the applicability of these mappings to arbitrary geometries has been difficult. The design of a specific thermal condition, and therefore specific parameter set, is highly dependent on the associated

thermal condition in the build. As the geometry of the build changes, the heat conduction paths change, resulting in different thermal gradients and solidification velocities. This requires a complex and computationally expense parameter set, custom designed to each material and build.

The casting industry has implemented microstructure control over arbitrary geometries for decades utilizing a variety of mechanisms, including inoculation[39,55]. In the case of inoculation, targeted nucleant particles are incorporated in the melt and dominate the solidification mechanism resulting in a relatively uniform microstructure that is controlled primarily by the material input rather than the thermal conditions dictated by the casting mold geometry[39,59].

This research in this dissertation investigates mechanisms by which the inoculation methods of casting can be implemented to improve the microstructure control of additively manufactured metals. This will focus on additive aluminum alloys. Initial studies will focus on understanding the solidification conditions in additive (Chapter 2). The solidification conditions, as will be discussed, can be extremely dynamic and have many unique features including complex fluid flow, short liquidus dwell times, and multiple melting and re-melting stages[60]. This will be followed by methods to identify and introduce inoculants in the additive process, in which common methodologies for identification of inoculants are discussed along with a new adapted methodology for inoculant discovery (Chapter 3). Analysis of the efficacy of inoculant discovery will be completed on additively manufactured pure aluminum to determine the effectiveness of different inoculants (Chapter 4). This research will conclude by applying this process to crack-susceptible wrought aluminum alloy compositions to demonstrate applicability to multi-component alloy systems

(Chapter 5). This research will demonstrate that inoculation can be applied to additive manufacturing to improve the microstructure control beyond the parametric approach and enable an increase in the available alloy composition processing space.

Chapter 2

Solidification Behavior in Additive Manufacturing

The most common forms of metal additive manufacturing utilize some form of metal fusion of powder or wire feedstock, either by a laser or electron beam source (**Figure 2.1**) where the feedstock material is locally melted and fused to the preceding layer[3]. The resulting material properties are therefore dominated by the microstructure which forms during the melt and re-solidification process[58,61]. As such, a complete understanding of the solidification physics is required to begin to understand and control the process-structure-property relationships of additively manufactured metals. While thermodynamic and kinetic models can be developed to describe a multitude of alloy systems, aluminum alloys will be the focus of this chapter for ease of discussion.

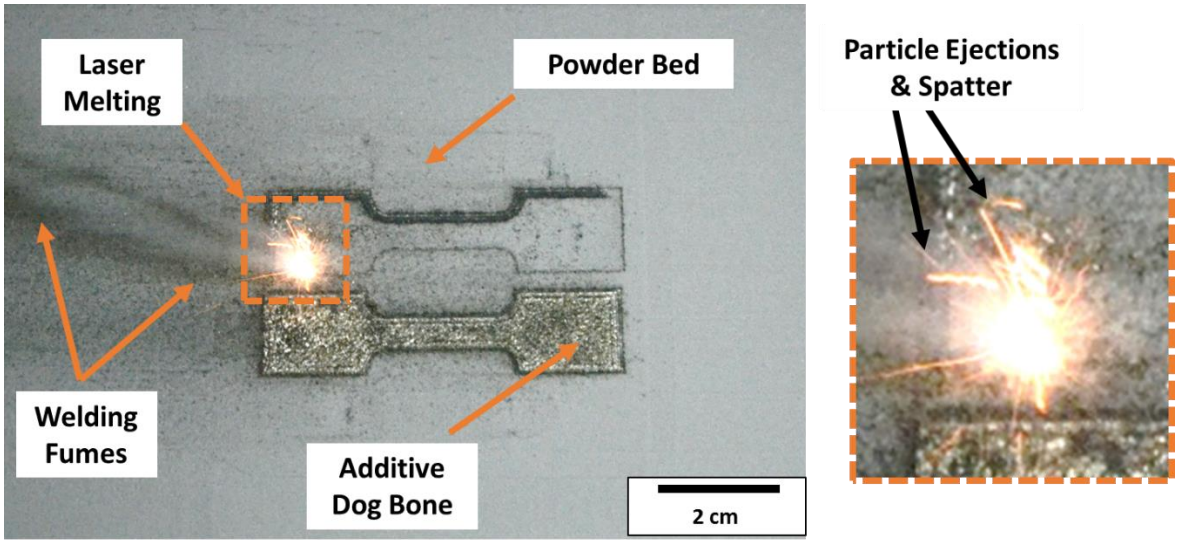

Figure 2.1: Optical image of metal additive manufacturing in process. Taken during selective laser melting of an aluminum alloy in a Concept Laser M2 indicating a highly dynamic process with particle ejections from the melt-pool a large amount of welding fumes, and high thermal gradients based on the local glow of the melt-pool during processing.

The aforementioned fusion based additive manufacturing processes start with a solid metal feedstock, melt the material, and then re-solidify into a consolidated component. The initial phase transformation from solid to liquid is undoubtedly important for the development of a stable melt-pool and establishing the associated thermal gradients and fluid flow prior to the solidification event[57,62–64]. While melt-pool formation and stability will have an impact on the solidified microstructure, their impacts can be considered independently of the entire solidification event. This chapter will focus on solidification as an independent event with the impact of factors such as initial melting, melt-pool shape, and re-melting effects, generally illustrated, but not explicitly derived. The focus of this work is not to fully capture all aspects of the additive process but provide insight into how a comprehensive understanding of solidification can aid in the microstructure control of metallic components synthesized by laser additive approaches.

2.1 Solidification Phase Transformations

Solidification is a first order phase transformation evident by a discontinuity in the derivative of the free energy curves[51]. For a simple single component system, the free energy of the solid and liquid phase can be simply plotted as a function of temperature (**Figure 2.2**). The melting point of a material occurs at the intersection of the solid and liquid free energy curves indicating the change in free energy between the two phases is zero. There is however a non-zero change in both enthalpy and entropy known as the heat of fusion (H_f) and entropy of fusion (S_f), $\Delta G = \Delta H - T\Delta S$. Moving up in temperature along the solid free energy curve, when the melting point intersection is reached the lowest free energy state becomes the liquid phase. Thermodynamically the system is always trying to minimize the total free energy and is therefore driven to undergo a phase transformation

with the melt absorbing the associated heat of fusion. The same occurs during solidification moving down in temperature along the liquid curve resulting in a release of the heat of fusion at the point of solidification. At relatively small undercooling, the free energy curves can be approximated as linear. This combined with the thermodynamic requirement at the phase change $\Delta G = 0$, provides a mathematical estimate for the ΔG_f where $\Delta G_f = dS_f = dH_f/T_m$.

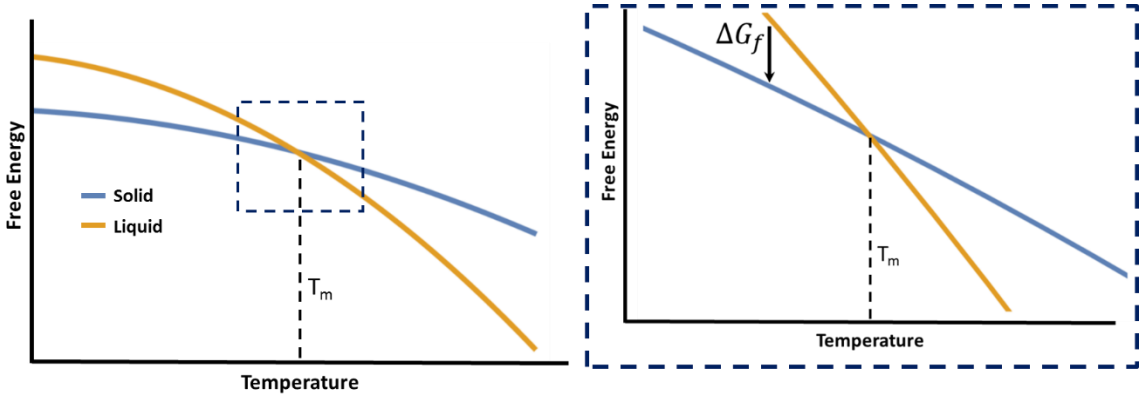

Figure 2.2: Notional Free Energy vs. Temperature Plot for a solid and liquid. (Left) A generalized curve over a large temperature range. (Right) A subset indicating that a linear approximation of the free energy curves can be approximated given a small temperature range as highlighted in Richard's Rule.

This simple description would seem to indicate that once the melting point is reached a phase transformation will occur, however this is not the case and at least some undercooling is required to initiate solidification[50,51]. In some highly controlled experiments material can be chilled to >100K below the melting point before initiating a solidification event[65]. This indicates the fundamental importance of the initial nucleation event. In the absence of a seed crystal or site, nucleation is considered homogenous and occurs via random vibrational rearrangement of atoms until a cluster of organized atoms reaches a critical radius to initiate growth[51,66]. This is the critical radius, and can be calculated using classical nucleation theory in which the total energy of the solidifying system is

$$\Delta G = {}^{4}/_{3}\,\pi r^3 \Delta g + 4\pi r^2 \gamma_{sl} \qquad (Eq\ 2.1)$$

where Δg is the bulk free energy driving force and γ_{sl} is the solid liquid interface energy. The free energy is approximated as $\Delta g = (\Delta T * H_f)/T_m$, where H_f is the heat of fusion, T_m is the melting point of the material, and ΔT is the undercooling. This evolves from the linear approximation shown in **Figure 2.2** where increased undercooling results in increased free energy driving force. The creation of a new interface has an associated energy penalty and therefore requires some additional energetic driving force. As the temperature decreases the change in free energy increases (**Figure 2.2**), while the surface energy remains relatively constant. As such, increasing the amount of undercooling decreases the critical radius (**Figure 2.3**). The calculations here are for pure aluminum and values used for calculations here and in subsequent figures are noted in the Appendix**.**

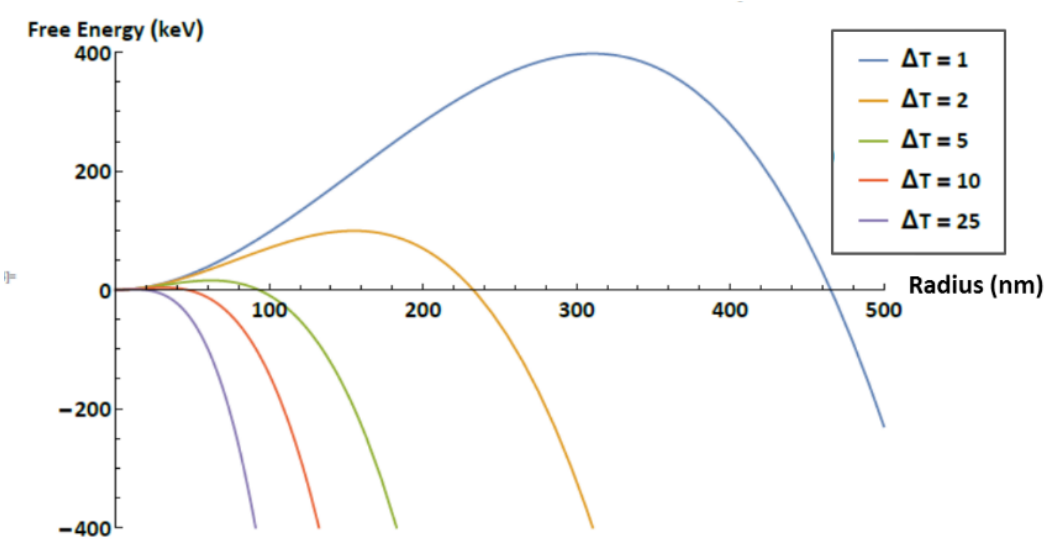

Figure 2.3: Free energy as a function of radius for aluminum solidification. Increasing the undercooling increases the volumetric free energy driving force for nucleation decreasing the energy barrier to nucleation from the surface energy barrier. Units for ΔT are in °C.

Homogenous nucleation in many materials indicates that substantial undercooling for solidification is required, however this is rarely observed in conventional processing. The nucleation event is generally heterogeneous, in which a secondary particulate or mold

surfaces are present in the melt which can initiate the solidification at a reduced energy penalty, decreasing the required driving force for nucleation and subsequent need for high undercooling (**Figure 2.3**)[67]. These secondary particulates can arise from a variety of sources ranging from undissolved intermetallic compounds to impurity particles from the processing environment. Determining the effect of nucleation on microstructure (e.g. columnar vs. equiaxed) requires an understanding of the nucleation rate, which is related to the thermal conditions and the number density of nucleation sites[67,68]. For most solidification calculations a number density of nucleants is assumed depending on the material and processing conditions (casting, arc melting, welding, etc.). In the absence of targeted additions of particulate, the typical nucleant densities can range from $10^5/m^3$ to $10^{10}/m^3$ and are used mainly as a calibration factor in determining the columnar to equiaxed transition[69,70]. Explicitly controlling this number density through inoculation is a common practice in casting and will be discussed further in this as well as other chapters[39].

Heterogeneous nucleation does not change the critical radius of nucleation but decreases the total free energy barrier required to initiate the phase transformation (**Figure 2.4**). In classical nucleation theory, the change in free energy is related to the wettability of the nucleant particle by the equation $\Delta G_{het} = \Delta G_{hom} \cdot f(\theta)$, where[51]

$$f(\theta) = \frac{2 - 3\cos\theta + cos^3\theta}{4} \quad (Eq\ 2.2)$$

Here, θ is the contact angle of the liquid on the solid substrate and varies between 0 and 1 from fully wetting to non-wetting (**Figure 2.5**). Therefore, heterogeneous nucleation sites with high wettability can significantly reduce the energy barrier to nucleation at a given radius. This has the added benefit of decreasing the total volume of material which must

organize to induce the volumetric free energy change increasing the kinetic likelihood of the nucleation event occurring. As will be discussed throughout this dissertation, additional effects from lattice strain can further alter this nucleation barrier and critical undercooling. Typically the calculations for nucleation rely solely on the aforementioned linear analysis of the free energy diagrams and are focused on the entropy or enthalpy of fusion. This, however, neglects other well-known contributions to free energy including strain. These effects are not included in the analysis of the free energy driving force for nucleation and instead assumed to either be negligible in impact or captured in the wetting angle of the substrate. This is a large over simplification which fails to fully account for the total free energy impact on nucleation.

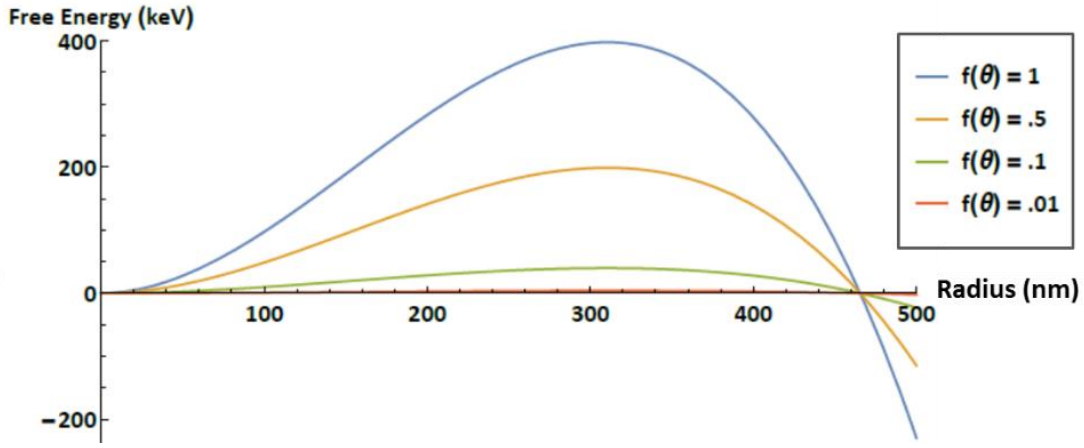

Figure 2.4: Impact of particle wetting on the energetic nucleation barrier. Increasing the wettability of the heterogeneous nucleation site, i.e. decreasing the value of f(θ), can have a large effect on the nucleation energy barrier, but does not change the critical radius.

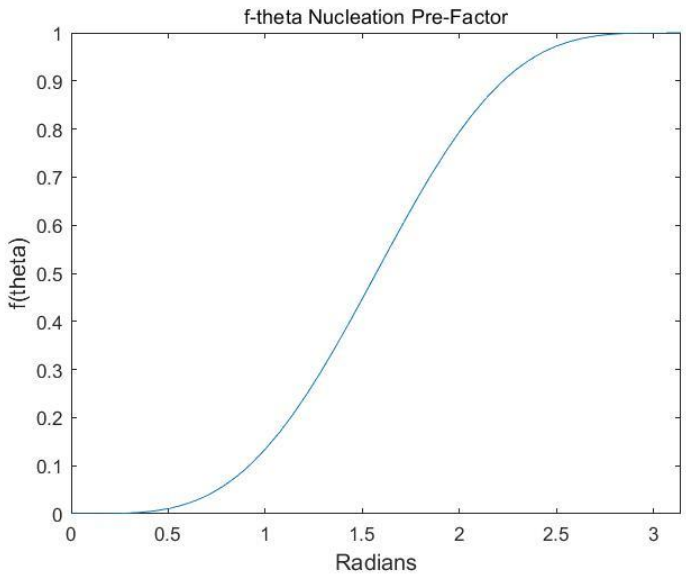

Figure 2.5: Value of f(θ) vs wetting angle.

2.2 Constitutional Supercooling and Microstructure Evolution

The previous description of solidification was simplified to a single component system. However, the goal of this work is to process alloy materials which may consist of a variety of secondary alloying elements. It is therefore important to understand how the presence of solute may impact nucleation and growth as well as the solidified microstructure. One of the most common alloying elements for aluminum is copper[71], the phase diagram for which is given in **Figure 2.6**. Unlike the diagram in **Figure 2.2** this is structured as temperature vs composition and is determined by the free energy curves of the individual phases. Given that aluminum-copper alloys are typically hypoeutectic (less than 33 wt% Cu), understanding this solidification behavior will provide significant insight into other aluminum alloys which are also generally hypoeutectic alloys of Mg, Zn, Mn, and combinations thereof.

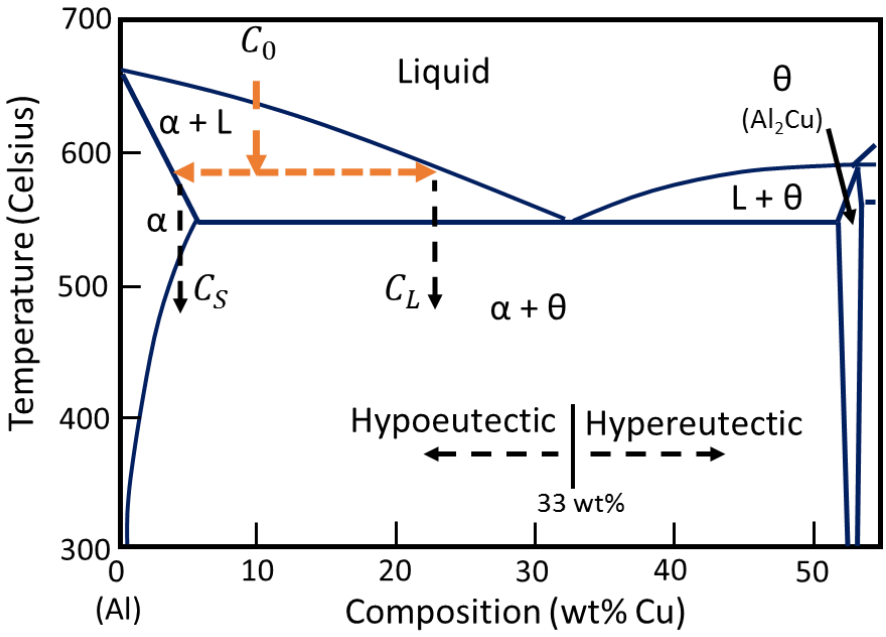

Figure 2.6: Al-Cu Binary Phase Diagram. Shown is the aluminum rich region of the phase diagram indicating a typical binary eutectic phase diagram[72,73].

In cooling a liquid with a hypoeutectic composition on the Al-Cu phase diagram the first phase boundary crossed is from a liquid to a two phase solid-liquid region (orange arrow). Thermodynamically the formation of a solid phase is preferential, but at a different composition than the initial liquid composition. Consequently this results in a rejection of solute into the liquid to form the associated solid composition. Assuming no diffusion in the solid and complete mixing of the rejected solute in the liquid, the composition can be calculated using the Scheil-Gulliver equation[35,39]:

$$C_s = kC_0(1 - f_s)^{k-1} \quad (Eq\ 2.3)$$

where C_0 is the initial composition, f_s is the fraction of solid, and C_s is the composition in the solid which can be related to the liquid composition by the partition coefficient, $k = C_s/C_L$. Under continuous cooling conditions in a closed system, it can be extrapolated that the solid fraction will continue to increase with continued rejection of solute until the liquid reaches the eutectic composition. This is apparent when utilizing a Scheil simulation where

the solid fraction vs temperature is plotted by sequentially stepping down in temperature from a liquid state and recalculating the aforementioned equation. This is shown for two different aluminum alloy compositions in **Figure 2.7**, indicating how changes in composition can change the solidification behavior. This can additionally be shown across the entire hypoeutectic Al-Cu system (**Figure 2.8**). The shape and solidification range of these materials has profound impact on the resulting crack susceptibility of the material, as will be discussed in Chapter 5.

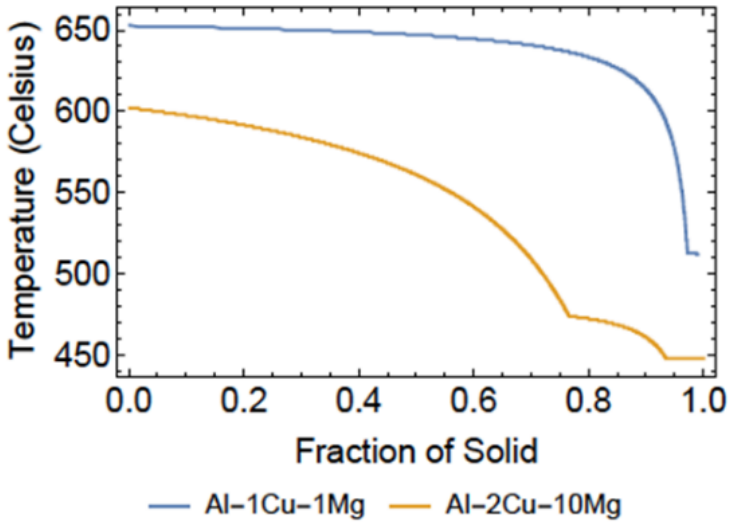

Figure 2.7: Scheil simulations of two aluminum alloy compositions. With minor alloying additions (blue) a high solid fraction of material solidifies under a small temperature range, but rejects solute which solidifies at a much lower temperature resulting in a large solidification range at the high solid fractions. With greater amounts of solute (orange) the material still solidifies over a large temperature range but does so more gradually[72].

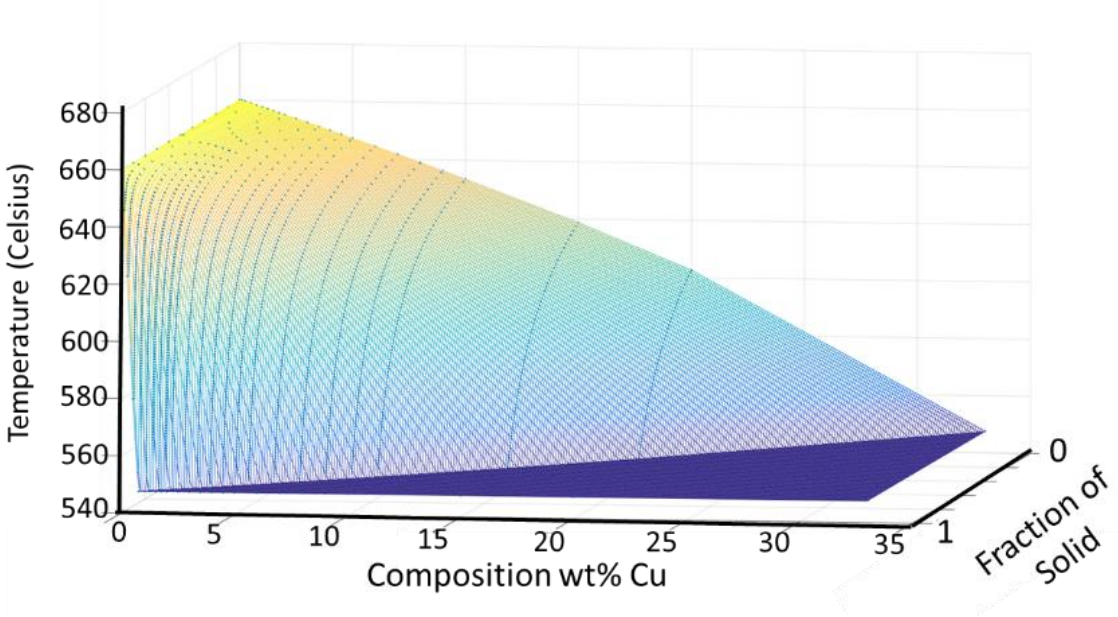

Figure 2.8: Composite Scheil simulation of the Al-Cu hypoeutectic compositions. The surface mesh can be used to approximate the expected fraction of solid at each composition and temperature. As seen, there is a large solidification range at the lower copper contents with a steep slope in the solidification curves at high solid fractions. As the copper composition increases the solidification range decreases with a lower liquidus temperature and a more gradual slope until the rejected solute reaches the eutectic point and solidifies[72].

The rejection of solute results in a compositional gradient in front of the solidifying material. The composition change results in a material with a different equilibrium liquidus temperature than the initial composition of the material, resulting in an associated liquidus temperature gradient. If the experimentally imposed thermal gradient is less than the liquidus temperature gradient, an undercooled region exists ahead of the solidifying material. This condition is referred to as constitutional supercooling (**Figure 2.9**). In the context of this dissertation, undercooling will be used to describe constitutional supercooling as this is fundamentally undercooling, i.e. cooling a liquid below the melting point.

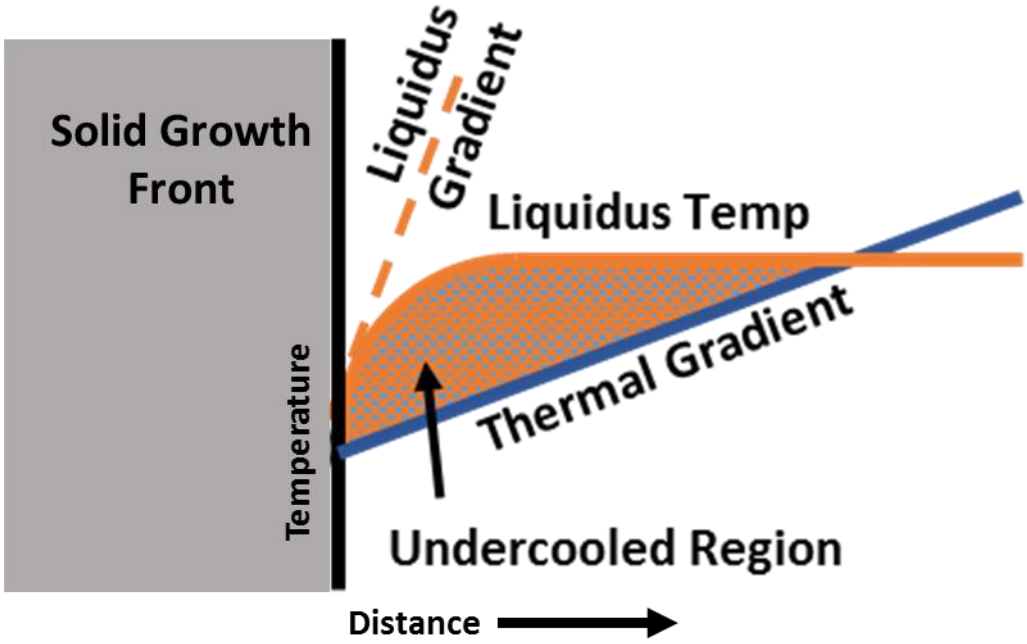

Figure 2.9: Schematic indicating the evolution of undercooling during solidification. In the above figure the thermal gradient (blue) is a lower slop than the liquidus gradient (orange) producing an undercooled region ahead of the growing solid (grey)

Without the existence of an undercooled region, planar growth is more favorable. With increased undercooling the planar interface destabilizes resulting in growth of perturbations in the planar front leading to cellular growth, transitioning to columnar dendritic growth with increased undercooling[51,74]. A substantial amount of undercooling can then result in a transition to equiaxed growth when there is enough undercooling to activate new nucleation events ahead of the front prior to being overtaken by the previous solidification front[69]. This transition is referred to as the columnar to equiaxed transition (CET).

The CET is generally depicted in a plot of thermal gradient vs solidification velocity with the Hunt Criterion being a common approximation[51,69],

$$g_g \approx n_g \frac{4\pi}{81}\left(\frac{\sqrt{v_T}}{G}\right)^3 \quad (Eq\ 2.4)$$

where g_g is the fraction of grains ahead of the solidification front, n_g is the number density of grains, v_T is the isotherm velocity, and G is the thermal gradient. Here grains are

assumed to be fully columnar when $g_g = 0.01$ and fully equiaxed when $g_g = 0.99$. While the thermal gradient effect has been discussed, the velocity component is related to the development of the undercooled region. The liquidus temperature gradient is dominated by the composition gradient, which is in turn impacted by the diffusivity of the alloying elements in the liquid[75,76]. Fast diffusing elements can reduce the magnitude of the undercooled region, however, as this is a kinetic effect, increasing solidification velocity decreases the time for alloying elements to diffuse and therefore maintains a high liquidus temperature gradients. **Figure 2.10** shows a typical CET plot from the Hunt criterion along with overlays indicating typical conditions for conventional metal processing routes.

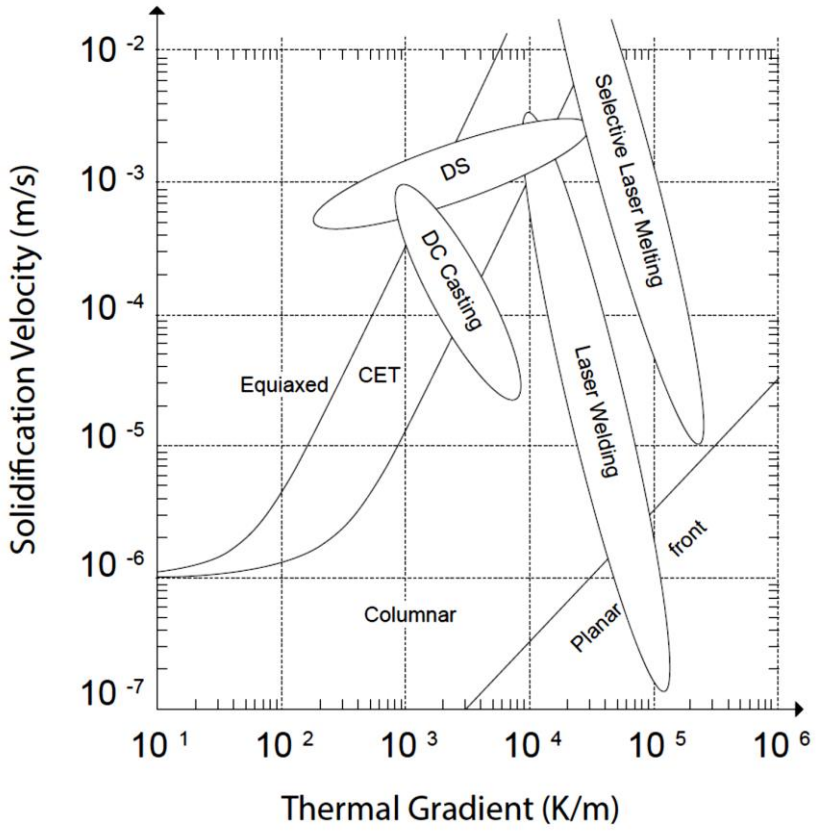

Figure 2.10: Columnar to Equiaxed Transition. A plot of thermal gradient vs isotherm velocity with the columnar to equiaxed transition (CET) highlighted. Additional bubbles have been added to indicate the thermal regimes at which typical metallurgical processes occur. Adapted from Dantzig and Rappaz[51].

The CET is not a sharp transition and is a gradual evolution from elongated columnar like grains to progressively more equiaxed structures[77]. The two transition points have been previously calculated by W. Kurz et al.[70] where equiaxed grains occur when

$$G < 0.6N_0^{1/3}\Delta T(1-\Delta T_n^3/\Delta T^3) \quad (Eq\ 2.5)$$

and columnar grains occur when

$$G > 2.9N_0^{1/3}\Delta T(1-\Delta T_n^3/\Delta T^3) \quad (Eq\ 2.6)$$

where N_0 is the number density of nucleation sites, ΔT_n is the critical undercooling to initiate a nucleation event, and ΔT is the undercooling. An approximation for the undercooling of a system, not accounting for advection or conduction, can be made from[70]

$$\Delta T = (20C_0 m(k-1)\Gamma/D)^{0.5}V^{0.5} \quad (Eq\ 2.7)$$

where m is the liquidus slope on the equilibrium phase diagram, Γ is the Gibbs-Thomson coefficient, D is the diffusivity of the solute in the liquid, and V is the solidification velocity. Plotting the columnar to equiaxed transition for the aluminum alloy Al-7075 in the high thermal gradient regions typical of additive manufacturing (**Figure 2.11**) it can be seen that extremely high solidification velocities would be required to form fully equiaxed microstructures, on the order of >1 m/s.

The calculations for the CET in Al-7075 were simplified using a constant literature value for $C_0 m(k-1)$ of 20.4,[78] an assumed diffusivity of the alloying elements close to that of copper ($5*10^{-9}$ m^2/s)[79–81], and an approximate Gibbs-Thomson coefficient based on the Al-Cu system ($5*10^{-8}$ °Cm)[51,82,83]. Additional assumptions include: constant dendrite tip radii, minimal effects from the thermal and solutal Péclet numbers, and no solute trapping. As these all affect the equilibrium solute rejection compositions they may have an impact on the location of the CET, however the effects are limited to the ΔT term and are

not likely to impact this by a significant amount. The N_0 term as previously discussed is assumed to be an existing nucleant density. Assuming this can be greatly increased with the aid of inoculation, the CET can be drastically shifted into a more reasonable region to process high thermal gradient solidification with equiaxed grains (**Figure 2.11**). Additionally certain elemental additions can have a large impact on the undercooled region as will be discussed further in Chapter 4.

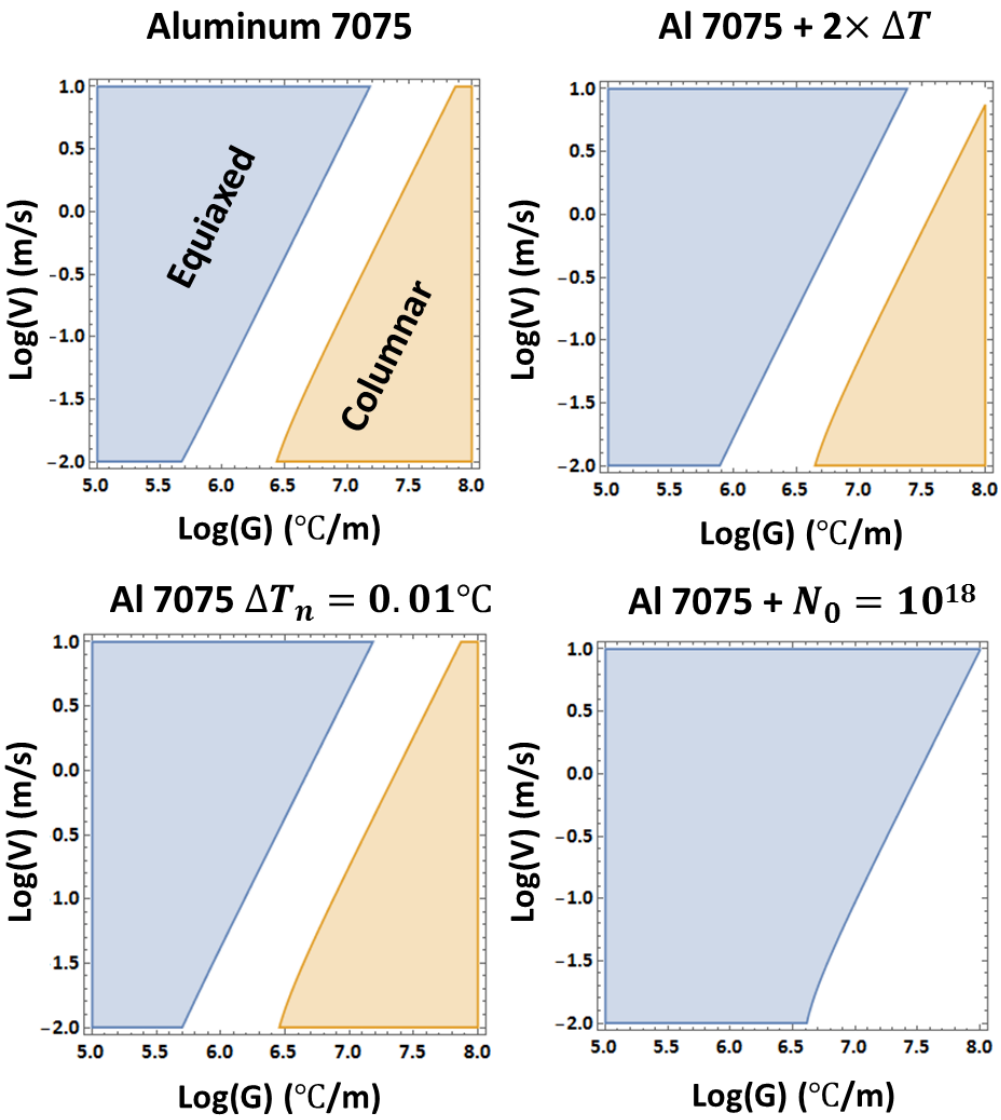

Figure 2.11: Columnar to Equiaxed Transition for Al-7075. Multiple columnar to equiaxed transitions have been calculated for Al-7075 utilizing varying parameters with the high solidification velocity and thermal gradient areas of the CET diagram highlighted where additive manufacturing based solidification is likely to occur. (Top-Left) Calculated using typical Al-7075 compositions and solute diffusivities ($10^{-9}m^2/s$) and critical nucleant undercooling of 2.5℃ and typical nucleant densities approximated to $10^{15}/m^3$. (Top-Right) Increasing the effective undercooling ahead of the solidification front by about 2X. (Bottom-Left) Decreasing the critical nucleation temperature, and (Bottom-Right) Increasing the nucleant density to $10^{18}/m^3$, which is on the order of the nucleants added to inoculated aluminum in later chapters.

A complete calculation of the effects from the Péclet numbers and solute trapping is difficult for a system such as Al-7075 due to the multiple alloying elements (Cu, Zn, Mg, Cr) which all have different diffusivities, partition coefficients, and diffusion velocities. In order to understand an order of magnitude effect on the undercooling ahead of a

solidification front a model Al-3wt%Cu system can be used to understand the effects. This can be rigorously calculated from the following equation[51]:

$$\Delta T = \frac{H_f}{C_p} Iv_{3D}(Pe_T) - m_l C_0 \left(\frac{(1-k) Iv_{3D}(Pe_C)}{1-(1-k) Iv_{3D}(Pe_C)} \right) + \frac{2\Gamma_{sl}}{R} \quad (Eq\ 2.8)$$

Equation 2.8 has three major terms representing the thermal, solutal, and interfacial effects on undercooling, respectively. The final term only has a major effect at very small radii. Here H_f is the latent heat of fusion, C_p is the volumetric heat capacity, m_l is the liquidus slope, C_0 is the initial composition of solute, k is the partition coefficient, Iv_{3D} indicates the use of a 3D Ivantsov function of the Péclet numbers, Γ_{sl} is the Gibbs-Thomson coefficient, and R is a characteristic radius of the solidifying material typically defined as the radius of the growing dendrite tip or nucleating phase. The characteristic radius is also used in the definition of the Péclet numbers as defined for the solute as: $Pe_C = (VR)/(2D)$, and for the thermal effect: $Pe_T = (VR)/(2\alpha)$, where V is the solidification velocity, D is the diffusivity of the solute, and α is the thermal diffusivity. Accounting for solute trapping, the value for k is also dependent on the solidification velocity according to the formula developed by Aziz[75,76,84]:

$$k = \frac{\left(\frac{V}{V_D} + k_0\right)}{\left(\frac{V}{V_D} + 1\right)} \quad (Eq\ 2.9)$$

where V_D is the diffusion velocity of the solute, and k_0 is the equilibrium partition coefficient. This indicates that as solidification velocity increases the partition coefficient approaches 1, effectively eliminating the solute induced undercooling. The effective partition coefficient for Al-3wt% copper is shown in **Figure 2.12**:

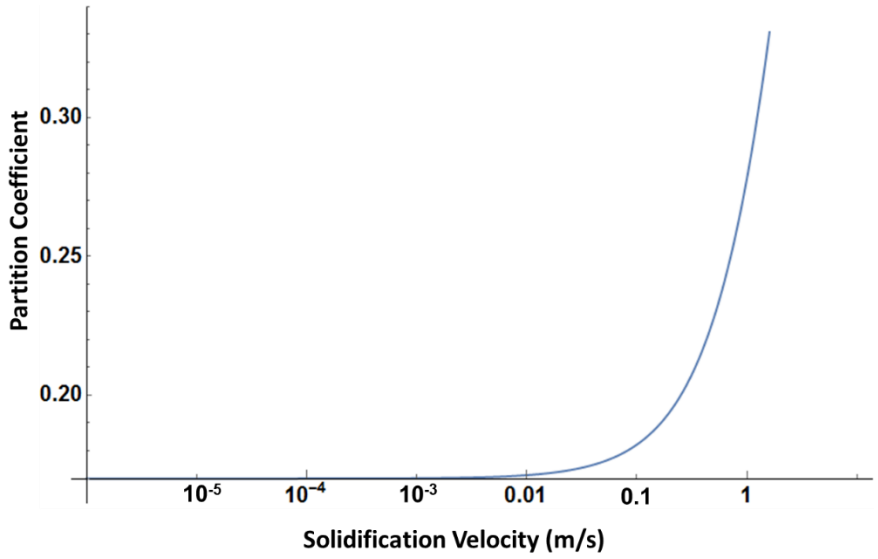

Figure 2.12: Plot of partition coefficient with respect to solidification velocity for Al-3wt%Cu. There is very little change in partition coefficient until the solidification velocity exceeds 0.01 m/s, but only increases to about 0.25 even at 1 m/s solidification velocities.

Utilizing a combination of equations 2.8 and 2.9, it is possible to calculate the undercooling ahead of a solidifying interface for different characteristic radii (**Figure 2.13**). Characteristic radii are shown relative to the size of potential heterogeneous nucleation sites as will be described below and in subsequent chapters. The relative magnitude of the undercooling is important, as it implies that relatively large undercooling can be achieved in the fast solidifying additive process (between 0.1 m/s and 1 m/s [33]), although the effect of solute trapping tends to limit the undercooling to less than 35℃ at the high end of the expected solidification velocity in additive (1 m/s)[33].

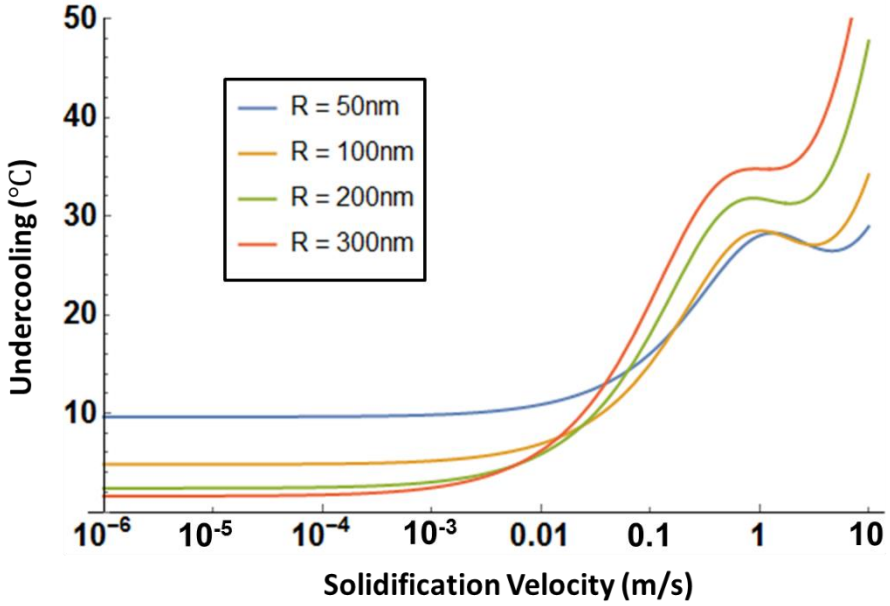

Figure 2.13: Calculated undercooling at different solidification velocities and characteristic radii for Al-3wt%Cu. Initial offset at the smaller radii is dominated by the small particle radius and the Gibbs-Thomson effect in equation 10. The evolution of the hump at the higher solidification velocities is driven by a change in the effective contribution of solutal undercooling from the change in partition coefficient from equation 9.

2.3 Inoculation of Metals

The use of secondary particulate to refine and control the grain structure of solidified metals is common place in many liquid metal processing operations, where as-cast grain sizes in some aluminum alloys can be reduced from 1mm to <100µm[39,78,85]. Common inoculants have been identified for a variety of alloy systems, including TiN for ferrous alloys[86], $CoAl_2O_4$ for nickel alloys[87], and TiB_2 for aluminum alloys[88]. These inoculants can be added in a variety of ways. TiN has been incorporated in welding applications by introduction into the welding gas or added to the weld joint prior welding[35], $CoAl_2O_4$ is added as a slurry to the base of superalloy casting molds to promote nucleation of higher densities of "seed" grains prior to single crystal casting, and TiB_2 is incorporated in casting through a salt reaction to form a high fraction of particulates in the melt[89]. While the types of inoculants are well known the mechanism of nucleation

and growth is still debated and methods for identifying new inoculants are unclear. Identification of these grain refiners has largely been by trial and error, in which the discovery of identifiable particulates from contaminations or unexpected reactions in the grain centers of solidified material indicate effective refiners[51].

The most consistent attribute of these inoculants is an apparent crystallographic coherency with the solidifying material[51,90]. This is attributed to an assumption that crystallographic coherency is related to a minimization of surface energy penalty[91], in the spirit of classical nucleation theory, **Equation 2.1**. This is however not the case for the Al-TiB_2 system in which substantial crystallographic mismatch (>10%) exists between FCC aluminum and the hexagonal TiB_2 phase, as will be discussed in Chapter 3. TiB_2 is one of the most potent grain refiners in the aluminum alloy system and is therefore one of the most studied, but seems to not follow the crystallographic matching philosophy present across other alloy systems. For example the inoculation of ferritic iron with titanium nitride shows a <5% lattice mismatch in the $(100)_{BCC\text{-}Fe}//(100)_{TiN}$ interface, while the most favorable orientation relationship in the Al-TiB_2 system is >10% lattice mismatch $(100)_{Al}//(001)_{TiB_2}$. The calculation methodologies for lattice mismatch are described in Chapter 3.

The mechanism of nucleation on TiB_2 is described in more detail in Chapter 3, however the general explanation for this discrepancy is that TiB_2 is not the actual nucleant phase, but instead a layer of Al_3Ti forms on the TiB_2 surface[92–94]. The Al_3Ti has greater coherency to the FCC aluminum and promotes nucleation[95,96]. This provides some self-consistency to the lattice coherency argument but does not substantially aid in extrapolating the success in the two stage nucleation event of TiB_2 to other alloy systems. Currently new inoculant discovery is limited to trial and error, but Edge to Edge lattice matching (E2EM)

techniques have been developed to help accelerate this discovery[97]. An expanded analysis of this theory and a new, more comprehensive analysis and discovery technique are described in Chapter 3.

2.3.1 Effects of Inoculants on Nucleation Rates

The mechanisms of nucleation have been described above, however the rate of nucleation events is ultimately what drives the evolution of solidified microstructures. The formation of an equiaxed grain structure can only occur if the rate of nucleation is commensurate with the rate of solidification. For instance a specific inoculant with a high potential for nucleation is only applicable for the control of microstructure if the rate at which nucleation events occurs is effectively controlled.

Heterogeneous and homogenous nucleation rates can be calculated given the following equation[51]:

$$I = v_0 p_c n \exp\left(\frac{-16\pi}{3}\frac{\gamma_{sl}^3}{\left(\rho \Delta s_f \Delta T\right)^2 k_B T} f(\theta)\right) \quad (Eq\ 2.10)$$

Where the $v_0 p_c$ term is related to the frequency of atomic attachment, n is the density of potential nucleation sites (where $n =$ density of atoms for homogenous nucleation), γ_{sl} is the solid liquid surface energy, ρ is the density, Δs_f is the entropy of fusion, ΔT is the magnitude of undercooling, $k_B T$ is the temperature dependent Maxwell-Boltzmann distribution indicating lower atomic mobility at decreased temperature, and $f(\theta)$ is a function of the contact angle with the substrate between 0 and 1 indicating the wettability of a heterogeneous nucleation site ($f(\theta) = 1$ in the case of homogenous nucleation). The impact of the $f(\theta)$ function, and hence the wettability of inoculants, on potential nucleation rates is shown in **Figure 2.14**.

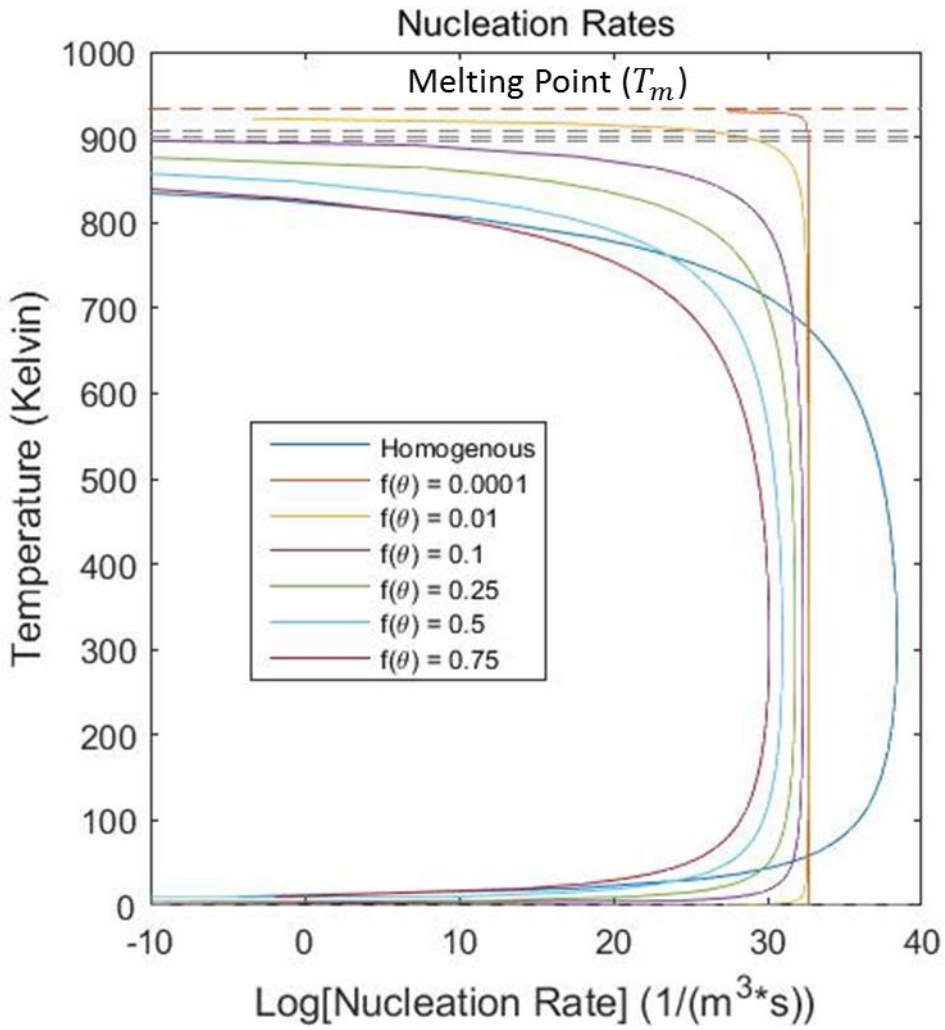

Figure 2.14: Nucleation rates vs Temperature in Pure Aluminum. Results are shown for homogenous nucleation and heterogeneous nucleation with different values for f(θ) indicating significant effects on nucleation rates at low undercooling based on heterogeneous nucleant particle wetting. Nucleant density used 4.5 x 10^{19} particles/m^3

A great deal of insight on the potential effects of nucleation rates can be discerned from **Equation 2.10**. Naturally the increase in density of nucleants will increase the nucleation rate. For heterogeneous nucleation the maximum nucleation rate tends to converge to a value dependent on the introduced nucleant density, while homogenous nucleation can achieve much higher nucleation rates due to the fact that every atom in is a potential nucleation site, however this is only possible at substantial undercooling where the critical radius for nucleation has decreased substantially. There is also a competing energetic and

kinetic effect in the denominator of the exponent, where increasing the undercooling increased the driving force for nucleation, but decreasing the system temperature also decreases the kinetic mobility of the atoms via a Boltzmann distribution, $k_B T$. This mobility effect is seen in **Figure 2.14** as evidence by the decrease in homogenous nucleation rates at substantially undercooled conditions.

Additionally, given all physical constants within the exponent are positive, increasing the value of the γ_{sl} and $f(\theta)$ decreases the nucleation rate, while in the case of favorable nucleation γ_{sl} and $f(\theta)$ are minimized to decrease the energetic barrier to nucleation leading to high nucleation rates. The solidi liquid surface energy, γ_{sl}, can be manipulated by the alloying constituents while the $f(\theta)$ function is simultaneously impacted by the alloy constituents and the interaction with the nucleant substrate[51,91,98]. This follows classical nucleation theory in which decreasing the surface energy penalty and providing a low surface energy substrate decreases the total energy barrier for nucleation.

Following an understanding of the mechanisms and rates of nucleation, the next step in controlling microstructure evolution during solidification is to capture the growth effects. While nucleation is a required precursor to the liquid to solid phase transformation, the evolution of a fully solid structure requires the continued growth of the solid phase from the nucleant to form a grain structure. Nucleation events which produce solid that does not grow to form full grains can be captured by the solidification front and results in an inclusion. Additionally these nucleation events may be pushed by the preceding solidification front slowing the growth of solidification until they have a chance to grow into new grains or are ultimately captured as previously described. A quantitative description of

which nucleation events lead to substantial growth events is needed to fully describe the role of inoculants on microstructure control.

2.3.2 Free Growth Model

As described in **Section 2.1**, growth of the solid phase is dominated by a free energy driving force once a critical radius is reached. Free growth assumes that the growth event occurs without influence from other solidification events and the local thermal conditions can be defined independently for each nucleation and growth event[51]. The free growth theory for inoculants was developed with this in mind to account for the apparent impact of inoculant size on the effective undercooling needed to activate the associated inoculant in the Al-Ti-B system[99]. Assuming the nucleating phase must form on a faceted phase the radius of curvature of the nucleating phase on the substrate must reach at least the critical radius dictated by classical nucleation theory, **Figure 2.15**. This implies that as the radius of the inoculant decreases the required undercooling to activate growth of the nucleating phase increases. This effect is captured in the equation for free growth undercooling[88,99]:

$$\Delta T_{fg} = \frac{4\gamma_{sl}}{\Delta S_v d} \quad (Eq\ 2.11)$$

where ΔT_{fg} is the critical undercooling to initiate free growth, γ_{sl} is the solid liquid interface energy, ΔS_v is the change in volumetric entropy, and d is the nucleant particle diameter. Plotting this equation for pure aluminum one can see that very small radii (<20nm) nucleants require extremely high undercooling (>20℃) to initiate growth **Figure 2.16**.

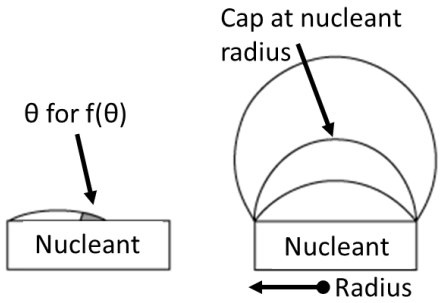

Figure 2.15: Schematic representation of heterogeneous nucleation of a nucleant particle. (**Left**) Θ is highlighted as the angle between the solid surface and cap film. (**Right**) Different potential cap radii based on the wettability indicating that at higher wetting angles the cap size increases.

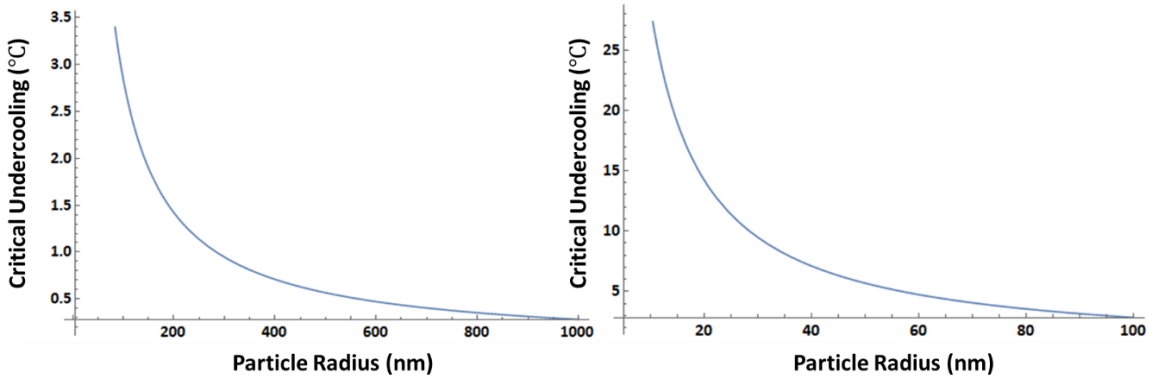

Figure 2.16: Plots of critical particle radius vs critical undercooling in aluminum. Two different ranges of particle radii are highlighted to show the relative change in critical undercooling at small radii.

Validation of this model has mainly been limited to a variety of cast aluminum alloy systems inoculated with Al-5Ti-1B master alloys, where the master alloy is enriched in titanium and expected to aid in the formation of a constitutionally supercooled region and of Al_3Ti as previously described[78,95,96]. Given a typical range of TiB_2 particle sizes, and by extension Al_3Ti surfaces, between, 0.1 µm and 10 µm, this indicates critical undercooling between 5.7K and 0.06K, respectively[88]. These distributions of particles are appropriate for casting alloys with grain sizes typically >100 µm, however given the melt pool widths are typically on the order of 100 µm in additive manufacturing, grain sizes (or grain widths in the case of columnar growth) tend to be <25 µm, with several grains spanning the width of the melt-pool (**Figure 2.17**)[100]. The associated grain size therefore indicates a smaller nucleant particle would be needed to avoid inoculants of the same relative size of the grains.

Holding the same volumetric ratio of inoculant to grain of 0.1 µm inoculant to 100 µm grain, decreasing the grain size to a more reasonable 10 µm for additive would indicate critical undercooling on the order of 55K. Given the solidification conditions of the typical additive process and the approximated idealized possible undercooling for a model system in **Figure 2.13**, this level of undercooling is extremely unlikely and the inoculant size likely require radii to be on the order of 100nm for the free growth model. As will be discussed in Chapter 4, it is likely that <100nm sized inoculants are in fact active during additive manufacturing. This can be explained by a combined understanding of the undercooling present during additive manufacturing and an analysis of the assumptions of the free growth theory.

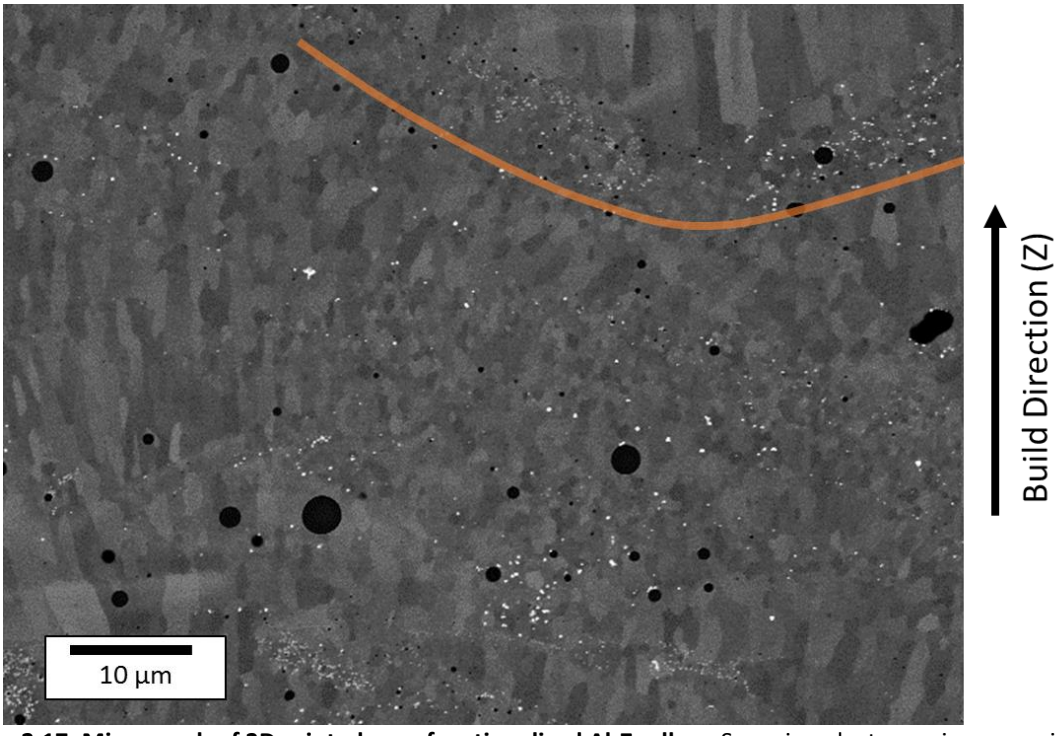

Figure 2.17: Micrograph of 3D printed nanofunctionalized Al-Zr alloy. Scanning electron microscopy image in backscatter highlighting the channeling contrast in the grains. A melt-pool boundary is highlighted in orange. Most melt-pool boundaries are indicated by a smaller grain size with more elongated grains in the center. This evolution of this microstructure will be discussed more in Chapter 3.

The free growth theory makes several thermodynamically accurate assumptions while ignoring some physically relevant phenomenon which may be self-fulfilling in their

application. The theory assumes a single nucleation event occurs on each inoculant, and the associated nucleation radius is directly tied to the inoculant size[99]. At large particle diameters it is possible that multiple nucleation events may occur on the inoculant surface leading to a higher statistical chance of a nucleation event growing. Larger nucleation sites also produce an initial solid that is volumetrically larger than that of a smaller inoculant releasing a greater amount of latent heat, a factor which is typically assumed to be negligable[99]. This may lead to local recalescence re-melting a smaller nucleation event and masking the similarly active nucleation event. Additionally substrate effects seem to have no impact on the calculated free growth undercooling. This however is not physically true as previously described where the substrate effects have a direct link to the free energy and nucleation penalty. Additionally the analysis of the undercooling related to the characteristic length scales would indicate continued decrease in particle size below about 100nm would result in substantial increases in effective undercooling making very small inoculants preferable, however this is not seen in the literature and is likely related to the substrate effects shown in **Figure 2.15**, where the effective radii of the solidifying material is directly related to the interaction with the substrate. It has been noted in the literature that the free growth model does not accurately predict the effects of nanoparticles and this may relate to an accumulation of particulate at the solidification front acting to restrict growth or other unknown mechanisms[101]. Larger substrates also have a statistically higher chance of containing a critically lattice matched nucleation site. Small radii particulate, specifically nanoparticles have higher surface energy and may reduce this by avoiding a faceted interface, unlike larger particulate, with high availability of faceted surfaces. The energy term generalized in the free growth theory does not account for these energetic changes

which makes the extrapolation to all particle compositions and sizes tenuous. Additionally there are complex fluid flow and thermal fields present in additive which make the extrapolation of an independent free growth event difficult to reconcile with the complex solidification behavior in additive manufacturing.

While the free growth theory has been effective in the analysis of Al-Ti-B systems, the extension to other systems has been limited and seems to fall short in its description of the inoculation in the additive process. It is possible that the longer solidification times in casting produce ideal thermal conditions for the free growth model making the model statistically applicable but not physically illustrative. For the analysis in this dissertation, as will be discussed in more detail in Chapters 3 and 4, the size of a specific nucleant particle is expected to have a negligible effect on the critical undercooling and nucleation rates. Instead, the number density and lattice registry of the inoculants will be focused on as the dominant mechanism of grain refinement.

2.4 Solidification in Additive Manufacturing

Nucleation and growth have, thus far, been discussed mostly independent of solidification boundary conditions. The associated thermal and kinetic conditions for every solidification process are different. Solidification models exist for many common metallurgical processes including casting and welding[35,39], however a comprehensive solidification model for additive manufacturing has still not been developed. Welding models are likely the most applicable given the functional similarity, however, the increased thermal gradients and solidification velocities of additive manufacturing result in higher fluid velocities and Marangoni effects[60]. The best additive models focus mainly on identifying and tracking isotherms and understanding fluid flow and spatter effects, however

very little modeling has focused on the actual solidification phase transformation, which is typically just roughly approximated.

The models for additive manufacturing are generally divided into efforts that model the thermal effects and those that model the melt-pool, including liquid flow effects[60,63]. The division of these is largely due to the time domains in which each simulation operates. Thermal modeling, derived largely from welding simulations, tends to utilize finite element analysis (FEA) where heat conduction across voxels can be well defined numerically. The addition of fluid flow and mass balance into FEA simulations, however, drastically increases the computational time and complexity of the numerical analysis. This is particularly problematic on the time scales for which additive manufacturing occurs, where motion of the heat source can exceed 1 m/s. Therefore accurate analysis of any fluid flow would require an extremely small time domain to accurately capture the liquid effects. This has pushed general thermal models to focus mainly on general approximations of thermal gradients and solidification velocities as well as thermal stress accumulation over a relatively large area of the part, rather than explicit analysis of the melt-pool[33,34,57,102]. These analysis techniques have been useful in designing scan strategies to reduce thermal stress and improve consistency across the build, but provide little information about the solidification condition during processing.

The second modeling approach has been focused on explicit analysis of melt-pool formation and stability using multi-physics computational fluid dynamics (CFD)[103–105]. This has provided analysis of not only fluid flow in the melt-pool but also laser and powder bed interactions. Coupled with high speed videography the CFD models can be validated to understand evolution of welding key-holes and particle ejection during additive

manufacturing[106]. This has provided interesting insight into pressure differentials around the melt-pool which can reposition powder in the powder-bed and evolution of surface tension and recoil pressure-driven fluid mixing during laser powder-bed fusion[105,107]. This provides a great deal of information regarding the thermal conditions prior to solidification, but these models still do not explicitly simulate a solidification event, and instead use a linear change in viscosity thorough a defined semi-solid zone.

While this research effort will not explicitly develop a solidification model for additive manufacturing, it is important to investigate the current state of additive solidification modeling to understand how the boundary conditions impact the previously described nucleation and growth phenomena. In general the solidification occurs under high thermal gradients $>10^5$ K/m and fast solidification velocities 0.01-1m/s[33].

Additive manufacturing is a layer by layer process in which progressive layers of material are melted on top of or next to one another. This provides a substrate for nucleation in which new grains can grow in an epitaxial fashion off of preceding or adjacent layers[100]. Given the solidified metal under the melt-pool is identical to the metal solidifying, the heterogeneous nucleation barrier is nonexistent, promoting epitaxial growth. As layers continue to build up grain selection can occur, resulting in formation of highly oriented grain structures in the fastest crystallographic growth direction (**Figure 2.18**). Any potential grain refining inoculant must be effective in nucleating new grains ahead of the highly favorable columnar structures. This is more difficult than in casting, or even welding, where the solidification velocities (<0.01 m/s) are relatively slow allowing enough time for additional grain nucleation ahead of the growth front[35,39].

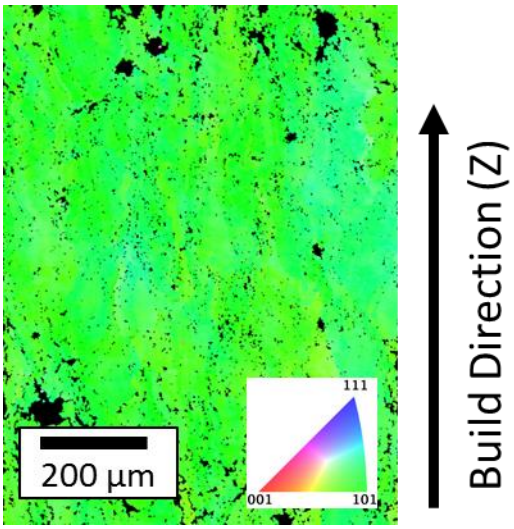

Figure 2.18: Inverse pole figure map of 3D printer aluminum. Referenced to the z-direction, the micrograph indicates a highly textured material in the (101) orientation.

The grains also grow in the direction of the highest thermal gradient, producing a typical weld-like structure where columnar grains grow towards the center of the melt-pool[108], sometimes leaving equiaxed grains at the top center due to decreased thermal gradients from latent heat release (**Figure 2.19**). This effect is readily apparent in 2D micrographs, however more complicated effects can also be seen in 3D models in which the raster effect of the laser can drag the growth direction of grains in multiple directions leading to significant intergranular misorientation[109].

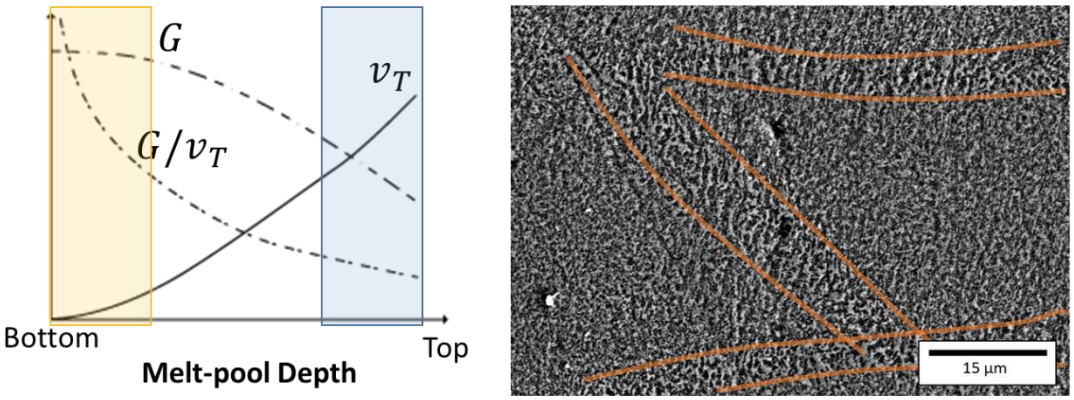

Figure 2.19: Thermal effects in inside the melt-pool. (**Left**) A notional plot, adapted from Dantzig and Rappaz[51], of the thermal gradients and solidification velocities in the melt-pool related to the change in shape and boundary conditions during solidification along with associated enthalpies of fusion. Highlighted at the bottom of the melt pool and in line with the CET plots previously presented more columnar and/or larger cell structures would be expected, likewise more equiaxed or smaller cell structures would be expected at the center of the melt-pool. This is demonstrated (**right**) in the SEM micrograph of etched 3D printed Al10SiMg where the build direction is towards the top of the page.

The thermal and kinetic boundary conditions in additive manufacturing are highly complex and can change rapidly depending on parameters and build geometries which change the critical heat conduction paths and layer by layer thermal load. Inoculation is likely the simplest way to overcome the variety of potential microstructures which could develop by shifting the dominating microstructure control mechanism to the number density and activity of heterogeneous nucleation sites. Thus the research described in this dissertation focuses on a novel approach to inoculation that is effective under additive manufacturing thermal conditions.

Chapter 3

Selection and Incorporation of Grain Refiners

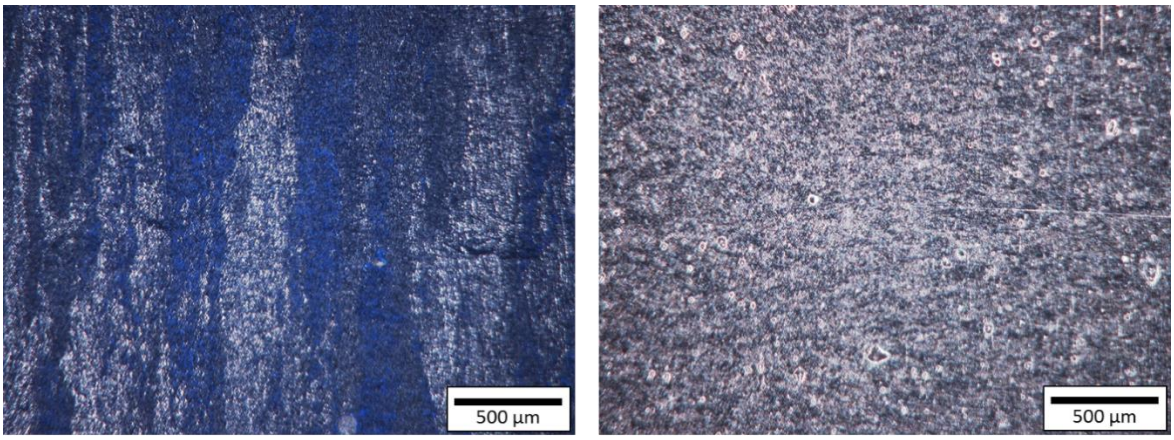

Figure 3.1: Additive Aluminum Microstructures Before and After Inoculation via Nanofunctionalization. (Left) Pure aluminum, (Right) Al-1at%Ta. Both samples were polished to a 50 nm alumina vibratory poilish, etched using Keller's reagent, and imaged under polarized light.

This chapter will investigate selection methodologies for conventional grain refiners and strategies for incorporation during additive manufacturing. The potential impact of secondary inoculants on microstructure control during additive processing is unmistakable, as shown in **Figure 3.1**, where the introduction of 1 at% Ta into additive unalloyed aluminum results in a 1000X decrease in grain size and a shift from columnar to equiaxed grain morphology. The major issue in realizing this potential is the mechanism in which these inoculants are incorporated in the additive process. Historically these are added to cast alloys where columnar grains typically grow towards the center of the casting[39,59,101]. It is therefore natural to assume that these same incorporation mechanisms could be applied to additive manufacturing. Furthermore, understanding how these conventional inoculation

particles are introduced will aid in understanding the applicability to additive process, specifically in the manufacturing the ingots used for that atomization process.

3.1 Inoculation in Aluminum Alloys Systems

Cast aluminum alloys are some of the most widely researched inoculated systems[101]. The most common and industrially relevant inoculant as previously discussed, is TiB_2. However a variety of other inoculant systems have been attempted including Al_3Ti, Al_3Zr, ZrB_2, AlB_2, and TiC[91,99,110–114]. The introduction can occur along a variety of paths, but typically revolve around the production of master alloys[39]. Master alloys are created with a high concentration of the targeted inoculant. These can be created by direct addition of the inoculant to a liquid with appropriate mixing including, more recently, the application of ultrasonic mixing to improve dispersion. More commonly inoculants are created using a reaction methodology where precursors of the targeted inoculants are added to react and form the targeted inoculant[115].

The TiB_2 system is an excellent example of the reaction mechanism being used to form the targeted inoculant. In some cases pure titanium and boron are added to liquid aluminum and allowed to dissolve at high temperatures (>1000C)[89]. This process can be energy intensive because the melt must be held at elevated temperatures for long periods of time (>30 min) to facilitate full dissolution of the titanium and boron along with appropriate timing for formation of the TiB_2 phase[89,115]. Additionally, early formation of the TiB_2 phase can result in coarsening of the TiB_2 resulting in a distribution in TiB_2 sizes, and subsequent Al_3Ti interfaces, the negative impact of which was discussed in Chapter 2[88]. The most common method of TiB_2 formation is the salt reaction method in which the following reaction takes place[89]:

$$K_2TiF_6(l) + KBF_4(l) + Al(l) \rightarrow TiB_2 \text{ (in Alloy)} + KFAlF_3(l) + KF(l) + AlF_3(l)$$

This method has the advantage of quickly and uniformly distributing the titanium and boron, which enables fast (<30 min) dissolution and reaction in the melt helping to produce uniform distributions of TiB_2 particulate. Additionally this can be accomplished at lower temperatures than those required to easily dissolve elemental titanium and boron[89,115]. Unfortunately this process suffers from safety and environmental hazards due to the formation and handling of high temperature molten fluoride salts.

Addition of inoculants to the liquid metal can be completed through direct addition of either a master alloy or loose inoculant particles to the liquid and allowed to disperse naturally, or more commonly mixed using either a conventional stirring process or induced liquid convection[116]. In some cases, ultrasonic agitation has been used to disperse particulate, although the applicability to large volumes is difficulty due to the dampening effects of large volumes of molten metal[117–119]. The master alloy route is generally the most industrially applicable due to the ease of working with ingot stock, as opposed to powder and utilizing an inoculant that is already pre-wetted to the matrix alloy reducing the tendency for agglomeration and segregation[39]. The inoculated melts are then directly cast to a final shape or ingot to be machined.

3.2 Feedstock Production for Additive Manufacturing

While additive manufacturing is itself a manufacturing process, there are several initial raw material manufacturing processes required before the final laser or electron beam based melt and solidification step[1,3]. The most important of which is the atomization of the base powder, which is in turn the only step in which the previous casting based inoculant incorporation processes could be applied. Most powder feedstocks for additive

manufacturing are produced through a gas atomization process, although plasma atomization is a growing market[120]. These are highly industrialized and researched processes[121–123]. During the gas atomization process a large heat of metal (typically >500 lbs) is melted above a ceramic nozzle. Once the heat is fully molten the metal flows through the nozzle while inert gas jets (Argon or Nitrogen) break up the molten metal flow and atomize the metal into powder (**Figure 3.2**). Proper control of melt viscosity and flow is needed to produce high quality powder[121,124,125].

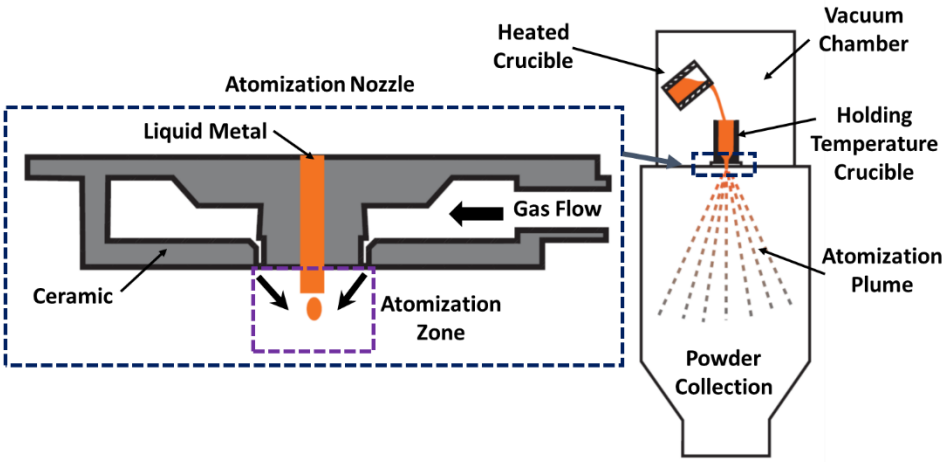

Figure 3.2: Schematic of the Atomization Process.

The gas atomization process is discussed here because control of the additive manufacturing process requires a tight distribution of highly spherical powder to provide uniform flow and spreading to ensure each layer is identical to the previous[126]. Misshaped particles lead to tumbling, which disrupts the coating process. Additionally particles which are too small or too large result in clumping or inadequate packing, respectively[45,127].

Given the need for high quality powder, it is not a trivial step to incorporate inoculants directly into the metal prior to atomization as this requires additional development of the atomization process to handle the changing viscosity and atomization

dynamics, decreasing powder yield and increasing final cost of the material[128,129]. Additionally the long molten duration times can lead to secondary dissolution or coarsening reactions of the targeted inoculants[89]. The former can result in a non-uniform distribution of inoculants in the resulting powder due to a change in inoculant density over the course of the atomization process. The latter can lead to severe processing challenges due to formation and growth of the inoculant phase, which can lead to nozzle clogging and significant changes in viscosity of the liquid metal[124]. An example of this has been recently observed when attempting to atomize an aluminum alloy with 1wt% Zr (**Figure 3.3)**. Here growth of large acicular Al_3Zr phases resulted in the failure of the atomization run.

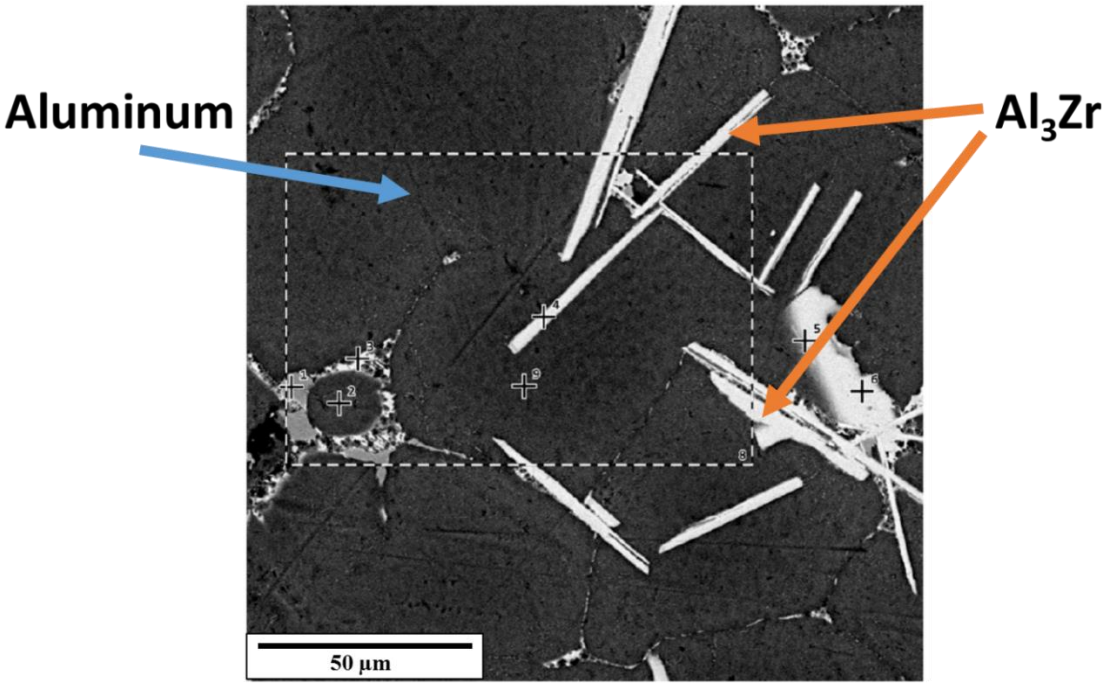

Figure 3.3: Resulting Microstructure of Clogged Nozzel during Atomization of Aluminum alloy with 1wt% Zirconium. Image provided by LPW Technology Ltd. Sample evaluation report dated 6/20/17.

Figure 3.3 highlights the difficulty in atomizing certain alloy compositions. In this case the 1 at% zirconium content increased the liquidus temperature of the aluminum alloy

by >400℃,[130] however to avoid secondary alloy element (e.g. Zn, Mg) boiling or evaporation as well as high temperature reaction with the ceramic nozzle, the holding temperature crucible (**Figure 3.2**), cannot be held at the true liquidus temperature where the Al_3Zr phase is in solution (>1000℃) resulting in rapid nucleation and growth of acicular Al_3Zr intermetallic phases. These increase the viscosity of the melt and begin interlocking creating a blockage in the nozzle, ultimately causing a stoppage in liquid flow into the atomization zone and a resulting in a failed atomization run.

3.3 Nanofunctionalization of Metal Powders

Given these concerns, the ideal inoculant incorporation mechanism would occur after the base alloy is atomized to avoid interfering with the otherwise industrially optimized atomization process. The natural first step would be utilizing a simple mixing routine (e.g. roll mixing) but the highly stochastic nature of powder mixing and blending leads to non-uniform distributions of inoculants within the powder bed, which is particularly problematic in the additive process where the entire powder bed is not melted and there is a high likelihood of incorporating inoculant free zones in the built component leading to locally poor properties. Other research has attempted to use high energy ball milling to incorporate secondary particulate into powders. While successful in incorporating high volume fractions of particulate the resulting powder can pick op contaminants and become highly deformed making it no longer acceptable for additive manufacturing[131–134]. A different approach is needed.

HRL Laboratories LLC. has developed a technology called *Nanofunctionalization* which enables direct assembly of nanoparticles onto the surface of micro-powders (**Figure 3.4**)[135]. Nanoparticles are electrostatically attached to the micro-powders providing a

durable assembled product that can accommodate the powder coating process in additive manufacturing, as described in Chapter 1. This technology is material agnostic and can enable assembly of small and large volume fractions of particulate. Because the process directly attaches the nanoparticle to the surface of particulate it overcomes the stochastic nature of simple mixing (e.g. roll mixing) and ensures a uniform distribution of nano-particulate in relation to the length scales of the melt-pool (i.e. ~100μm). Metal powder for laser powder bed fusion typically has average particle size dimensions between 25 μm and 50 μm produced by gas atomization, with highly spherical morphology to facilitate flow during the sequential layer processing. The nano-particles used in nanofunctionalization can range in size but are generally an order of magnitude smaller than the base metal powder. This results in a stochastic local organization on the surface of individual metal feedstock powders (Figure 4), but a uniform distribution relative to the additive build resolution (typically ~250μm). Additionally the assembly process does not alter the base powder shape and the small nano-particle sizes do not appreciably affect the flow-ability of the powder. As such an additive feedstock can be produced which has a high volume fraction of inoculant particles without negatively affecting the powder morphology.

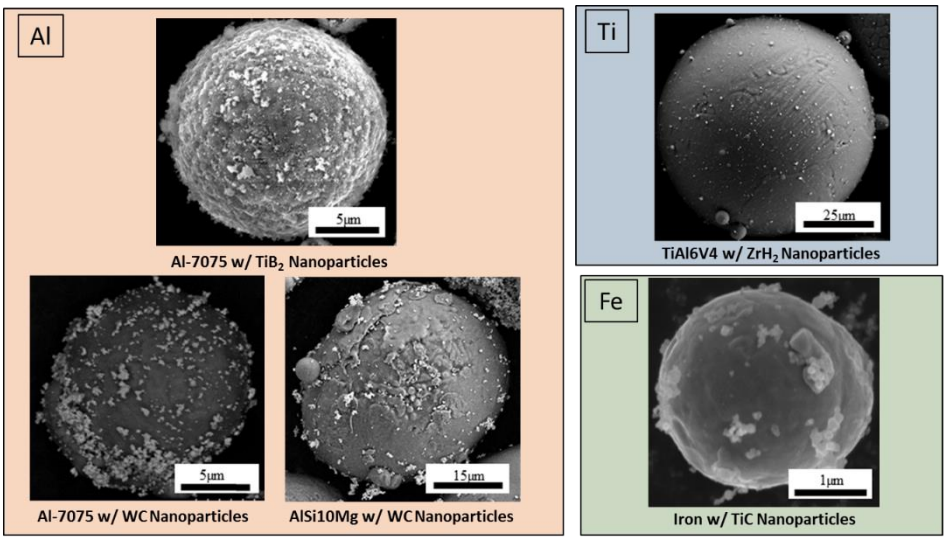

Figure 3.4: Nanofunctionalized Metal Powders. Multple compositions of micropowder and nanoparticles along with varying concentrations of nanoparticles are highlighted here to indicate the material agnostic nature of the nanofunctionalization process.

During the powder bed additive manufacturing process the laser or electron beam induces a molten bow wave which incorporates the nanofunctionalized powders directly into the highly turbulent melt pool (**Figure 3.5**)[60,104]. This results in a well dispersed inoculant which is readily available for new grain nucleation[135] or direct incorporation (e.g. as a metal matrix composite[136]) as the main solidification front approaches from the back of the melt-pool. This phenomenon occurs uniformly throughout the build volume producing a final component with well dispersed secondary particulate.

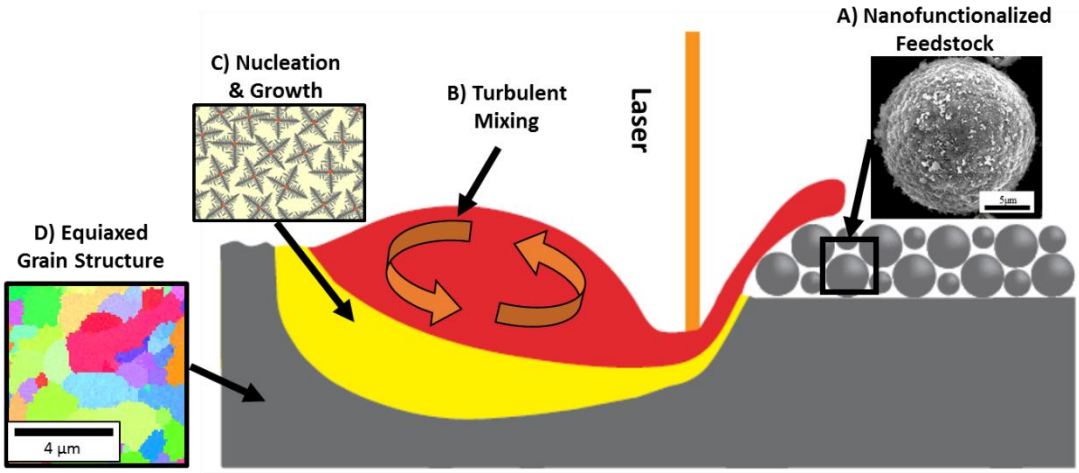

Figure 3.5: Nanofunctionalization *Assisted* Additive Process. During selective laser melting, the laser *(not to scale)* melts the material creating a wave which can sweep in the nanofunctionalized powder (A). Marangoni effects from high thermal gradients, along with laser induced recoil pressure induce a turbulant mixing state in the liquid melt-pool (B). Available particulate can then nucleat grains in the undercooled region (C) resulting in a solidified equiaxed grain structure (D).

The material agnostic nature of the nanofunctionalization process provides a unique opportunity to identify and incorporate grain refiners of arbitrary composition and potentially discover more potent inoculants than commonly used in casting processes. With this in mind a new inoculant selection criteria was developed based on lattice mismatch, the effect of which was described in Chapter 2.

3.4 Inoculant Selection Using Crystallographic Data

Previous attempts at discovering new grain refiners has focused on either simple Edisonian approaches or, more recently, edge to edge lattice matching (E2EM)[91,97,137]. The latter focuses on the ability to match the lattice parameters of closed packed crystallographic planes to other closed packed planes of secondary phases. The E2EM critical criteria is generally given as less than 10% mismatch related to the interatomic misfit along a single crystallographic orientation on a closed packed plane. The misfit is calculated as, $\varepsilon = |(d_1 - d_2)/d_1|$.[97] Here, d is the interatomic spacing of one of the constituent

phases along a specific closed packed orientation. This can be calculated for several potential inoculants of aluminum (d_1 = 2.85Å) (**Table 3.1**). While more rigorous lattice distortion calculations that consider single crystal elastic constants would provide improved predictions, there is too much missing information in available databases to take this approach.

Table 3.1: E2EM Calculations for Potential Aluminum Inoculants. Crystallographic data derived from the Materials Project. *indicates non-cubic symmetry

Nucleant	Space Group	Plane [hkl]	d_2 (Å)	E2EM Misfit
TiB_2	P6/mmm	100*	3.22	12.98%
			3.03	6.32%
WC	P-6m2	100*	2.92	2.46%
			2.85	0.00%
TiC	Fm-3m	111	3.06	7.37%
Al_3Ti	I4/mmm	211	2.884	1.19%
Al_3Ta	I4/mmm	211	2.883	1.16%
Al_3Nb	I4/mmm	211	2.89	1.40%
Al_3Zr	I4/mmm	211	2.95	3.51%

The logic of this approach is sound as it can be assumed that minimal variations in atomic spacing may lead to high lattice registry and would in turn produce a low surface energy interface which would promote heterogeneous nucleation as discussed in Chapter 2[138]. However, the E2EM has many fundamental limitations particularly when applied to non cube-to-cube crystal relationships, as shown in **Table 3.1**. From this analysis it is difficult to understand the impact of non-cubic structures on the calculation, particularly for WC which seems to have a single lattice parameter which is well matched, while the other is greater than that of Al_3Ti, Al_3Ta and Al_3Nb. The calculations for TiB_2 indicate one parameter is within the 10% threshold while the other is not. It additionally appears, from this analysis, that the Al_3Zr intermetallic would have less registry than the other Al_3X

intermetallic structures and therefore be less effective as an inoculant. This is however not the case as will be shown later.

The most obvious limitation is the focus on closed packed planes with constant atomic spacing when primary crystal growth directions are generally on lower density orientations (i.e. [100] for aluminum and most FCC metals vs the [111] closed packed Al plane)[39] and many intermetallic and ceramic materials have non-uniform atomic spacing in varying orientations[139]. While closed packed registry may lend itself to a greater chance of low density plane registry this is by no means a guarantee. Additionally the closed packed density of one crystal structure may not have the same atomic density as another crystal's closed packed plane and therefore requires a misfit dislocation. Finally the E2EM criteria in its typical form requires that the two crystal structures have some typical geometric similarity, i.e. cubic to cubic, cubic to tetragonal, etc. Application to more complex crystal pairs such as cubic to rhombohedral are more difficult to justify given the single strain metric in the E2EM model.

Inspired by the E2EM metric a criterion was developed focused on investigating the full crystal lattice effects. An areal strain metric was developed based on the registry of lattice planes rather than atomic spacing. While strain energies are not individually calculated due to a lack of available information as previously described, it is assumed that the strain energy effect can be well characterized over the area without explicit calculations with a greater degree of accuracy when compared to E2EM. In the case of materials with highly anisotropic elastic tensors this assumption is likely invalid, however the critical criteria was set to less than 5% mismatch (rather than the 10% in the E2EM) to limit the impact of false positives in the search criteria.

Citrine Informatics LLC was utilized to produce a software algorithm to employ this empirical criterion and to search the greater than 4,000 different materials. Citrine incorporated the density functional theory (DFT) crystallographic database from the Materials Project as the baseline crystal structures for analysis[139]. Limiting the search to Miller indices with values between 0 and 3 in the standard [hkl] nomenclature of lattice planes. This was chosen as a practical cut-off for computational efficiency as increasing Miller indices value increased the computation time exponentially. Citrine then implemented the search to produce >11 million different matching crystallographic pairs. Specific materials were omitted from the search criteria such as crystalline noble gases for practicality, as well as elements and compounds of radioactive isotopes for safety reasons. The software tool can then be used to select the appropriate primary phase one wishes to nucleate and then produce a list of potential matching inoculants with minimized areal lattice strain. Down selection can then proceed to account for atomic lattice plane density mismatch.

The selection criteria in the new lattice matching evolves from two main goals: promoting nucleation at low undercooling via low surface energy and facilitating high growth velocity crystallographic directions. The philosophy of lattice matching, as with the E2EM, implies a potentially low surface energy interface. Classical nucleation theory balances the free energy of formation with the associated surface energy penalty[67]. Decreasing the surface energy penalty is generally considered the key to promoting the nucleation event and the free energy of formation is considered a relative constant increasing with increasing undercooling and driving the growth of the new phase. During initial nucleation and growth however this is not necessarily true and the effect of the free energy

of formation can potentially be manipulated to further decrease the energy barrier to nucleation.

At small length scales and volumes of material, as at the onset of nucleation, the atomic interaction potentials between nucleant surface and atoms in the liquid can still impact the volumetric free energy. As such introduction of energy penalties such as strain, dislocations, or vacancies can increase the overall free energy of the system and change the free energy driving force of nucleation[138]. This philosophy stands in contrast to typical simplified thermodynamic calculations of free growth and critical nucleation radii where Richard's Rule ($\frac{\Delta H_f}{T_m} = \Delta S_f$) is typically applied based on standard enthalpy and entropies of fusion as opposed to accounting for the local change in energetics[51,59]. These effects are qualitatively captured in the lattice matching criteria, where areal strain is minimized decreasing strain energy and decreasing the tendency for misfit dislocations, while simultaneously decreasing the need for vacancies by matching crystallographic plane density. It is therefore incomplete to think of inoculation only from a surface energy perspective, particularly in the case of additive manufacturing where high solidification velocities rely on quick nucleation and growth to produce new grains ahead of the solidification front in the case of equiaxed growth. The associated strain energy has an effect on the free energy of the system thus impacting the free energy term (Δg) in the classical nucleation theory equation (($\Delta G = {}^{4}/_{3}\,\pi r^3 \Delta g + 4\pi r^2 \gamma_{sl}$). This reduces the driving force (Δg) for nucleation increasing the critical radius. Additionally this strain can affect the equilibrium melting point, effectively decreasing the actual undercooling at the nucleant surface.

While the strain energy effects are captured in some form using the lattice matching technique, the thermodynamic stability is not and must be considered independently. In the most extreme case FCC aluminum is well matched to the crystalline FCC argon lattice at 0K. This is, of course, intriguing rather than practical as argon is only solid at less than 90K while liquid aluminum solidification occurs closer to 900K. Additionally liquid aluminum is highly reactive with many carbides and oxides, forming Al_4C_3 or Al_2O_3, making many of the potentially lattice matched materials unlikely to be thermodynamically stable prior to a nucleation even from the liquid aluminum state[72,140]. As such additional analysis of thermodynamic stability of any potential nucleants was considered prior to testing. The lattice matching technique is also run at a static, 0K, temperature, while the nucleation and growth process happens over a dynamic temperature range. In order to accommodate for this one can further limit the material search by using materials with similar coefficients of thermal expansion or similar stiffness tensors to account for the temperature effects.

Given the aforementioned criteria, as well as insight from literature for common aluminum alloy additions, the following materials in **Table 3.2** were selected for investigation. Initial experiments were completed using pure aluminum with 1 vol% nucleant added via the HRL Nanofunctionalization process. In some cases, the added nanoparticulate is not the same as the target nucleant. This is by design, to leverage the high reactivity of the liquid aluminum to form the desired nucleant phase from the nanofunctionalized precursor particle without having to produce or procure intermetallic nanoparticles.

Table 3.2: Nanoparticles Utilized for Nanofunctionalization. All particulates were purchase from US Research Nanomaterials, Inc.

Nanoparticle Composition	Size Range (nm)	Target Nucleant
TiB_2	58	TiB_2
Al_2O_3	20	Al_2O_3
TiO_2	40	TiO_2
WC	55	WC
TiC	80	TiC
Ta	50-80	Al_3Ta
Nb	50	Al_3Nb
$ZrH_{(1-2)}$	<2000	Al_3Zr

3.5 Additive Manufacturing of Nanofunctionalized Metals

All experiments were conducted using a Concept Laser M2 system at HRL Laboratories. Parameter development was not pursued for these experiments; the equipment was operated utilizing the commercially provided parameters for the Concept Laser CL31 powder. The CL31 powder is an Al10SiMg alloy and given the similar reflectivity to pure aluminum was expected to provide effective melting of the nanofunctionalized pure aluminum system with very similar melting and solidification conditions across all tested materials. The exact parameters details were not provided by Concept Laser, but the machine capabilities are listed below in **Table 3.3.** All experiments were conducted in a nitrogen atmosphere, unless reaction with the nanoparticles was expected as with tantalum, in which case argon was used as the inert gas. The build contained a set of 1cm x 1cm blocks that could be analyzed for microstructure variations (**Figure 3.6**).

Table 3.3: Concept Laser M2 Specifications

Concept Laser M2 Specifications		
Parameter		**Value**
Laser	Type	Single mode, CW modulated Ytterbium fiber laser
	Wavelength	1070nm
	Power	400W
	Scan Speed	Up to 7.0m/s (Typical 1-2 m/s)
	Spot Size	50µm Minimum
Powder Handling	Build Chamber Size	80mm x 80mm
	Build Plate Size	70mm x 70mm
	Coater Blade Type	Rubber (Y-conformation)
	Layer Thickness	20-80µm
Atmosphere	Gas Type	Argon or Nitrogen
	Oxygen Limits	<0.1%

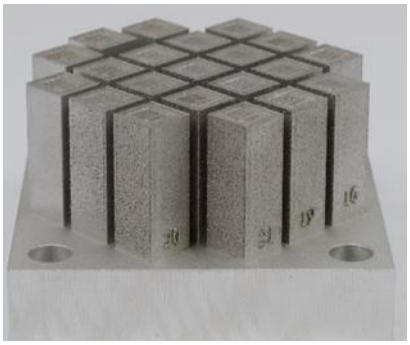

Figure 3.6: Example of As-Built Aluminum Microstructure Blocks.

Some changes in emissivity may be expected between the different types of nanofunctionalization, but given the primary laser interaction described above, this was likely a minimal impact on the total absorbed power[141]. The main difference between the tested pure aluminum and the parameters designed for the Al10SiMg system is the surface tension of the metal, which has a large impact on the shape of the melt-pool. Silicon reduces the liquid aluminum surface tension, aiding in melt-pool formation[142]. Decreasing the surface tension of the liquid allows the melt-pool to the underlying surface and avoid balling

up breaking the continuity of the weld line[35,143]. Additionally the surface tension of the liquid affects the shape of the melt pool, which is important in the design of the hatch overlap where the appropriate amount of re-melting is needed to effectively produce a dense component without lack-of-fusion defects. This indicates the utilized parameters may have difficulty producing a stable melt-pool in the pure aluminum system. Regardless of this, the small additions of particulate added where not expected to significantly change the surface tension of the liquid aluminum and the experiments could therefore be considered as roughly equivalent in thermal history and melt-pool behavior between each composition of material tested.

Samples were removed from the block using a water cooled cutting tool and polished using sequentially finer grit SiC paper and finished using 1μm diamond paste and colloidal silica. Select resulting microstructures and highlighted features are shown in the **Figure 3.7** below. Given the large variations in microstructures observed, multiple imaging modalities were employed, ranging from optical to scanning electron microscopy (SEM). Additional analysis of additively manufactured nanofunctionalized pure aluminum alloys will be discussed in Chapter 4.

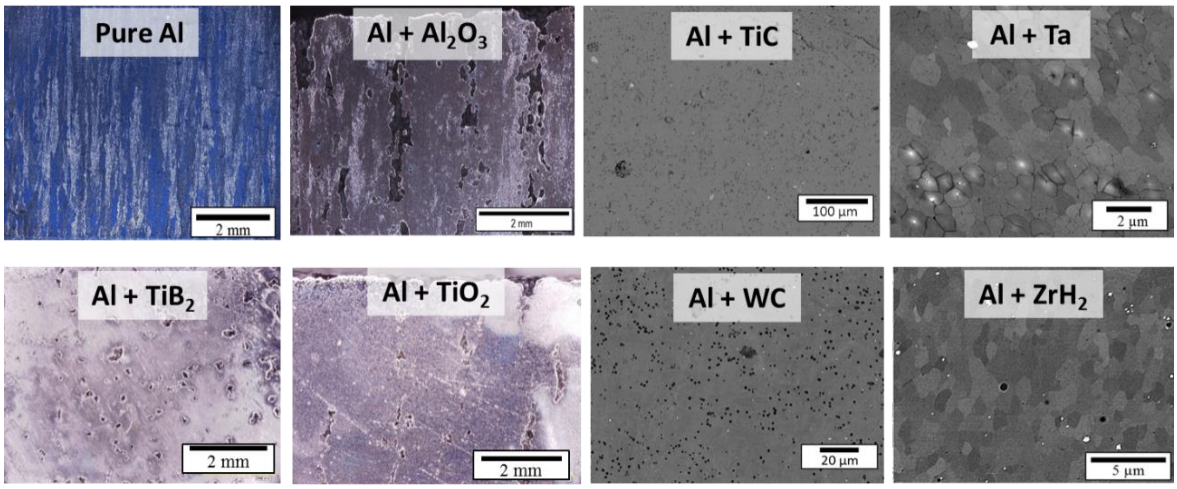

Figure 3.7: Resulting Microstructures from Selected Nanofunctionalized Material. Due to the varying sizes of characteristic microstructure elements, multiple imaging modalites are employed. The left half are optical images while the right half are scanning electon microscopy images utilizing the backscatter detector. All microstructures, except Al+TiB_2, are shown in the XZ plane with the build direction oriented towards the top of the page. Al+TiB_2 is imaged in the XY Plane highlighting the distribution in the channeling type porosity seen in the XZ cross-sections in Al+Al_2O_3 and Al+TiO_2.

Grain size was measured by optical and SEM microscopy of the material cross-sections and are presented in **Table 3.4**. The observed trend indicates that improved lattice matching of the nucleant phase results in reduced grain size of the printed material and lattice matched materials where either effective or not in the refinement of the microstructure. Additional studies of materials with intermediate matching between the thresholds tested may indicate a more uniform trend in lattice matching and grain size.

Understanding the dwell time of the inoculants in the liquid can provide insight into the nucleation rates of the different materials. In order to obtain a first order approximation of dwell times in the liquid state a Rosenthal solution calculation was performed for a variety of parameters (**Figure 3.8**)[51]. The Rosenthal solution calculates a three-dimensional temperature field as,

$$T = T_0 + \frac{Q}{2\pi k r} exp\left[\frac{-V(r+\xi)C_p\rho}{2k}\right] \quad \text{(Eq 3.1)}$$

where T_0 is the base temperature, Q is the heat input, k is the thermal conductivity of the

material, V is the beam velocity, C_p is the material heat capacity, ρ is the material density and $r = \sqrt{\xi^2 + x^2 + y^2}$ with ξ as the moving reference axis in the direction of the beam travel[51].

The Rosenthal solution is a highly simplified heat transfer solution for a moving heat source, and the solidus temperature isotherm (dashed line for aluminum in **Figure 3.8**) is not necessarily equal to the solidification front location or velocity. Since undercooling is required for nucleation and growth, the solidification front can lag behind the solidus isotherm by several degrees. Additional heat of fusion and phase transformations are not directly accounted for making the isotherm locations somewhat approximate. Despite this, the Rosenthal solution is likely within the right order of magnitude for relative isotherm location to provide an understanding of trends for liquidus dwell times and thermal gradients[108,144].

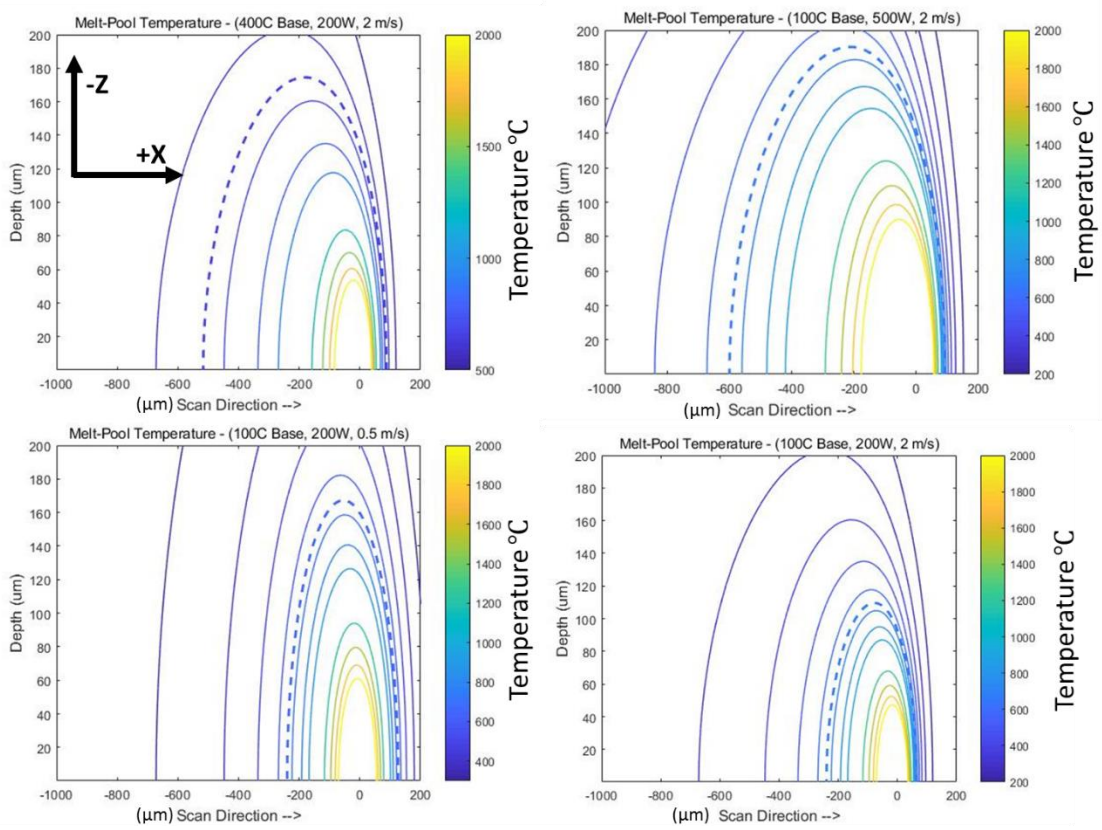

Figure 3.8: Thermal Profiles of an Aluminum Melt-pool Under Multiple Input Conditions. Plots are sectioned through the middle of the melt-pool in the XZ plane with beam travel io the right and beam incidence from the bottom of the page at (0,0). The simplified equation indicates the thermal field is symetric around the incident beam. The 660°C isotherm is highlighted as a dashed line. Input conditions are highlighted at the top of each graph and are provided to indicate trends in melt-pool size and shape under a variety of potential parametric additive conditions.

Assuming a constant scan velocity and steady state location of the isotherms, the time between two isotherms can be calculated using the distance between the isotherms and the beam velocity. This can be used to analyze the potential kinetic stability in the super-heated melt close to the laser as well as the time in an undercooled region assuming a set critical undercooling for nucleation, typically <10K. For an arbitrary depth in the melt-pool the time is calculated as, $\Delta L_{isotherm}/V_{beam}$, where $\Delta L_{isotherm}$ is the distance between two isotherms of interest perpendicular to the beam velocity vector. Calculating this for an estimated additive manufacturing condition typical for the Concept Laser M2, with an absorbed laser power of 200W moving at 1 m/s and a base metal temperature of 150°C

calculated 25 μm below the melt-pool surface, the approximate time in the melt is between 129 μs and 161 μs measuring from the point of beam incidence or the front of the melt-pool wave respectively. Additionally, the time in the undercooled region can be estimated between 0.26 μs and 2.65 μs for 1℃ and 10℃ critical undercoolings. The undercooled times along with the grain size of the resulting material can then be used to estimate the nucleation rates seen during processing where, $I = \rho_{grains}/t_{\Delta T}$. Here I is the approximate nucleation rate, ρ_{grains} is the number density of grains per unit volume after solidification, and $t_{\Delta T}$ is the time spent in the undercooled region of the melt-pool.

Table 3.4 highlights many of the important factors which were utilized in selection of nanoparticle inoculants. Nucleant space groups are provided to indicate the phase of nanoparticle used during processing, as many of the compositions can occur in different phases. For the Ta, Nb, and Zr samples the enthalpy of formation is provided indicating a high driving force for formation in the liquid aluminum[140]. As shown the increased tendency for lattice matching results in a decreased grain size and increased nucleation rate. The minimum lattice matched families of planes are shown, however in most cases additional matched planes existed at different Miller indices. The minimum mismatch plane is likely to produce the least amount of strain energy and therefore provide the lowest energy barrier to nucleation, as will be highlighted in Chapter 4.

Table 3.4: Nucleant Lattice Matching and Properties of 1 vol% Additively Manufactured Material. Minimum lattice mismatch is calculated by the previously described lattice matching criterion. Grey boxes indicate where no lattice matched data was identified from the 5% matching criteria imposed in the lattice matching software. Orange boxes indicate where data was not gathered due to difficulties in preparing samples. Grain size is in the as printed state.

Nanoparticle	Nucleant	Nucleant Space Group	Formation Energy (-kJ/mol)	Minimum Lattice Mismatch					Microhardness (HV0.2)	Grain Size (µm)	Approximate Nucleation Rates
				%	Al Plane (hkl)	Al Plane Density (atoms/Å^2)	X Plane (hkl)	X Plane Density (atoms/Å^2)			
N/A	Pure Al	Fm-3m	N/A						37.4	200 - >1000	$<3*10^{16}$
TiB_2	TiB_2	P6/mmm	N/A						39.3	200 - 1000	$\sim3*10^{16}$
Al_2O_3	Al_2O_3	Fd-3m	N/A						34.8	200 - 1000	$\sim3*10^{16}$
TiO_2	TiO_2	$I4_1/amd$	N/A	3.58	111	0.142	112	0.067			
WC	WC	P-6m2	N/A	2.18	100	0.123	100	0.120	57.1	4 - 8	$1.7*10^{22}$
TiC	TiC	Fm-3m	N/A	3.87	311	0.074	001	0.213			
Ta	Al_3Ta	I4/mmm	122	1.35	110	0.087	012	0.090	54.35	2 - 5	$1.4*10^{23}$
Nb	Al_3Nb	I4/mmm	163	1.56	110	0.087	012	0.090	47.3	4 - 6	$3.1*10^{22}$
Zr	Al_3Zr	I4/mmm	187	0.52	100	0.123	001	0.124	44.5	3 - 6	$4.2*10^{22}$

There is not a clear linear trend between lattice strain and grain size as might be expected from nucleation theory, however this is somewhat expected, as nucleant surface energies along with dissolution and reaction of some precipitates in the elevated melt-pool temperatures result with different degrees of solute undercooling behavior ultimately leading to differences in nucleation behavior. While this generally demonstrates the importance of lattice matching to ease of nucleation and growth, the complete physics of the nucleation and growth mechanism is not fully apparent from these experiments. These experiments indicate that a high degree of lattice matching is important, but not a sufficient metric for selection of inoculants. An understanding of solute effects, along with the thermodynamic and kinetic stability of the inoculant phases, is needed develop further predictive capability. This will be discussed in more detail in the next chapter.

Chapter 4

Grain Refinement in the Unalloyed Aluminum System

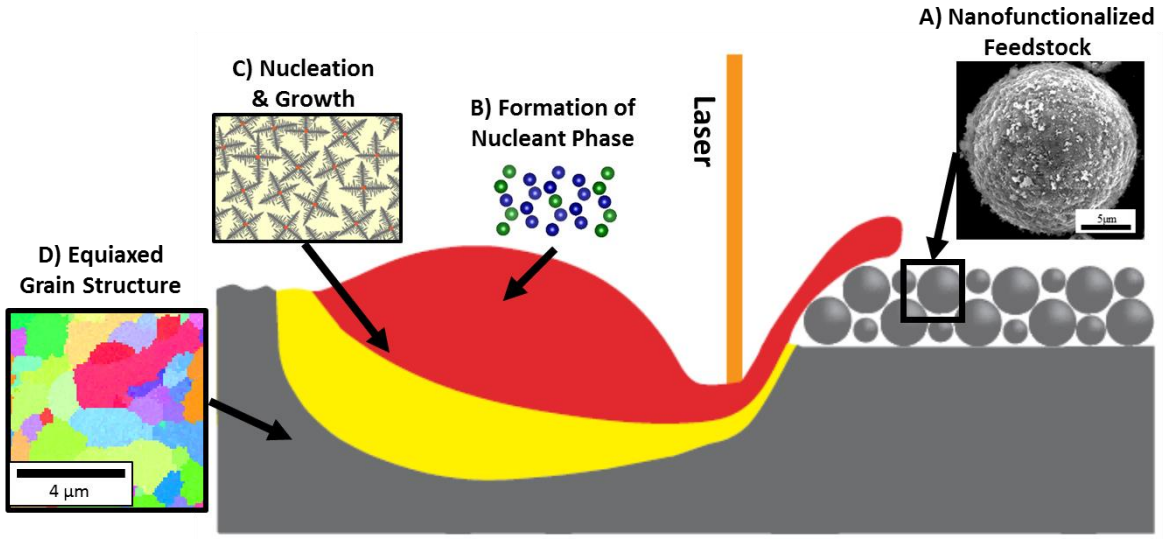

Figure 4.1: Process of additive manufacturing with nanofunctionalized powders. Laser scanning left to right, **A)** incorporating nanofunctionalized powder during laser powderbed fusion, **B)** reacting with the nanoparticles on the surface of the alloy powder to form a targeted nucleant phase in the melt (red), **C)** promoting heterogeneous nucleation, D) leading to an equiaxed final microstructure in the printed part.

The general solidification behavior during additive manufacturing along with typical inoculated melts under casting conditions has been described mostly independently in previous chapters. This chapter will focus on how a combination of inoculation and the unique solidification conditions in additive manufacturing can be leveraged to control microstructure during solidification. As will be described, this is not only a combination of solute effects mentioned in Chapter 2, but also the impact of crystallographic misfit on inoculant effectiveness discussed in Chapter 3. This will be explained in relation to a model Al-Al_3Ta nucleant system. The applicability to other Al_3X peritectic nucleant systems for aluminum alloys will also be addressed.

Recently, work by Martin et al.[145] has demonstrated that nanofunctionalization of input powders can be utilized to control solidification during additive manufacturing in a parameter agnostic manner through targeted inoculation and nucleation control, **Figure 4.1**. Here a comprehensive description of the nucleation physics is described for a model additive aluminum system. It is demonstrated that with targeted control of nucleant density and activity along with appropriate thermodynamic and kinetic driving forces, the microstructure of additive alloy systems can be controlled. The microstructures which develop and ultimately dominate the material properties are derived from nucleation and growth events in the melt-pool. As such, understanding and controlling these nucleation events would provide a comprehensive tool for microstructure control.

The dependence of as-solidified microstructure at the micrometer to millimeter scale is well known to be sensitive to the thermal gradients and solidification velocity and is well established in the literature[69,70]. The most applicable model for prediction of grain structure during additive manufacturing is the columnar to equiaxed transition (CET)[33], as described in Chapter 2. Due to the layered approach to additive manufacturing, columnar growth is generally the most favorable growth mechanism, with grain selection and epitaxial growth from the previous layer[100]. While columnar microstructures have some benefits for some industrial applications, such as directionally cast turbine blades, elastic and plastic anisotropy in the crystal structures of many base metals (Iron, Nickel, Titanium) can result in a component with anisotropic material properties, making component design extremely difficult[100,146]. A transition to fine grained equiaxed microstructures provides many material property benefits including increased strength, fatigue life, ductility, and reduced

crack susceptibility. As such, much of the current research in additive microstructure control is devoted to pushing the G-V processing window beyond the CET.

Issues with microstructure control are not limited to additive alloy systems and processes. As previously described, cast alloys have similar challenges related to microstructure control due to imposed thermal conditions from mold geometry and casting temperatures. Inoculation has been used to overcome this and produce castings with uniform equiaxed grains under a variety of thermal conditions[39]. The most studied system along conventional casting routes is that of aluminum alloys with TiB_2[59,95]. The TiB_2 particles act as heterogeneous nucleation sites, seeding new grains ahead of the solidification front and interrupting growth of the columnar structure.

4.1 Role of Solutes in Inoculation

The exact mechanism of heterogeneous nucleation in the TiB_2 system is still debated[93,94,147]. Multiple explanations have been proposed and their extrapolation to other systems has been limited. While inoculation is currently limited to a few alloy systems, the ability to take advantage of heterogeneous nucleation across all alloy systems as a mechanism for microstructure control has potential not only for additive manufacturing but all existing and future liquid-based metallurgical processes. One of the original proposed inoculation mechanisms indicated that the TiB_2 particle surfaces form an Al_3Ti intermetallic which acts as the actual site where nucleation occurs, **Figure 4.2**. This was supported by simulated and experimental results indicating formation of a monolayer of Al_3Ti on the [0001] TiB_2 plane[92], see Chapter 2. Additionally it was shown that increasing the solute content of titanium in the aluminum melt decreased the critical undercooling of the TiB_2 particles[95,96].

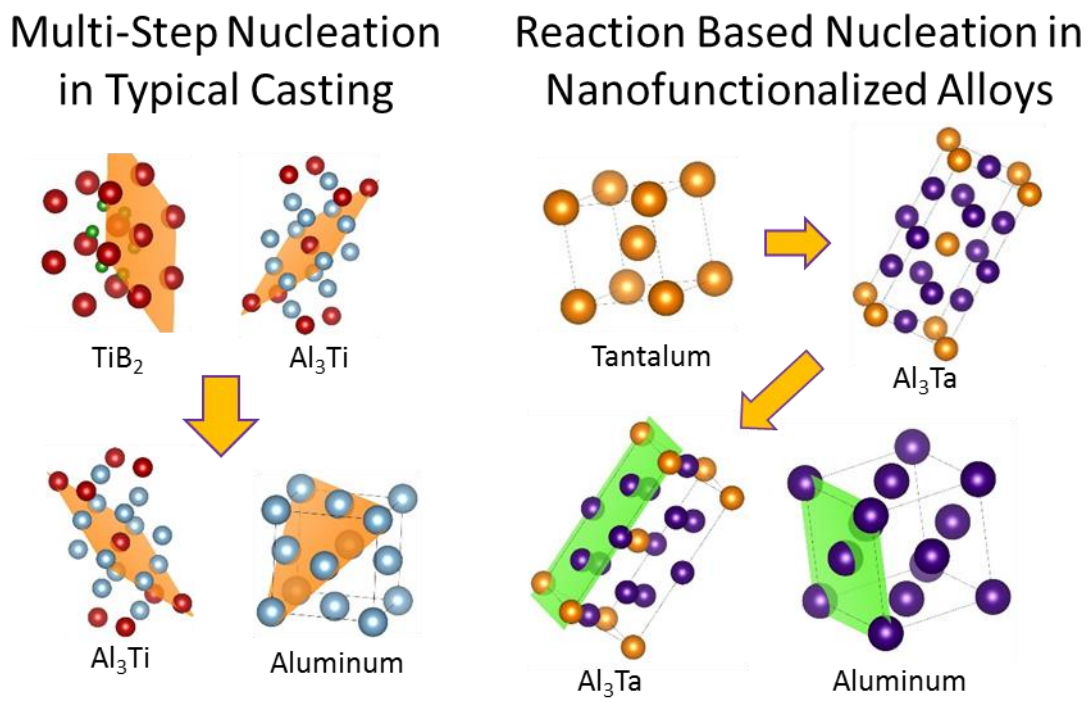

Figure 4.2: Heterogeneous nucleation process. (Left) Typical nucleation process in inoculated aluminum castings in which TiB_2 particles form a mono-layer of Al_3Ti which then promotes nucleation of FCC aluminum. **(Right)** Reaction nucleation seen in this study during additive manufacturing of nanofunctionalized aluminum alloys in which a solid state or dissolution and nucleation event occurs forming an Al_3X intermetallic which directly promotes nucleation of FCC-aluminum. A potential growth direction of (001) is indicated, however multiple lattice matched orientations exist due to the FCC and ordered tetragonal relationship between Al and Al_3Ta. Crystal structures extracted from the Materials Project[139].

Alternatively, this concentration effect has been attributed to the growth restriction factor (GRF) originally discussed by Johnsson[148] and further developed by Easton and St. John[78]. The GRF is used to estimate the effect of solute elements on restricting the growth of the solid via segregation. This, however, fails to account for many other effects such as attachment kinetics and solid-liquid surface energy. The GRF is inversely related to the ability to form a constitutionally supercooled region in front of a growing solid[149]. Utilizing the equilibrium phase diagram one can calculate the growth restriction factor for an individual alloying element as ($Q = c_0 m(k-1)$). Where Q is the GRF, m is the gradient of the liquidus, k is the partition coefficient ($k = c_s/c_l$), and c_0 is the composition of the solute. As would be expected high concentrations of solute and a steep liquidus slope would

result in high levels of constitutional undercooling. Noticeably absent from this is any diffusion term and is thus applicable for initial establishment of the undercooled region in a diffusion limited regime[149]. The effect of small solute additions is dominated by the relatively constant $m(k-1)$ term. For simplicity this term will be referred to as the growth restriction coefficient (GRC_x), where $_x$ is the solute element being described. Common values for these calculations can be derived from the example equilibrium phase diagram in **Figure 4.3** for common peritectic elements in the aluminum system[81,130,150,151].

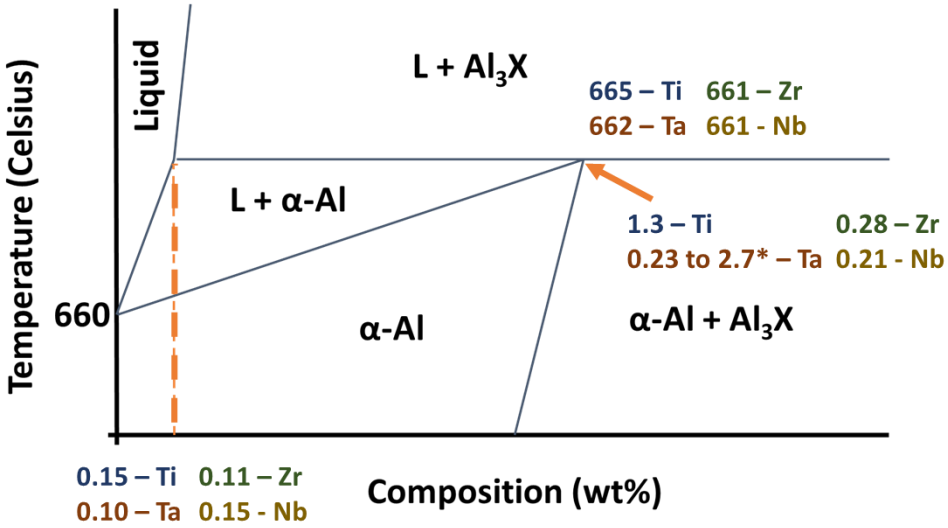

Figure 4.3: Exaggerated Aluminum Rich Phase diagram for common Al_3X Peritectics. Individual values for critical intercepts are labeled for each metal[130,149]. *Ta has substantial deviation in the composition of the peritectic point[151]

During solidification in the Al-Ti system, growth of the solid phase is restricted through solute accumulation in the solid via a k~9 wt%/wt% and high positive value for m~30 °C/wt%, producing a GRC_{Ti} of ~240[95]. This can then be compared to the typical undercooling criteria where[77]:

$$G < \frac{c_0 m(k-1)}{k}\frac{v}{D} \quad \text{(Eq 4.1)}$$

Where v is the solidification velocity and D is the diffusivity of the solute in the liquid. For

undercooling to be present, the gradient associated with the equilibrium liquidus temperature, for a plane front condition, must be greater than the thermal gradient G, **Figure 4.4**. At a given solidification velocity, assuming that the atomic diffusivities of Ti, Zr, Nb, and Ta in solution are similar (~10^{-9} m^2/s)[152], the main driving force for undercooling is Q/k. While titanium has a high GRC_{Ti}, the low solubility (~0.15 wt%) and k >1 partition coefficient provides a maximum Q/k of ~4. Conversely common alloying elements like Cu and Mg have relatively low GRC values at 2.8 and 3, respectively. However a high potential liquid solubility and <1 partition coefficient results in greater Q/k values. Many 7000, 5000, and 2000 series aluminum alloys have >2 wt% of these elements either in combination or individually, where at 2 wt% the Q/k values can be ~33 for Cu and ~12 for Mg[81]. While the magnitude of Q/k for Ti is between 10 and 4 times lower than what is typical for other aluminum alloying elements, the value is not insignificant given the low weight percent in the alloy.

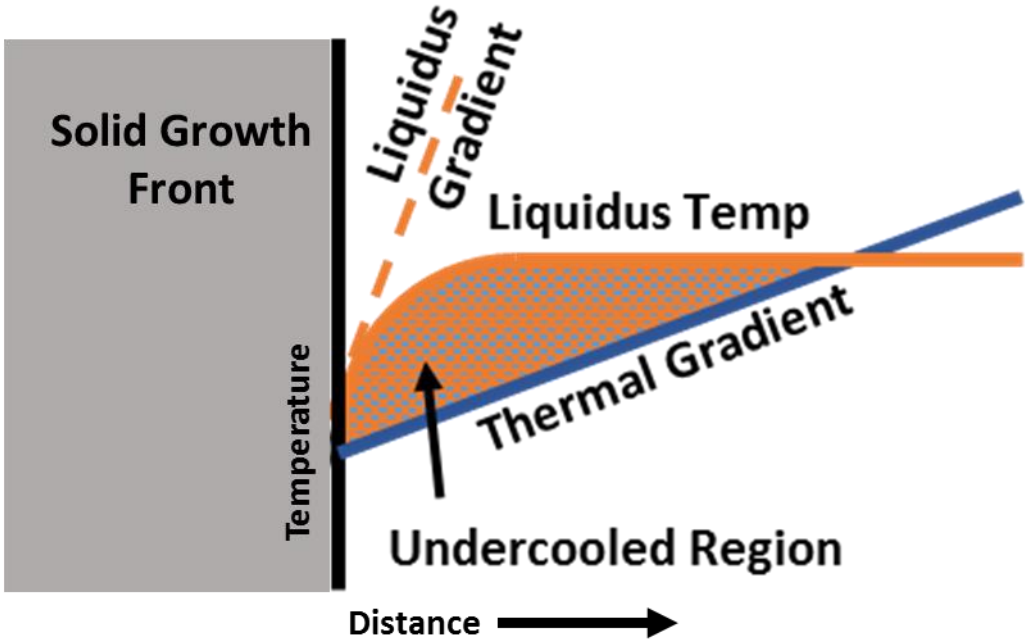

Figure 4.4: Constitutional Undercooling Schematic. Illustration of the evolution of undercooling during solidification where when the liquidus gradient is greater than the thermal gradient an undercooled region can form.

The true impact of the GRF on nucleation is difficult to decouple from other phenomenon such as attachment kinetics, change in the solute-influenced solid liquid surface energy, and secondary phase formation, which would introduce a local latent heat in the system. Additionally the value of the GRF is highly dependent on the accuracy of the equilibrium phase diagram in a very dilute composition range for the more potent peritectic elements, where 0.5°C variations in local liquidus temperature or >0.1 wt% changes in solubility can have significant impacts on the GRC value, **Figure 4.3**. Furthermore the applicability to additive manufacturing is less clear, as small-scale dendrite radii may induce minor (but significant for GRC calculation) changes to the free energy equations of state due to the Gibbs-Thomson effect.

The incorporation of the GRF does not preclude the previous multistep Al_3Ti-TiB_2 nucleation phenomenon and serves more as an additional phenomenological description rather than a clear design criteria for nucleation. Crystallographic analysis of the Al-Al_3Ti-

TiB_2 nucleation stack provides some insight into the driving force for this process. The aluminum FCC crystal structure requires a >5% areal lattice strain, defined in Chapter 3, when matched to any of the TiB_2 crystal interfaces, leading to the addition of strain and inevitable misfit dislocation energy into the nucleation barrier. As originally described by Turnbull[67], heterogeneous nucleation is driven by a decrease in the energy penalty associated with forming the new phase as described in Chapter 2, however the effect of the substrate has been limited to wettability as in $\Delta G_{het} = \Delta G_{hom} \cdot f(\theta)$, where $f(\theta)$ is related to the wettability of the substrate[51]. Taking these additional energy penalties into effect and lowering cumulative energy penalty from the phase formation can further decrease the critical radius required to induce growth as well as the critical undercooling. Critical undercooling in most metal systems is typically only a few degrees Celsius making the impact of these secondary effects important when trying to initiate nucleation and growth under the fast solidification conditions characteristic of additive processes[88].

The formation of the Al_3Ti monolayer on the 0001 TiB_2 interface leads to a decrease in strain accommodated for nucleation of the FCC aluminum phase. The {112} Al_3Ti lattice has a combination of low areal strain to the TiB_2 {0001} interface and the {111} aluminum FCC lattice **Figure 4.2**[51]. This reduces the total strain of the system and reduces the frequency of misfit dislocations or vacancies, ultimately lowering the energy barrier to nucleation and growth. The observed increases in nucleation activity with increasing titanium content can then be attributed to increased local concentration of titanium relative to that required for formation of the stoichiometric intermetallic at the TiB_2 interface where additional titanium has been shown to dissolve into the liquid likely producing a high

enough Ti concentration at the interface to push the local equilibrium into the Al-Al_3Ti two phase region[59,153].

When trying to identify new grain refiners for additive manufacturing a combination of the above effects was incorporated to a search approach for a series of possible nucleants. While edge to edge lattice matching, discussed in Chapter 2, has been used to identify grain refiners before, this is limited as it does not take into account atomic density of the lattice plane or the effect of non-parallelepiped crystallography[90,97]. A new software tool that identifies matching crystallographic lattice spacing and densities to provide a low energy nucleation barrier was utilized[135]. The software, described in Chapter 3, analyzed over 4,500 different crystal structures of powder and nanoparticle combinations corresponding to over 11.5 million matching pairs. Minimized lattice misfit, similar atomic packing along matched crystallographic planes, thermodynamic stability in the desired alloy, and availability were factors used to identify potential matches. While aluminum was the focus of this study, grain refinement systems for other high value alloy systems were identified including those of Iron, Nickel, and Titanium.

4.2 Inoculation of Unalloyed Additive Aluminum

As expected the search algorithm found that the Al_3Ti system was lattice matched to both TiB_2 and FCC-Al, however FCC-Al did not fall within the parametric constraints to show any lattice matching to the TiB_2 structure. In addition to the Al_3Ti system, several other Al_3X phases where identified (X = Zr, Ta, Nb). All of these alloying elements have a similarly structured peritectic phase diagram in the aluminum rich region of the phase diagram **Figure 4.3**, with Titanium and Tantalum having a relatively high GRC (GRC_{Ti}~240, GRC_{Ta}~105), while Zr and Nb are low (GRC_{Zr}~6.8, GRC_{Nb}~6.6). In order to

rapidly analyze these systems, a nanofunctionalization approach was used, **Figure 4.1**, in which nanoparticles of the associated elemental species are assembled onto the surface of spherical >99% aluminum micro-powder from Valimet (average particle size of 45um). The procedure of which is described in Martin *et al*.[135] The nanoparticles used were Ta (50-80nm), ZrH (<1 micron hydrogen stabilized to reduce air reactivity, Nb (50 nm), and Ti was not tested due to safety associated with co-processing Ti nanoparticles with Al under potential air exposure. The nanoparticle compositions where chosen in order to form the identified Al_3X phases (X= Ta, Zr, Nb) which showed high lattice registry. Nanofunctionalization allows for easy analysis of varying compositions without the need for custom alloy production. Tantalum was chosen as the model system for additional study due to the purity of the feedstock (>99.99%), high Z-contrast in electron imaging, and slow solid state diffusivity to avoid microstructure evolution during the build ($<10^{-12}$ cm^2/s at room temperature based on similar diffusivity data for the Al-Zr system)[81] which was expected to aid in maintaining the as-built microstructure throughout processing and analysis. Unfortunately no valid data for the diffusivity of Ta in Al was readily found, however, given the similar atomic size ratios and electronic structure of Al and Zr the low diffusivity is expected to correlate closely.

The combination of nanofunctionalization and additive manufacturing allows introduction of these elements at compositions beyond their conventional limits in aluminum alloy processing (typically <0.15 wt%). This limit is driven by the extremely high superheat during casting (>1000℃ casting temperature) required to fully dissolve these peritectic elements at elevated concentrations. Due to the short liquid dwell times on the order of <100 μs (calculated in a later section), intermetallic coarsening is suppresed, which is

difficult to achieve in conventional casting or powder atomization techniques without high superheats (>300°C over liquidus)[150] and fast quenching (>10^3 °C/s)[39]. Additionally powder feedstocks of aluminum with 1 vol% 58nm TiB_2 (the most common aluminum inoculant[154]) and 1 vol% 20nm Al_2O_3 (a common component in stir cast metal matrix composites[118]) were produced via nanofunctionalization. A list of all materials investigated is shown in **Table 4.1**. Neither the TiB_2 or Al_2O_3 systems was demonstrated to have acceptable lattice matching, defined as <5% areal strain, to induce nucleation, but were tested due to their practical use in current casting processes.

Table 4.1: Tested nucleants in this study. Actual weight % shown when verified by ICP-AES, *vol % equivalents adapted based on actual weight % measured by ICP.

Nucleant Added	Tagret Nucleant Phase	wt% Added	Actual wt%	vol% Equivalent
Pure Al				
TiB_2	TiB_2	1.65	N/A	1.00
Al_2O_3	Al_2O_3	1.44	N/A	1.00
ZrH	Al_3Zr	2.35	N/A	1.00
Nb	Al_3Nb	3.07	N/A	1.00
Ta	Al_3Ta	5.8, 2, 1, 0.5, 0.25, 0.1	5.4, 1.98, 0.95, 0.5, 0.24, 0.1	0.93, 0.32, 0.15, 0.08, 0.04, 0.017*

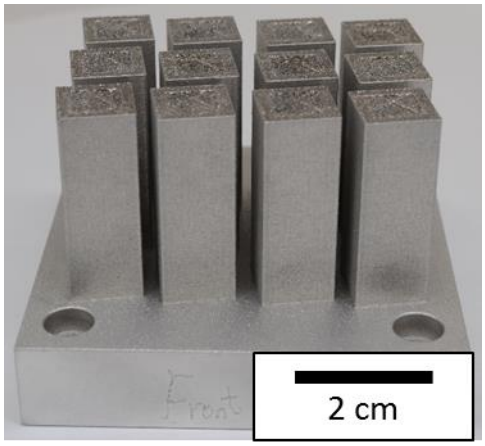

Figure 4.5: Example of 3D printed structures used in this study. Material was printed and excised for analysis.

Each batch of feedstock was 3D printed in a Concept Laser M2 under an inert atmosphere. The inert atmosphere was either nitrogen or argon and oxygen content was maintained below 0.2%. Argon was used when the nanoparticles had a thermodynamic driving force for the formation of nitrides[140], (i.e. ZrH, Nb, Ta) otherwise nitrogen was used (Pure Al, TiB_2, Al_20_3). The build was designed to produce several microstructural samples, **Figure 4.5**, to analyze and used the stock parameters provided by the manufacturer, Concept Laser, for additive manufacturing of the commercially available CL31 powders, an Al10SiMg alloy system. This provided a parameter set that was known to melt aluminum alloys and eliminated the need to develop a new parameter set. Utilizing an identical processing configuration for all samples ensured that the solidification conditions were as identical to each other as possible. This forced any change in microstructural features to be driven by the introduced nanoparticles and not the associated solidification conditions.

During processing the laser creates a depression melting into the previous layer and inducing a bow wave of liquid which pulls the nanofunctionalized feedstock material into the main body of the meltpool[104], **Figure 4.1**. Marangoni effects along with laser induced recoil pressure produce a turbulent meltpool with relatively high fluid velocities (>1 m/s)[60]. This provides an ideal environment for uniform distribution of potential nucleants. In the case of the chosen Al_3X nucleants with high lattice matching a reaction with the elemental nanoparticles is required to form the target phase. This can occur either as a solid state reaction on the surface of the particle or through full dissolution and nucleation of the target phase. The latter is more likely for the smaller particulate due to the high surface to volume ratio driving dissolution combined suppressed melting points related

to the Gibbs-Thompson effect. Local concentrations of solute are then highly likely to nucleate the target Al_3X phase due to the high undercooling (>600℃ vs equilibrium phase melting points of the high temperature Al_3X phases typical >1400℃)[81,130]. There is some support for this theory in the Al-Ta system, as will be discussed in more detail below. In the case of the non-lattice matched nucleants (TiB_2 and Al_2O_3) no reaction is expected in the case of Al_2O_3, and for TiB_2, the high temperature stability, short melt dwell times, and high mixing rates are not likely to provide the kinetic environment for formation of the Al_3Ti reaction phase on the TiB_2.

Cross sectional views of the printed material shows very clear variations in microstructure developed in the baseline pure aluminum and 1 vol% nanofunctionalized material, **Figure 4.6**. The unalloyed aluminum with Al_3X nucleants, (**Figure 4.6 D,E**), possess a high density with some residual gas porosity, while the non-lattice matched particulate alloys, (**Figure 4.6 B,C**), exhibit large columnar voids and cracks persisting through the entire build height. Given the relationship between particle wettability and associated surface energy[137] it appears that the lack of appropriate lattice matching also leads to an inability to produce a stable melt pool where unwetted particulates induce voids and cracks possibly due to difficulties in the formation of a stable weld-pool. While pockets of higher bulk density and reduced grain sizes were seen in the TiB_2 system there are no such areas in the Al_2O_3. This likely indicates that in some cases there was enough time for reaction of the TiB_2 to create the targeted Al_3Ti phase. The results indicate that as a metric for incorporation via nanofunctionalized additive manufacturing, the lattice misfit present in the Al_2O_3 and TiB_2 is a good approximation for determining whether a nanoparticle system can be incorporated into additive aluminum without significant issues with particle wetting

and void formation. The additional lack of noticeable grain refinement provides further evidence of the potential importance of crystallographic misfit, at least in the solidification conditions present during additive manufacturing.

Parameters were not optimized for this study, and some combination of parameters may be appropriate to improve the quality of the high lattice misfit material, however the comparable success of the low lattice misfit refiners indicates that this approach is much more favorable for further study. The Al-Al_3Ta system, in particular, showed the best grain refinement tested along with the highest hardness. Additionally, channeling contrast in the electron backscatter imaging modality indicates that the tantalum rich phase is present in the center of the grains as evident by the bright contrast in many grains, **Figure 4.6 E**. The presence of bright spots in every grain is unlikely due to the stochastic nature of the grains and inability to bisect the nucleant center of each grain. As previously discussed, this type of imaging is made possible by the high z-contrast between tantalum and aluminum.

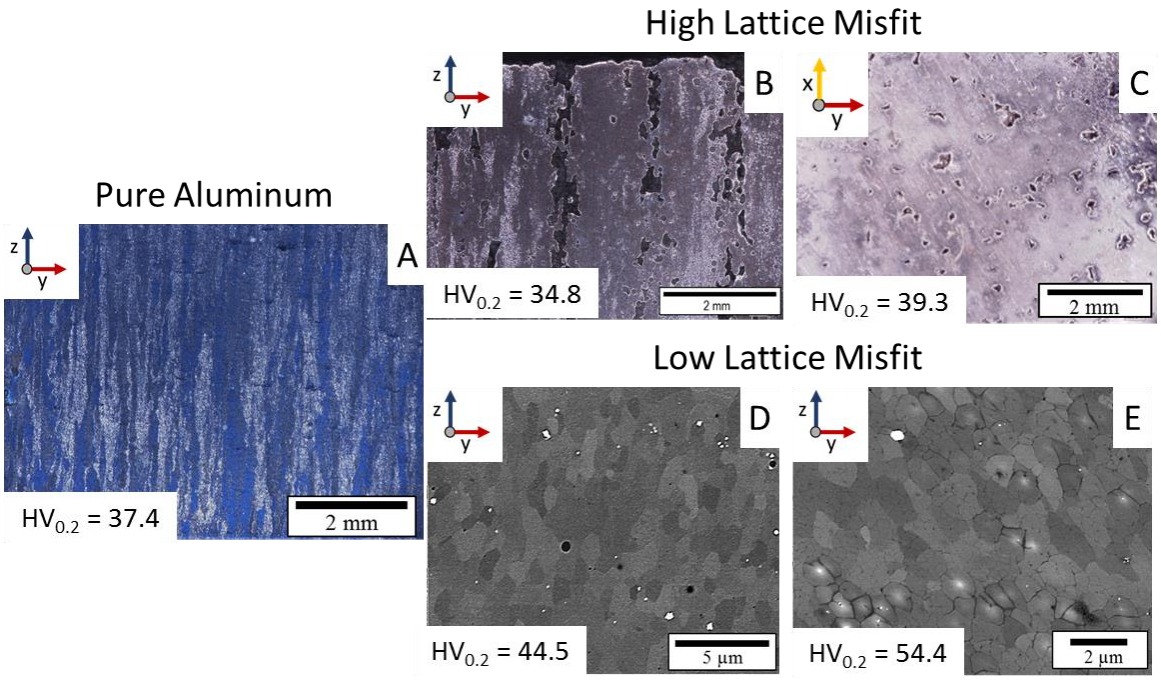

Figure 4.6: Micrographs and Vickers Hardness of 3D printed materials. (A) Pure aluminum indicating large columnar growth in the Z direction (**Top**) Optical micrographs of material printed with high lattice misfit nanoparticles (**B**:1 vol% Al_2O_3 & **C**:1 vol% TiB_2) indicating large columnar growth with porosity. (**Bottom**) SEM micrographs on material printed with nanoparticles designed to produce low lattice misfit nucleants (**D**:1 vol% ZrH & **E**:1 vol% (5.8 wt%) Ta), indicating significant grain refinement.

Taking a closer look at the grain refinement in the Al-Al_3Ta system as compared to pure aluminum in **Figure 4.6**, there is an approximate 1000X decrease in grain size. This was relatively consistent regardless of the Al_3X nucleant (X= Zr, Nb, Ta), however the tantalum system does show slightly lower grain size and increased hardness over the Zr and Nb systems (also discussed in Chapter 3). The inverse pole figure (IPF) maps in **Figure 4.7** demonstrate the high variability in microstructure possible by introduction of nucleating phases. The pure aluminum is highly textured with the <101> direction parallel to the build direction, likely due to angled growth from the back of the half-hemisphere melt-pool with significant inclination between the melt pool surface and build direction, as the <100> growth direction is generally the most favorable growth orientation for FCC-Al[155]. Additionally there is significant rotational misorientaion in the grains likely due to the

change orientations in the heat flux due to the rastering nature of the beam during the build[155]. During the additive process, each laser pass melts into the previous layers, sometimes by >2 layers (>50 μm). Because the laser may be traveling in a different direction than that which established the previous layers, as described in Chapter 1, the thermal gradients may have very different vector orientations compared to that present in previous layer growth. As the layer epitaxially grows off the previous layer, the preferential growth will still be in the direction of the thermal gradient, promoting growth along the crystal orientations, creating misorientation. This is a likely cause of the apparent waviness in the [100] and [010] reference orientations in the IPF maps in **Figure 4.7**. Conversely the Al_3Ta inoculated materials show highly refined grains with little to no misorientation within the grains and no observable texture relationship to the heat source.

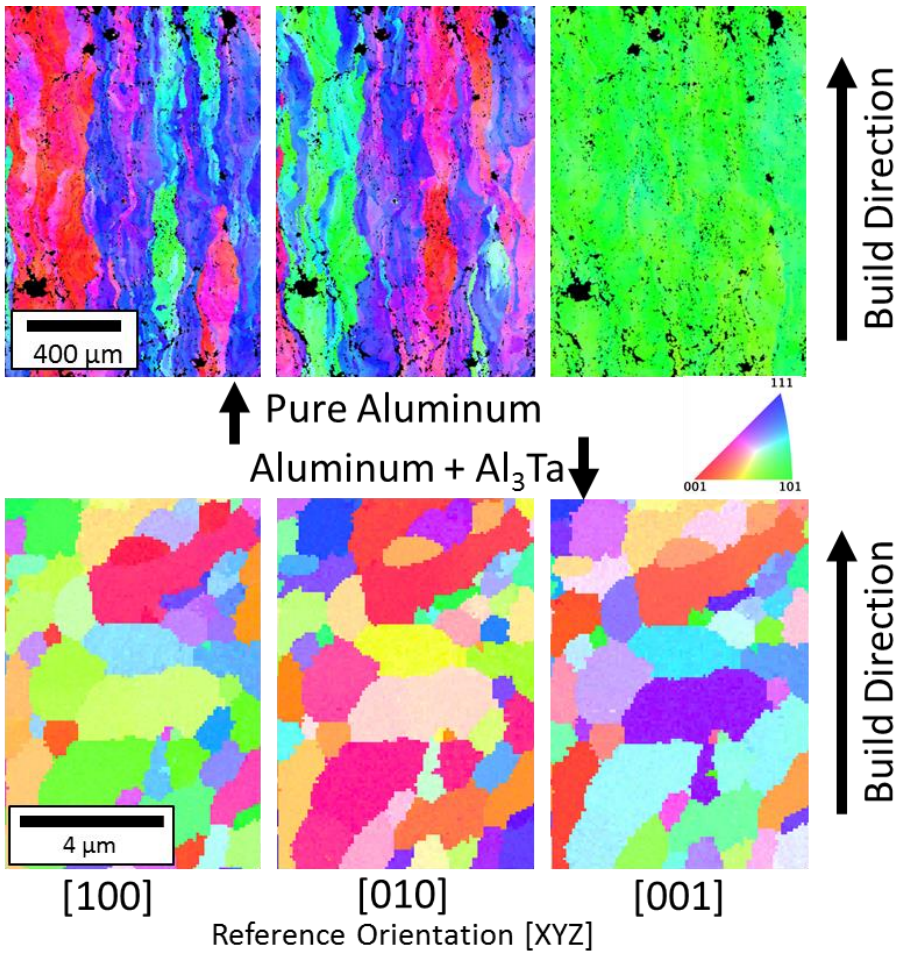

Figure 4.7: Inverse pole figure maps of printed material. (Top) Pure aluminum indicating a highly textured material with significant grain rotation. **(Bottom)** Al + 1 vol% (5.8 wt%) Ta indicating more equiaxed grain structures with a random texture.

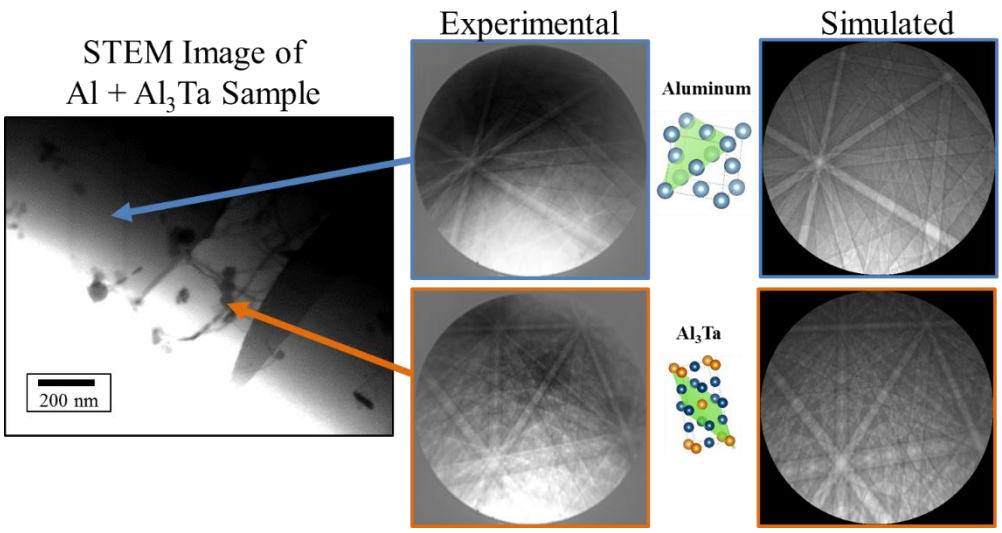

Figure 4.8: Scanning Transmission Electron Microscopy (STEM) and Transmission Kikuchi Diffraction (TKD) of Al + 1 vol% (5.8 wt%) Ta. STEM image shows nanoparticles are mostly in the grain centers indicating the location of nucleation. Experimental and Simulated TKD patterns of the grain and nanoparticles indicate a phase match to the expected crystal structures. Simulations were completed as described in Pascal et al.[156] and Callahan & De Graef[157].

Given the high observability of the tantalum phase, a sample was prepared for TEM and STEM. To confirm the lattice matching effect two different techniques where used, diffraction in TEM and zone axis alignment in TKD, **Figures 4.8, 4.9 & 4.10**. Imaging and diffraction analysis indicates that the resulting alloy contains two distinct phases, with the second phase present throughout the structure. Transmission Kikuchi Diffraction (TKD) was used to identify the phases as Al_3Ta and FCC Al phase. This was further confirmed using simulated TKD patterns for the predicted crystal structures of these phases and matching them to experimental patterns, **Figure 4.8**. XRD was also completed to confirm the phase formation as will be discussed in a later section.

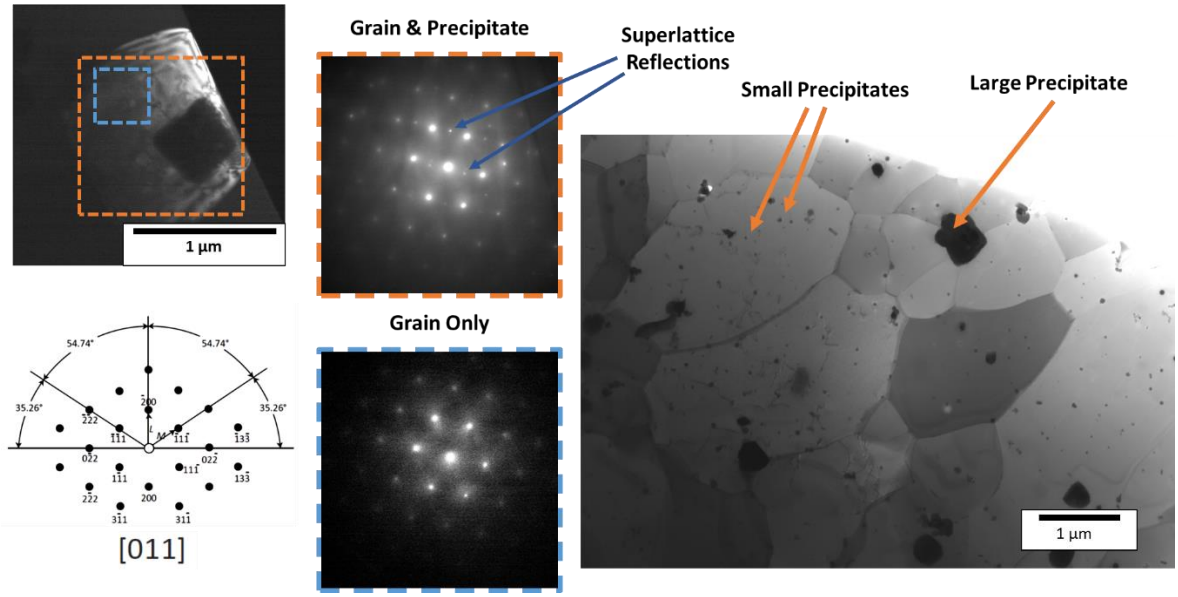

Figure 4.9: Transmission Electron Microscopy (TEM) and STEM images of Precipitates and Grains. (Left) TEM images and diffraction patterns indicating a coherent precipitate system (Orange box) imbedded in an FCC aluminum grain (Orange and Blue box). Characteristic secondary superlattice reflection peaks are seen in the large area diffraction pattern typical of the ordered Al_3Ta precipitate, along with pattern alignment with the grain indicating a highly similar lattice parameter. A standard [011] diffraction pattern is provided[158], indicating alignment of the grain and precipitate along the [011] direction. **(Right)** There is a distribution of both large and small precipitate systems, in which the large precipitates tend to be near grain boundaries and the small precipitates have cubic geometries distributed throughout the grains.

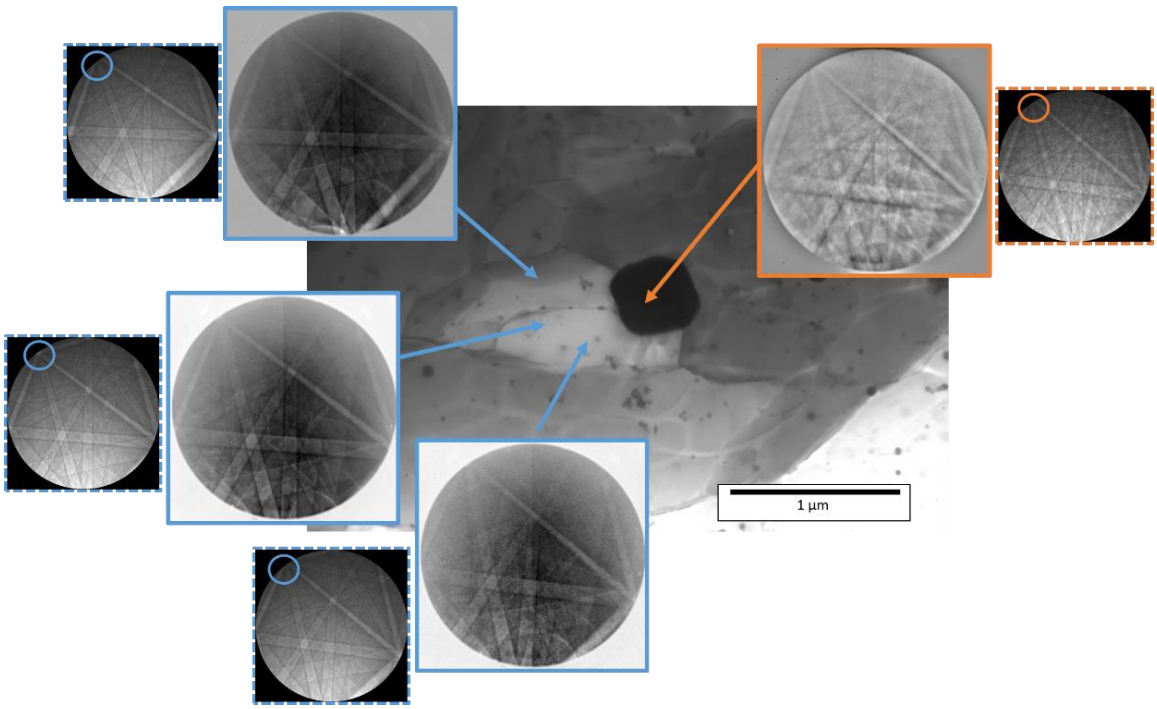

Figure 4.10: STEM and TKD of Precipitate and Grain. Additional microscopy of a large precipitate system indicates that the TKD diffraction patterns can be used to indicate a coherent interface as the aluminum grain (TKD in Blue) show an aligned zone axis with the Al_3Ta Precipitate (TKD in Orange). Simulated patterns are also provided (dotted boxes) along with indications of the [110] zone axis (circles). Simulations were completed as described in Pascal et al.[156] and Callahan & De Graef[157].

The diffraction patterns in TEM **(Figure 4.9)** indicate that the Al_3Ta intermetallic which is present may have a similar lattice parameter to that of the aluminum matrix as evident from the diffraction spot spacing between the two diffraction patterns. The pattern which includes the grain and precipitate show characteristic secondary reflections indicative of an ordered structure. It is particularly interesting that the orientation relationship between the Al_3Ta and the FCC Aluminum phase is related to the [011] orientation. The cuboidal nature of the second phase would seem to imply a [001] orientation in which the cubic faces are all similarly oriented. The [011] relationship is unexpected as it relates to the morphology, but not unanticipated when accounting for the lattice misfit between the Al_3Ta and Al phases. As described in Chapter 3, the Al-Al_3Ta system has the lowest lattice misfit in the [011] family of planes. Additional analysis is likely needed to validate the most common

orientation relationships seen between the precipitates and the matrix. It is possible that cube on cube symmetry exists, but is inconclusive with the available diffraction data. This is further evidence of the impact of crystallographic relationships on nucleation behavior.

The TKD analysis, **Figure 4.10**, provides additional evidence of specific orientation relationships indicative of lattice matched nucleation and growth. While direct lattice parameters are not as easily determined from this method, the alignment of zone axis can be observed indicating a crystallographic relationship between the grain and the precipitate system. This also appears to show a strong relationship in the [110] zone axis providing additional support to the importance of crystallographic misfit in nucleation. Knowing the expected crystal structures and lattice parameters, one can conclude that these aligned orientations are in fact indicative of crystallographic driven nucleation and growth. Given the large imaging area, and relatively quick data collection rates of TKD versus TEM diffraction patterns, it is possible that this methodology may be applicable to analyze statistically large data sets of precipitate matrix orientation relationships to better understand the effect of precipitate or inoculant crystal orientation and that of the solidified material.

The size distribution of particulate is also of interest. Analysis was mostly confined to the larger precipitates, however a significant number of secondary small precipitates (<200 nm) exist throughout the grain structure. It is expected that, as with the large precipitates, these are coherent within the matrix. Additional analysis is likely needed to understand the varying roles of the different size precipitates on the nucleation process, however a first approximation of the potential activity of these small particulates (radii <50 nm) can be determined analytically using a combination of the free growth model and potential undercooling during solidification.

As discussed in Chapter 2, the free growth model indicates that nucleation on particles this small (<50 nm) can require a substantial amount of undercooling (>10℃)[85]. The potential undercooling available in an Al-Ta alloy system can be calculated for the maximum solubility of Ta at the equilibrium temperature of Al solidification (0.1 wt%, 0.02 at%) and compared with that of 3 wt% copper in Chapter 2 (**Figure 4.11**).

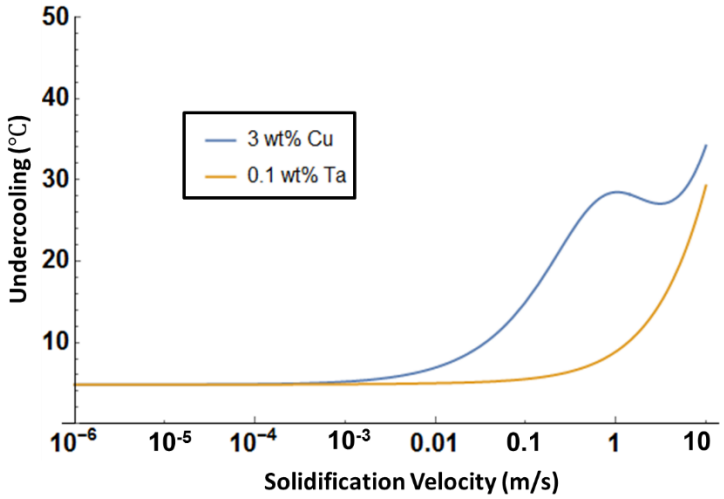

Figure 4.11: Undercooling at 100nm characteristic radii for 3wt% copper and 0.1wt% Ta. Diffusion velocity for Ta was not known and assumed to be half that of copper, however the >1 partition coefficient for Ta implies the solute trapping effect is of less importance based on the Aziz equation[76].

Due to the lower solubility and therefore lower GRF value for the tantalum, substantially higher solidification velocities are needed to induce an increased level of undercooling. As also discussed in Chapter 2, this may indicate that critical undercooling for nucleation may not necessarily be dominated by inoculant radii, as implied by the free growth model, but is instead related to the interaction with the substrate and associated stain impact on the free energy. The number and distribution of the large Al_3Ta phases do not seem to account for all potential nucleation events and it is likely that these smaller Al_3Ta phases are active nucleants, however additional study is needed.

4.3 Analysis of the Aluminum Rich Al-Ta System

The success of the 1 vol% (5.8 wt%) Ta inoculant prompted further research into the effectiveness of different Ta concentrations to further affect grain refinement. As shown in **Figure 4.9**, multiple Al_3Ta particles are present in the centers of grains with large precipitates at grain boundaries, indicating that there is room for optimization. Samples of Al with 0.1wt% (0.02 vol%) to 5.8wt% (1 vol%) Ta were nanofunctionalized, additively manufactured and analyzed for grain size, final composition, and hardness. Hardness was expected to be dominated by the Hall-Petch relationship due to the relatively low solute content and associated minimal solute strengthening. In the higher volume contents some second phase particle strengthening may be possible, however given the low volume fraction of particulate this was also expected to be minimal[159,160]. Furthermore, the small Hall-Petch coefficient for aluminum (between 0.06 and 0.13 MPa-$m^{1/2}$)[56] should be sensitive only to large changes in grain size, as would be expected for the observed 1000X change in grain size between 0 vol% and 1 vol% (5.8 wt%) Ta. Final composition analysis indicated that the resulting materials were nearly identical to the target compositions, **Table 4.1**. It is possible that due to the small size of the particulate, gas flow or turbulence near the melt-pool may eject some of the nanoparticles from the system, however this is not the case and nearly all added nanoparticles appear to be incorporated in the resulting material, based on analysis using inductively coupled plasma optical emission spectrometry (ICP-OES), the results of which are indicated in **Table 4.1**.

Analysis of hardness and grain size presents an unexpected trend, **Figure 4.12**. The initial introduction of small amounts of tantalum show a sharp decrease in grain size from the baseline but then levels out until higher concentrations are reached. Low tantalum

content changes can likely be attributed to the aforementioned growth restriction factor, however when compared to the most common available equilibrium phase diagrams for the Al-Ta system (**Figure 4.13**), concentrations greater than 0.25 wt% (0.04 vol%) are above the peritectic point and would be expected to behave with at least a positive correlation where increasing particle density increases the nucleation rate and therefore reduces the grain size. Complicating this is the disagreement in the actual composition of the peritectic point ranging from about 0.25 wt% (0.04 at%) to 2.6 wt% (0.44 at%)[151]. The actual location of the peritectic could have a profound impact on the region of which the undercooled liquid resides in the phase diagram and the specific phases which are likely to nucleate.

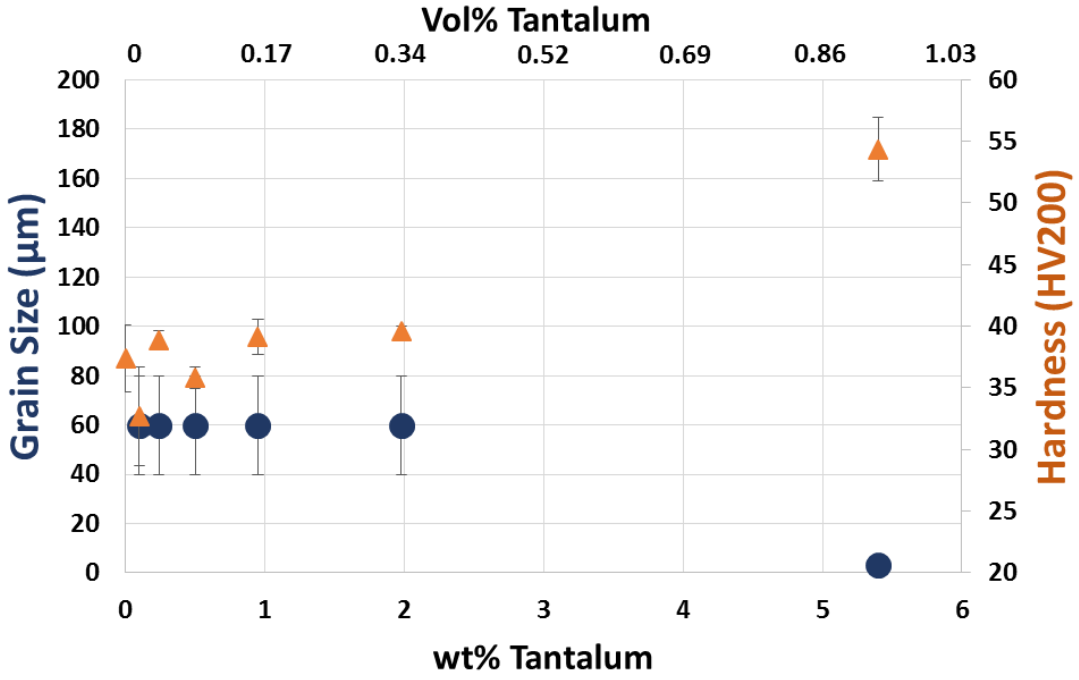

Figure 4.12: Grain Size and Hardness Relationship in Al-Ta samples. Hardness (orange triangles) and grain size (blue circles) indicating a relatively stagnant behavior in microstructure between 0.1 and 2 wt % Ta with a sharp increase in hardness and decrease in grain size at elevated Ta wt%.

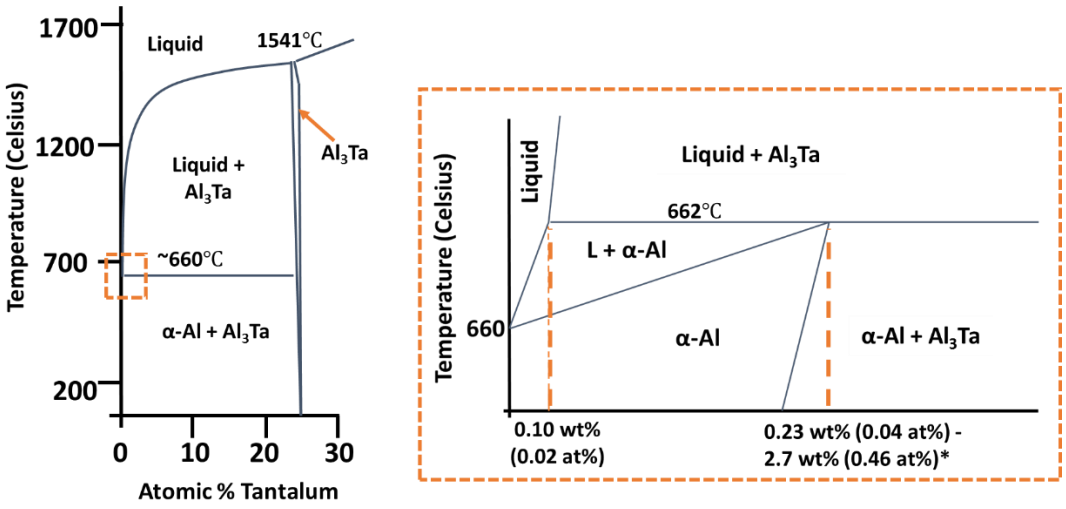

Figure 4.13: Aluminum Rich Aluminum Tantalum Phase Diagram. Variations in the potential peritectic composition are noted[151].

These observations prompted a reassessment of the Al-Ta phase diagram in the aluminum rich region, utilizing the 3D printed Al-Ta compositions. Samples with increasing tantalum content were held at 650°C ± 10°C for 96hrs. Samples were then scanned using X-ray diffraction (XRD) with a ~0.05° 2θ step size with a total scan time of 12hrs. The relatively slow scan rate was chosen to ensure identification of the Al_3Ta phase. As shown in **Figure 4.14**, Al_3Ta phases are clearly present in the 5.8wt% (1 vol%) sample. Indications of the presence of the phase are also observed down to about 1wt% (0.15 vol%), however, lower levels of Ta show no indication of Al_3Ta formation. Additionally there is a sharp change in peak intensity ratios indicating a change in texture. As discussed previously the Al_3Ta phase has high lattice registry to the (110) plane in Al. The presence of the Al_3Ta phase likely strengthens the texture of this orientation as shown by the high ~65° peak intensity at increased Ta concentrations. Strong texture in additively manufactured material is expected due to the high incidence of columnar growth previously described[100], however recrystallization was expected during heat treatment. The recrystallization texture of aluminum alloys has been shown to develop a strong (111) orientation. While the

mechanism of recrystallization is still debated, it is possibly related to the preferred <111> growth direction and low <111> twist boundary mobility seen in FCC metals (~40° peak)[161,162]. It is possible that the presence of the Tantalum changes the recrystallization behavior[163], as evidenced by the lowest volume percent (0.1 wt%, 0.02 vol%) showing a break in the trend towards the expected polycrystalline peak intensity ratios.

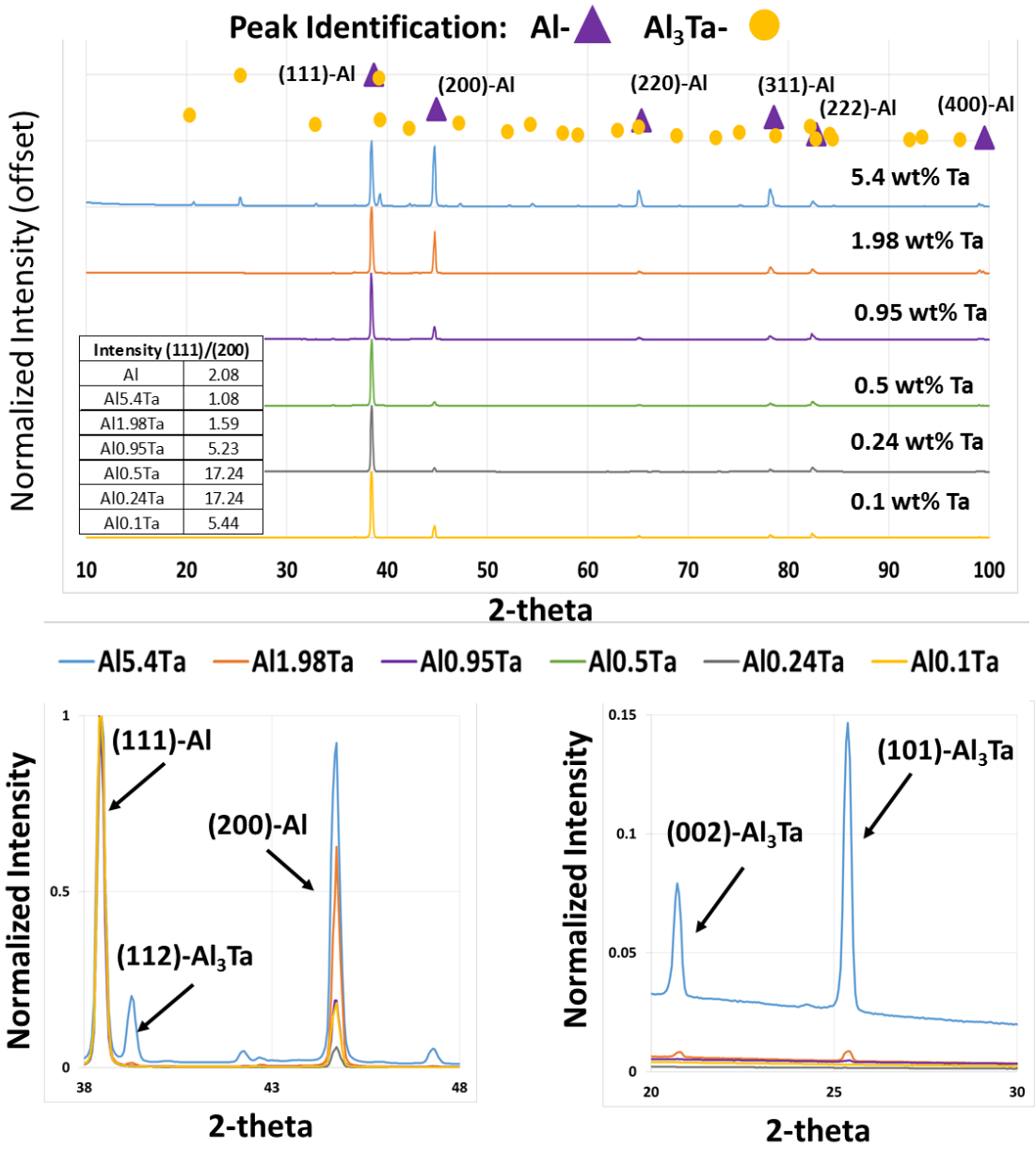

Figure 4.14: XRD scans of heat treated Al-Ta samples. (Top) Offset XRD patterns for tested materials indicating a general trend in peak intensity ratios with changing Ta content. Standard aluminum peaks are labeled and indicated with purple triangles, while standard Al_3Ta peaks are labeled with yellow circles. Peak identification was completed using standard peaks calculated in the materials project[164]. **(Bottom**) Zoomed in overlay plots of XRD patterns indicating **(Bottom-Left)** change in (111)/(200) peak intensity ratios and **(Bottom-Right)** disappearance in Al_3Ta phase peaks with decreasing Ta content**.** Compositions shown are based on ICP-OES of the as built samples.

While this is not fully conclusive, it does appear that the solubility of Ta in the FCC-Al lattice is likely higher than the proposed 0.25wt% (0.04 vol%)[165], but likely less than 2.6wt% (0.44 vol%)[150]. The original experiments indicating the 0.25wt% (0.04 vol%)

peritectic point only held at 640℃ for 50hrs[165], 52% of the hold time of this experiment, which may indicate a premature experimental data point where additional Ta solubility may exist. As such, additional hold times, as in this experiment, seem to indicate higher solubility. This experiment is also inconclusive as it relates to an equilibrium condition and not the solidification conditions indicative of additive manufacturing. As previously discussed, high curvature of the dendritic tip and increased solidification velocities can be present which could induce a metastable extension of the solid solution α–Al phase field. It is not unreasonable to predict that this could extend into the >2wt% (0.32 vol%) regime given the extremely low detection levels of Al_3Ta in 2wt% (0.32 vol%) vs 5.8wt% (1 vol%) Ta.

With an understanding of the region of the phase diagram for which the Al-Ta compositions are undergoing solidification, the nucleation events can be better described. Heterogeneous and homogenous nucleation rates, as described in Chapter 2, can be calculated given the following equation[51]:

$$I = v_0 p_c n \exp\left(\frac{-16\pi}{3}\frac{\gamma_{sl}^3}{\left(\rho \Delta s_f \Delta T\right)^2 k_B T} f(\theta)\right) \quad \text{(Eq 4.2)}$$

Where the $v_0 p_c$ term is related to the frequency of atomic attachment, n is the density of potential nucleation sites (where $n =$ density of atoms for homogenous nucleation in which every atom may act as a nucleation site), γ_{sl} is the solid liquid energy, ρ is the density, Δs_f is the entropy of fusion, ΔT is the magnitude of undercooling, $k_B T$ is the temperature dependent Maxwell-Boltzmann distribution indicating lower atomic mobility at decreased temperature, and $f(\theta)$ is a factor between 0 and 1 indicating the wettability of a heterogeneous nucleation site ($f(\theta) = 1$ in the case of homogenous nucleation). Given all

physical constants within the exponent are positive, increasing the value of the γ_{sl} and $f(\theta)$ decreases the nucleation rate, while in the case of favorable heterogeneous nucleation γ_{sl} and $f(\theta)$ are minimized to decrease the energetic barrier to nucleation leading to high nucleation rates.

Before incorporating the rate effects it is worth determining potential kinetic boundary conditions based on the potential input parameters. For this the Rosenthal solution was used to calculate isothermal profiles in the melt-pool at a variety of power, velocity, and preheat temperatures, **Figure 4.15**. The Rosenthal solution calculates a three-dimensional temperature field as,

$$T = T_0 + \frac{Q}{2\pi k r} exp\left[\frac{-V(r+\xi)C_p\rho}{2k}\right] \quad \text{(Eq 4.3)}$$

, where T_0 is the base temperature, Q is the heat input, k is the thermal conductivity of the material, V is the beam velocity, C_p is the material heat capacity, ρ is the material density and $r = \sqrt{\xi^2 + x^2 + y^2}$ with ξ as the moving reference axis in the direction of the beam travel. The Rosenthal solution is a highly simplified heat transfer solution for a moving heat source, and the solidus temperature isotherm (dashed line for aluminum in the figures) is not necessarily equal to the solidification front location or velocity. Since undercooling is required for nucleation and growth the solidification front can lag behind the solidus isotherm by several degrees. Additional heat of fusion and phase transformations are not directly accounted for making the isotherm locations approximate.

While more sophisticated models exist, the Rosenthal solution is a good approximation for evaluation of the thermal conditions within the right order of magnitude. By calculating the location of the 660℃ isotherm for different conditions, a bounding length of the meltpool can be approximated. This along with the given laser velocity then provides

approximate dwell times as a liquid assuming the meltpool has reached a steady state condition. For an arbitrary depth in the melt-pool the dwell time is calculated as, $\Delta L_{isotherm}/V_{beam}$, where $\Delta L_{isotherm}$ is the distance between two isotherms of interest perpendicular to the beam velocity vector. Given the boundary conditions of laser velocities between 0.5 and 3 m/s and powers between 100 and 500 Watts the approximate liquidus dwell time above the Liquid + Al_3Ta two phase region is between about 33 µs and 800 µs, with additional meltpool length as the preheat temperature increases from the simulated 100℃ resulting in increased dwell times.

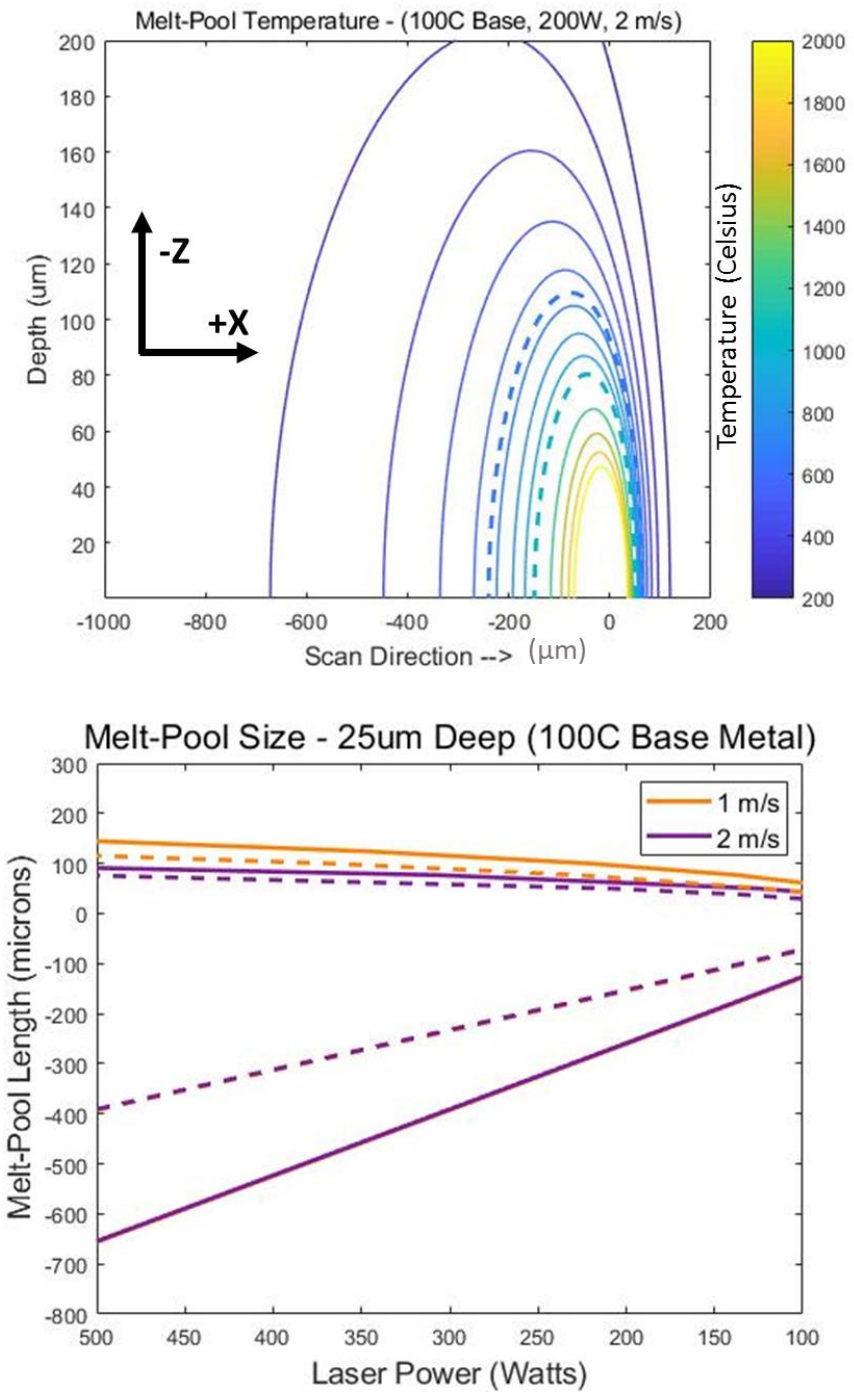

Figure 4.15: Melt-pool geometries based on Rosenthal Solution. (Top) Thermal contour map resulting from Rosenthal solution of pure aluminum with 200W heat source incidence at (0,0) and moving at 2 m/s for a 100°C base metal with the 660°C and 1000°C isotherms indicated by the dotted lines. Here the negative x values indicate the position behind the laser. **(Bottom)** A schematic indicating the 1000°C (dashed line) and 660°C (solid line) isotherms for two different laser scanning speeds at different laser power inputs. The plots are referenced based on a laser incidence at (0,0) with the positive being the isotherm location in front of the laser as in the Top plot, and negative numbers indicating the thermal field behind the laser. 25 μm deep was chosen as this was the layer thickness used in this study.

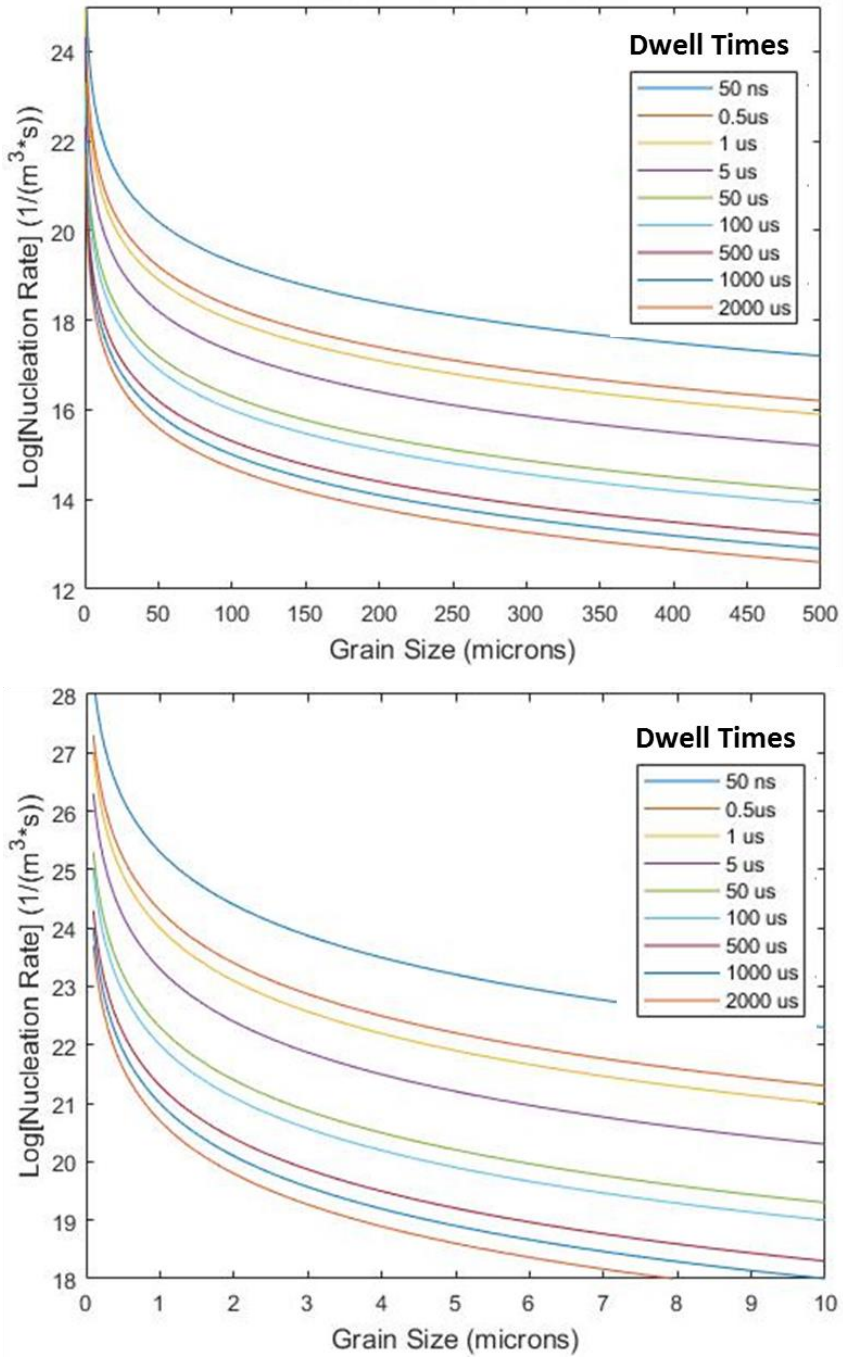

Figure 4.16: Nucleation rates vs Grain Size. (Top) Calculations of required nucleation rates to produce targeted grain sizes given a potential dwell time in the undercooled region from 50 ns to 2ms. **(Bottom)** Zoomed assessment for smaller grain sizes.

It is assumed that experimental nucleation site density in the Al-Ta samples can be predicted based on the grain density in the resulting material and a reasonable prediction of the dwell time in the undercooled region, **Figure 4.16**. As discussed in Chapter 3, the time

in the undercooled region can be estimated to be between 0.26 µs and 2.65 µs for 1℃ and 10℃ critical undercoolings for an estimated additive manufacturing condition with an absorbed laser power of 200W moving at 1 m/s and a base metal temperature of 150C calculated 25 µm below the melt-pool surface. The undercooled times along with the grain size of the resulting material can then be used to estimate the nucleation rates seen during processing where, $I = \rho_{grains}/t_{\Delta T}$. Here I is the approximate nucleation rate, ρ_{grains} is the number density of grains after solidification, and $t_{\Delta T}$ is the time spent in the undercooled region of the melt-pool. This dwell time will extend with increased build temperature due to a decrease in thermal gradient, but seems to indicate nucleation rates $>10^{21}$ $1/(m^3s)$ would be required to induce grain sizes less than 5 µm as seen in the additive 5.8wt% (1 vol%) Ta system.

This can then be compared to calculations given the nucleation rate equation, the number of particles can be approximated based on the wt% added and the size of the particulate. The range of particulate added, and by association the potential nucleation sites, varies only by a couple orders of magnitude across the compositions investigated (0.1 wt% (0.02 vol%)= $7.5*10^{17}$ particles/m^3 and 5.8wt% (1 vol%)= $4.4*10^{19}$ particles/m^3). If each particle can react and form at least a monolayer of the targeted Al_3Ta phase, this variation in particle loading has very limited impact on the number density of potential nucleation sites and therefore nucleation rates at low amounts of undercooling. As such, the grain sizes should be similar regardless of the loading, this is however not the case.

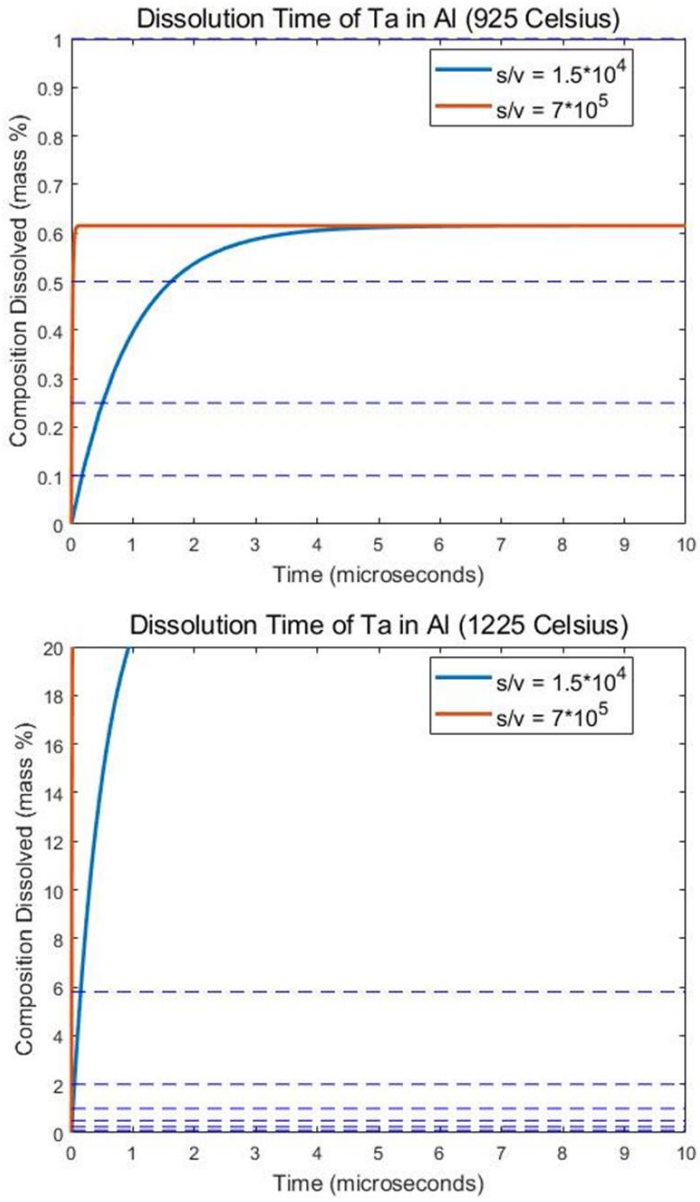

Figure 4.17: Dissolution Rates of Ta in Al. Dashed blue lines indicate compositions which were tested in this study. s/v ratios shown are indicative of the highest and lowest nanoparticle loadings tested in this study **(Top)** Dissolution rates at 925 C quickly approach the solubility limit in ~4 µs. **(Bottom)** If melt pool temperatures exceed 1225 C all Ta compositions tested in this study are likely dissolved in <1 µs. s/v ratios are in m^{-1}.

The lack of correlation between nanoparticle density and nucleation rate is likely an indication of particle dissolution rather than a solid state reaction occurs on the timescale relevant to the melt-pool solidification. Tantalum has a remarkably fast dissolution rate when compared to the growth rate of the intermetallic and typically does not form a thick layer of Al_3Ta until the liquid is fully saturated[166]. The temperature dependent

dissolution rate can be calculated from:

$$k = k_0 exp(-E_k/RT) \quad \text{(Eq 4.4)}$$

where k_0 = 1.48*10^3 m/s, E_k = 28 kJ/mol, and R is the gas constant. This can then be used to determine the dissolution time at constant temperature from equation:

$$C = C_s \left[1 - exp\left(\frac{-kst}{v}\right)\right] \quad \text{(Eq 4.5)}$$

where C is the composition dissolved in the liquid, C_s is the saturation composition at the specified temperature, s/v is the surface area to volume ratio, and t is the elapsed time[166]. Given the extremely high s/v introduced from the nanoparticle additions, in most cases the tantalum can be fully dissolved within about 3 μs, **Figure 4.17**. It should be noted that the dissolution time does not account for the Gibbs-Thompson effect present due to the small nanoparticle radius, likely driving faster dissolution rates than the equilibrium system calculated. Additionally the kinetic value of k was used in the calculation which is a smaller value than the k value accounting for diffusion which is a function of the Ta diffusivity in the liquid, melt viscosity, and angular velocity of the particles. Given the turbulent meltpool and superheating present from the laser it is possible that the liquid temperature reaches into the fully soluble region of the phase diagram leading to the rapid dissolution of the Ta particles and solidification of a saturated liquid as opposed to a liquid with secondary nucleation particles present.

Given the reasonably fast dissolution times possible at the approximated meltpool temperatures, the calculated liquid dwell times provide ample time for full dissolution to the liquid saturation limit given the high s/v ratio and the expected high meltpool temperatures and turbulence. It is therefore important to know the approximate dwell times in the two phase region of the phase diagram at Ta concentrations >0.1 wt%. Given the sharp increase

in liquidus temperatures the two phase region can be approximated to begin at about the 1000℃ isotherm, **Figure 4.15**. Variations in laser speed this gives an approximate dwell time in the Liquid + Al_3Ta region between 25μs and 125μs, providing ample time for growth or nucleation of a high number density of the Al_3Ta phase prior to entering the undercooled region where alpha-Al growth will occur.

The formation of Al_3Ta nucleation sites is therefore driven by two distinct mechanisms which may both be present in different areas of the melt-pool depending on the specific thermal conditions. At high Ta concentration and/or relatively low liquid temperature, the saturation of the liquid with dissolved Ta may result in the thermodynamically favorable formation of Al_3Ta which grows as solid state transformation from the originally introduced Ta particulate. At lower Ta concentrations and/or high liquid temperatures, where full dissolution is possible, the availability of Al_3Ta phases is then dictated by the nucleation rate of the Al_3Ta phase. The large amount of undercooling from the equilibrium Al_3Ta formation temperature (~1530℃)[151] provides a significant driving force for nucleation and growth of the targeted phase, regardless of surface energy (see nucleation rate equation) due to the large ΔT, large enthalpic driving force (-122 kJ/mol)[140], and high atomic mobility (related to $k_B T$ where T>660C). The nucleation rate is then dictated by the n term related to the density of potential Al and Ta clusters which can form the associated Al_3Ta phase. The relatively low atomic percentage of Ta in these experiments of between ~0.02 at% (0.1 wt%) and ~1 at% (5.8 wt%) leaves a statistical variation in potential nucleation sites of only a couple orders of magnitude. The convergence of the homogenous nucleation rate to the number density of potential sites and relatively low variation in number density between the tested samples indicates that there is likely little difference in the number

density of Al_3Ta nucleants regardless of composition with the assumption of full dissolution. The main difference would likely be related more to the size and growth velocity of the Al_3Ta phases with regard to composition which may nucleate from the Ta saturated melt.

The summation of experiments and calculations points to a clear mechanism of grain refinement in nanofunctionalized aluminum alloys utilizing the Al_3Ta peritectic system. A similar mechanism is expected for the other Al_3X peritectics (e.g. Nb and Zr). During laser melting the nanoparticles are incorporated into the liquid and quickly dissolve up to the added composition or saturation limit. In most cases the superheating in the melt pool is enough to fully dissolve the added particles, however this could likely be controlled with laser parameters and controlling the s/v particle ratio which dominates the dissolution rate. The resulting liquid then has three potential solidification pathways: heterogeneous nucleation on partially-dissolved particulate, epitaxial growth off previous additive layer, or a two-step nucleation mechanism. It is likely that a combination of all three events occurred to differing degrees during this experiment and within different locations in the melt-pool **(Figure 4.18)**. Due to different peak temperatures in the melt-pool and associated dwell times at temperature **(Figures 4.15, 4.16 & 4.17)**, the amount of dissolved Ta and rate at which nucleation can occur may evolve. It is possible that less dissolution occurs at the melt-pool boundaries due to lower temperatures and shorter dwell times could result in a greater number of residual particulates changing the nucleation dynamics. **Figure 4.18** shows systematic variations in microstructure, however it is difficult to draw significant conclusions as the degree of melt-overlap from the rastering and layer structure produce a complex thermal history. The formation of patches of ~30 μm columnar grains distributed though out the micrograph indicate there may be areas where formation of Al_3Ta is

unfavorable or fluid flow does not allow appropriate dwell time in the undercooled region to initiate growth. Based on an approximate dimensional analysis assuming liquid dwell times of ~30 μs and laser speeds of 1 m/s, these columnar grain sizes are consistent with the approximated thermal analysis utilized in this research. Additional thermal history studies are necessary to decipher the local nucleation behavior based on thermal history, however the potential mechanisms can be defined.

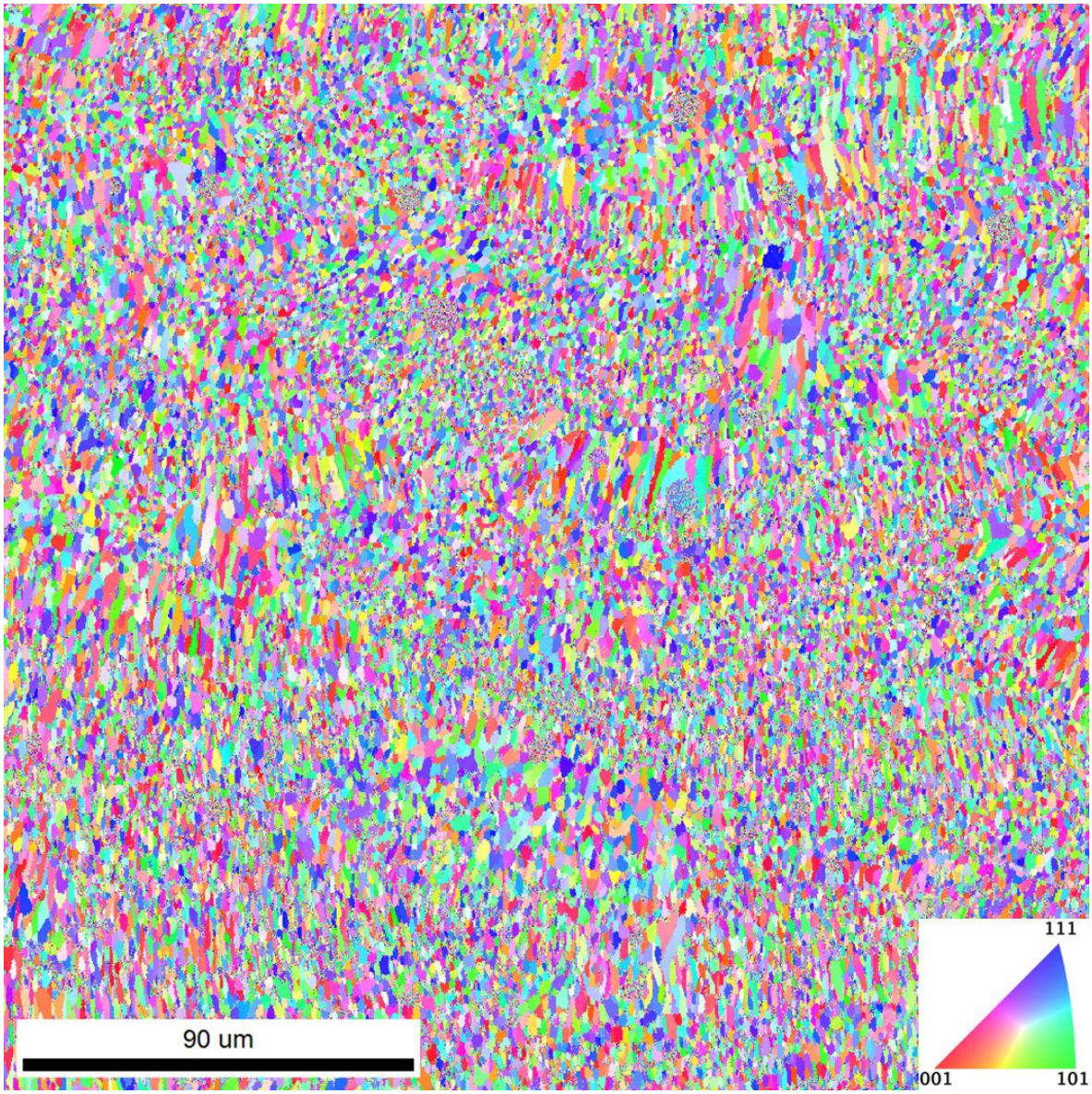

Figure 4.18: Large Area Inverse Pole Figure Map of Al-1at%Ta. Variations in microstructure are likely due to changes in dissolution and nucleation conditions. Build direction is oriented toward the top of the page. Reference orientation is into the page.

In the case for which the particles are not fully dissolved, a Al_3X surface layer may be present, promoting heterogeneous nucleation. Controlling the dissolution rates via parametric control and s/v ratios the exact number density of nucleants can be selected for optimum control of grain size and structure.

In the case of the lower Al-Ta concentration (0.1 wt%, 0.02 vol%) samples are quickly quenched through the liquid + α-Al phase region allowing for nucleation and growth on the previous melted layer, leading to a high degree of texture. This nucleation and growth is likely dominated by the GRF and evolution solute induced undercooled region. This indicates a dominance of the growth restriction rather than inclusion of secondary nucleants, however it is likely that some particulates may be present to promote nucleation. Additionally there could be some level of recrystallization during and after processing.

The case of full Ta dissolution is interesting as it is very similar to the two step nucleation phenomenon seen in the Al-Ti-TiB_2 system. At high super saturations the driving force for homogenous nucleation of the Al_3X phase reaches a peak (seen locally at the TiB_2 interface in the Al-Ti-TiB_2 system). Although calculations for the Al_3Ta nucleation event are not explicitly completed here, homogenous nucleation at extensive undercooling can exceed 10^{35} $m^{-3}s^{-1}$ well above the needed nucleation rates to produce the grain sizes seen indicating an extensive supply of secondary phases for nucleation at the more reasonable ~10^{20} $m^{-3}s^{-1}$ seen for the α-Al grains in the 5.8 wt% (1 vol%) Ta system. Homogeneous nucleation is highly unlikely in this event, however the calculated nucleation rates serve as a fundamental upper bound. In this case and that of the >0.25 wt% (0.04 vol%) samples, there is ample dwell time in the L+Al_3Ta region and α+Al_3Ta region to produce growth of the Al_3Ta intermetallic. Additionally solidifying past the peritectic point could decrease the

likelihood of a particle surface peritectic reaction which may lead to a high stress due to atomic rearrangement thus leading to a higher surface energy and lower driving force for nucleation. Solidifying past the peritectic point also avoids the two phase Liquid + α-Al region of the phase diagram. Based on the high dissolution rates of Ta into liquid aluminum it is likely that dissolution of Al_3Ta rather than nucleation of α-Al would be dominant decreasing the likelihood of potent Al_3Ta nucleation in the hypoperitectic composition regime.

To summarize, a thermodynamic and kinetic description of nucleation in additively manufactured nanofunctionalized materials has been presented. Leveraging nanofunctionalization and the unique solidification conditions of additive manufacturing, novel compositions can be produced leveraging the atypical nucleation phenomenon described herein. It is possible that this effect is exclusive to the additive manufacturing process where there is simultaneously high melt-pool temperatures providing a favorable condition for dissolution of large amounts of Al_3X peritectic elements, a long enough dwell time in the two phase Liquid + Al_3X region of the phase diagram to form thermodynamically stable nucleation sites, but short enough dwell times to avoid coarsening of said nucleation sites.

Given the mechanisms described, full microstructure control is possible with nanofunctionalization of aluminum alloys provided the parametric thermal inputs, composition of the alloy, and type of functionalizing agent can be described kinetically and thermodynamically with reasonable accuracy. While this mechanism has been thoroughly described for the pure aluminum system, additional alloying elements are likely to impact thermodynamics and kinetics, but should be easily accounted for given additive

manufacturing's general convergence to equilibrium phase diagram behavior. Furthermore, the applicability of the base physics may be extensible to other common alloys such as those of iron, nickel, and titanium.

Chapter 5

Additive Manufacturing of Crack Susceptible Aluminum Alloys

Metal additive manufacturing, as previously described, is a potentially disruptive technology across multiple industries, including aerospace, biomedical and automotive[2,3]. Building up metal components layer by layer increases design freedom and manufacturing flexibility, thereby enabling complex geometries, increased product customization and shorter time to market, while eliminating traditional economy-of-scale constraints[4]. This dissertation has focused mainly on the principles of grain refinement in additive manufacturing and the ability to utilize nanofunctionalization to control nucleation in pure aluminum systems. This chapter will focus on how applying the principles of nanofunctionalization and grain refinement to crack susceptible, high strength aluminum alloys can aid in accommodating strain accumulation during solidification and eliminate cracking[167]. Industrial use of pure aluminum systems for structural applications is rare and the use of alloyed aluminum alloys such as Al6061 and Al7075 are much more common[40,168]. Unfortunately the large solidification ranges of these alloys make them susceptible to cracking during solidification and unusable in typical additive manufacturing processes[52,169]. This data presented in this chapter was previously published by Martin et al.[167,170]

Currently only a handful of alloys, the most relevant being AlSi10Mg, TiAl6V4, CoCr, and Inconel 718, can be reliably printed.[2,3] The vast majority of the >5,500 alloys

in use today cannot be additively manufactured because the unique melting and solidification dynamics during the additive process lead to intolerable microstructures with large columnar grains and periodic cracks.[24,37,171] These issues can be solved by introducing nanoparticle nucleants that control the solidification during additive manufacturing[167]. Nucleants were selected using crystallographic informatics and assembled onto aluminum alloy Al7075 and Al6061 powders. After functionalization with targeted nucleants, it was found that these high strength aluminum alloys, previously incompatible with additive manufacturing, can be successfully processed by selective laser melting. Crack-free, equiaxed, fine-grained microstructures were achieved, resulting in strengths comparable to wrought material. This approach is both alloy and machine agnostic, providing a foundation for broad industrial applicability including electron beam melting (EBM) and directed energy deposition techniques such as Laser Engineered Net Shaping (LENS) and wire fed systems . It is possible that it can enable additive manufacturing of other alloy systems such as nonweldable nickel superalloys and intermetallics. Furthermore this technology can also be leveraged in conventional processing routes such as joining, casting, and injection molding, where solidification cracking and hot tearing are also common issues.

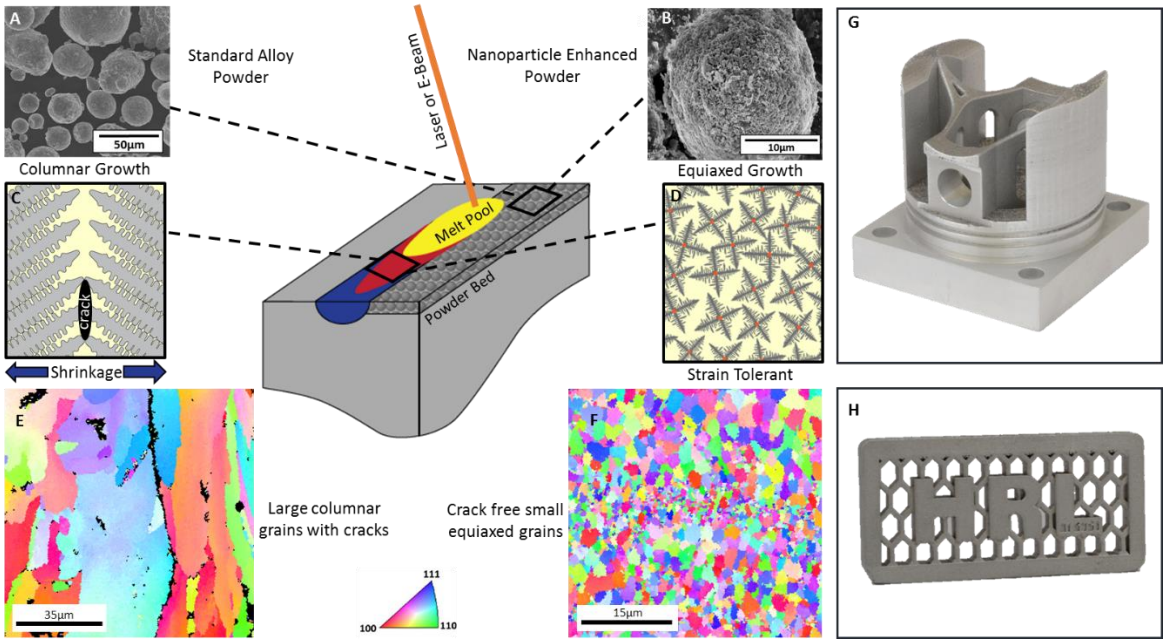

Figure 5.1: Additive manufacturing of metal alloys via selective laser melting. a, Conventional Al7075 powder feedstock. **b,** Al7075 powder functionalized with nanoparticles. **c,** Many alloys including Al7075 tend to solidify by columnar growth of dendrites resulting in cracks due to solidification shrinkage. **d,** Suitable nanoparticles can induce heterogeneous nucleation and facilitate equiaxed grain growth, thereby reducing the impact of solidification strain. **e,** Many alloys exhibit intolerable microstructure with large grains and periodic cracks when 3D printed with conventional approaches. **f,** Functionalizing the powder feedstock with nanoparticles produces fine equiaxed grain growth and eliminates hot-cracking. **g,** 3D printed topologically optimized Al6061 piston on the build plate. **h,** 3D Printed Al7075 HRL Logo

5.1 Evolution of Crack Susceptibility in Alloys

In metal additive manufacturing, application of a direct energy source, such as a laser or electron beam, to melt alloy powders locally results in solidification rates between 0.1 and 5 m/s, an order of magnitude increase over conventional casting processes. Given that rastering of this direct energy source to continuously fuse successive layers of powder is analogous to welding processes, it is not surprising that the suite of printable metal alloys are limited to those known to be easily weldable. Application of conventional 3D printing methods to “unweldable” high performance engineering alloys that cannot accommodate these solidification conditions, such as 6000 and 7000 series aluminum alloys and high gamma-prime nickel superalloys, results in microstructures with columnar grains and cracks

spanning dozens of successive print layers[24,37,171]. The limitations of the currently printable alloys, especially with respect to specific strength, fatigue life and fracture toughness, have hindered metal additive manufacturing from maturing to its full potential.

During solidification of these unweldable alloys, the primary equilibrium phase solidifies first at a different composition than the bulk liquid. This results in solute enrichment in the liquid near the solidifying interface, locally changing the equilibrium liquidus temperature and producing an unstable, undercooled condition[50]. As a result, there is a breakdown of the solid liquid interface leading to cellular or dendritic grain growth with long channels of interdendritic liquid trapped between solidified regions. As temperature and liquid volume fraction decrease, volumetric solidification shrinkage and thermal contraction in these channels produces cavities and hot tearing cracks which may span the entire length of the columnar grain and can propagate through additional intergranular regions[172,173] (**Figure 5.1e**).

In contrast, fine equiaxed microstructures more easily accommodate strain in the semi-solid state by suppressing coherency that locks the orientation of these solid dendrites and promotes tearing[174]. Producing these ideal equiaxed structures requires high amounts of undercooling which has thus far proven difficult in additive processes where high thermal gradients arise from rastering of a direct energy source in an arbitrary geometric pattern[108]. As previously described, a general approach to control solidification microstructure by promoting nucleation of new grains with nanoparticle grain refiners (**Figure 5.1d**). Alloy powder feedstock particles are decorated with lattice-matched nanoparticles (**Figure** 5.**1b**) that heterogeneously nucleate the primary equilibrium phases during cooling of the melt pool. By providing a high density of low energy barrier

heterogeneous nucleation sites ahead of the solidification front, the critical amount of undercooling needed to induce equiaxed growth is decreased[95]. This allows for a fine equiaxed grain structure that accommodates strain and prevent cracking under otherwise identical solidification conditions. Utilizing this technology enables additive manufacturing of previously unattainable high performance alloys, such as 7075 or 6061 aluminum, with improved properties over currently available systems.

Aluminum alloys are a good demonstration platform for our approach, since the only printable aluminum alloys are based on the binary Al-Si system and have a wide range of reported properties, but tend to converge around yield strength of approximately 200 MPa with low ductility of 4%[2,62]. The exception is Scalmalloy[23,175], which relies on alloying additions of Scandium, a rare high cost metal. In contrast, most aluminum alloys used in automotive, aerospace and consumer applications are wrought alloys of the 2000, 5000, 6000 or 7000 series which can exhibit strengths exceeding 400MPa and ductility of >10% but cannot currently be additively manufactured[168,176,177]. These systems have low cost alloying elements (Cu, Mg, Zn, Si) carefully selected to produce complex strengthening phases during subsequent aging. These same elements promote large solidification ranges, leading to hot tearing during solidification, an issue that has been difficult to surmount for over 100 years since the first age-hardenable alloy, Duralumin, was developed in 1909[26,178]. The most complete study of elemental effects dates back to the late 1940s, however the mechanistic effect was not fully described until 1999 by Rappaz, Drezet, & Gremaud (RDG)[27,173]. The RDG model uniquely incorporated both deformation of the semi-solid network and fluid backfill to capture the composition and microstructure effects on cavitation assisted tearing. Additionally, Gourlay & Dahle

demonstrated experimentally that strain can be accommodated more readily in a fine equiaxed material due to an increase in the solid fraction at which dendrite coherency occurs and the suppression of large dilatant shear bands which require additional backfilling[179]. Combining the mechanistic effects addressed by Gourlay & Dahle and the predictions of the RDG model to minimize crack susceptibility has not been effective for highly crack susceptible alloys such as Al-7075 and Al-6061, due to a lack of processing paths to produce fine equiaxed grains.

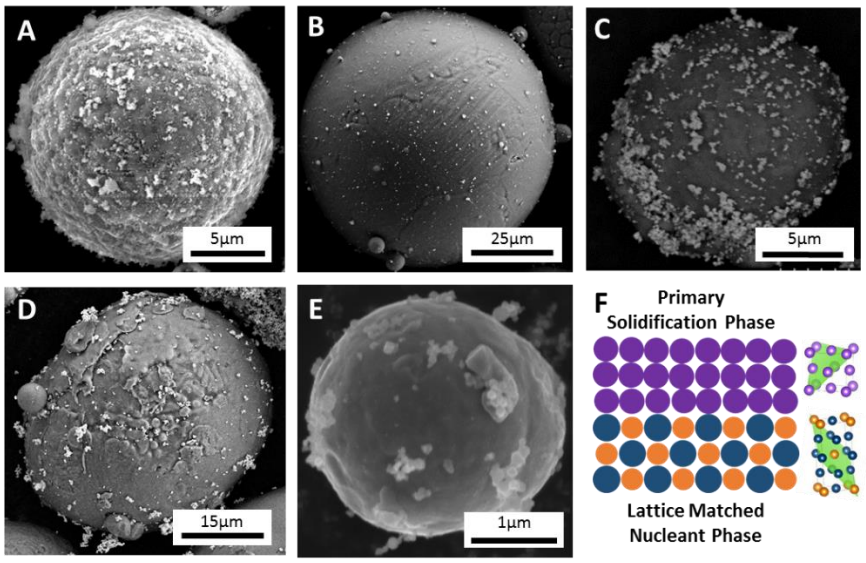

Figure 5.2: Nanoparticle assembly on additive metal feedstock. The alloy and nanoparticle agnostic assembly approach enables the production of a variety of feedstocks with different nanoparticle assemblies which can be targeted to induce equiaxed grain growth **a,** Al7075 powder with TiB_2 Nanoparticles (NPs). **b,** TiAl6V4 powder with ZrH_2 NPs. **c,** Al7075 powder with WC NPs. **d,** AlSi10Mg powder with WC NPs. **e,** Iron powder with TiC NPs. **f,** Graphical representation of how lattice matched nanoparticles (bottom phase in blue and yellow) can induce low energy barrier epitaxial growth of solidifying metals (top phase in purple).

A scalable and alloy-agnostic approach has been developed to directly incorporate grain refining particles into conventional hot tear susceptible alloy powders to additively manufacture high strength crack-free alloys with a fine equiaxed microstructure (**Figure 5.2**). Conventional alloy powders and nanoparticles are electrostatically assembled, producing a powder feedstock with uniformly distributed nanoparticles. Nanoparticle

compositions targeted to each alloy were selected using a new software tool that identified matching crystallographic lattice spacing and density to provide a low energy nucleation barrier based on classical nucleation theory (**Figure 5.2f**). The software described in Chapter 3 analyzed over 4,500 different powder and nanoparticle combinations corresponding to over 11.5 million matching pairs. Potential matches were sorted by a combined set of constraints: minimized lattice misfit, similar atomic packing along marched crystallographic planes, thermodynamic stability in the desired alloy, and availability. For the aluminum alloys tested, hydrogen stabilized zirconium particles were selected for their stability in air and ability to decompose at the melting temperature, resulting in formation of the favorable Al_3Zr nucleant phase[130]. This phase has previously been described as a "mild" grain refiner in the literature but can be difficult to incorporate in many aluminum alloys due to rapid coarsening and a high liquidus temperature, making gas atomization of additive feedstock difficult[115,130]. In the present approach incorporation of this particulate at the instant of melting provides a high level of mixing and a high density of nucleation sites.

5.2 Additive Manufacturing of Nanofunctionalized Crack Susceptible Alloys

Pre-alloyed gas atomized 7075 and 6061 spherical powders with an average particle size of 45 μm were coated with 1 vol% hydrogen stabilized zirconium nucleants using an electrostatic assembly technique to ensure uniform distribution in the powder bed and avoid settling. Assembled powders were additively manufactured via selective laser melting using a Concept Laser M2 400W system with an 80mm x 80mm build volume. Standard machine parameters provided by the manufacturer for a conventional AlSi10Mg alloy were utilized for all nanoparticle functionalized 7075 and 6061 powders. After completion of the build,

components were homogenized on the build plate and aged to a T6 condition in accordance with conventional wrought materials. For direct property comparison, parts were also manufactured from stock 7075, 6061, and AlSi10Mg powders without functionalization under the same processing conditions.

The Concept Laser M2 machine specifications are listed in **Table 3.3**. Samples consisted of 60mm x 20mm x 40mm tensile block specimens and 10mm x 10mm x 40mm blocks for examining microstructure. Images of the as-printed samples on the build plates are shown in **Figure 5.3**. Samples were processed with Concept Laser "islanding" scan strategy specifically developed for the CL31 AlSi10Mg alloy material to minimize thermal and residual stress build up in the part. Islands which compose the core of the build geometry were 2mm x 2mm in size. The standard parameter values are considered proprietary by Concept Laser and cannot be accessed by the user. The 70mm x 70mm build plates were machined out of aluminum alloy 6061 and sandblasted on the surface. Layers of the build were incremented by a range from 25μm to 80μm depending on part geometry and location in the build. Processing was done under a flowing, inert argon atmosphere with oxygen monitoring. All processing was completed at room temperature with no applied heat to the build plate. Samples were removed from the machine and cleaned of extra powder by sonicating in water. Parts were then dried with clean compressed dry air.

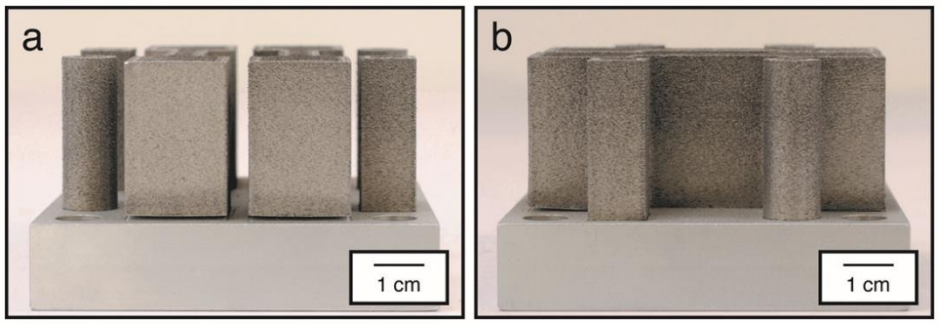

Figure 5.3: As-printed Al 7075 parts for tensile testing and microstructure evaluation. (a) Stock Al 7075, (b) Al 7075 + Zr.

Microstructure analysis reveals a substantial difference between components additively manufactured from stock powders and those produced with nanofunctionalized powder (**Figures 5.1 & 5.4**). Stock 7075 and 6061 exhibit a series of large columnar grains oriented parallel to the build direction with cracks present in the intercolumnar region and extending through multiple build layers. This is consistent with previously documented attempts at printing wrought aluminum alloys and is driven by the high, directional heat flux in an additive process which provides high thermal gradients and minimal undercooling during solidification[24]. Previous additive routes to producing equiaxed grains have focused on manipulating the thermal gradient and solidification velocity to induce substantial undercooling for nucleation of equiaxed microstructures, as described in Chapter 2. Manipulating the thermal gradients and solidification velocity to produce equiaxed grain structures requires extensive manipulation of parameters including scan strategy and build temperature and is not extensible to multiple alloy systems, additive hardware or build geometries[58,108]. While the solidification velocity is relatively high, it is not sufficient alone to induce equiaxed growth per the conventional Hunt criterion for a columnar to equiaxed transition. In particular, the high thermal conductivity of aluminum and large

liquid diffusivities of alloying elements make significant undercooling extremely difficult to achieve with the accessible ranges of solidification velocities and thermal gradients[180]. In addition, the Hunt criterion assumes a steady state solidification front, while the additive process deviates significantly from steady state due to the raster pattern and accumulation of residual heat[69]. As such, solidification preferentially occurs through nucleation on existing grains from the previous layer, leading to the observed grain growth oriented preferentially along the build direction with grains extending across multiple build layers as in the inverse pole figure map in **figure 5.1e**.

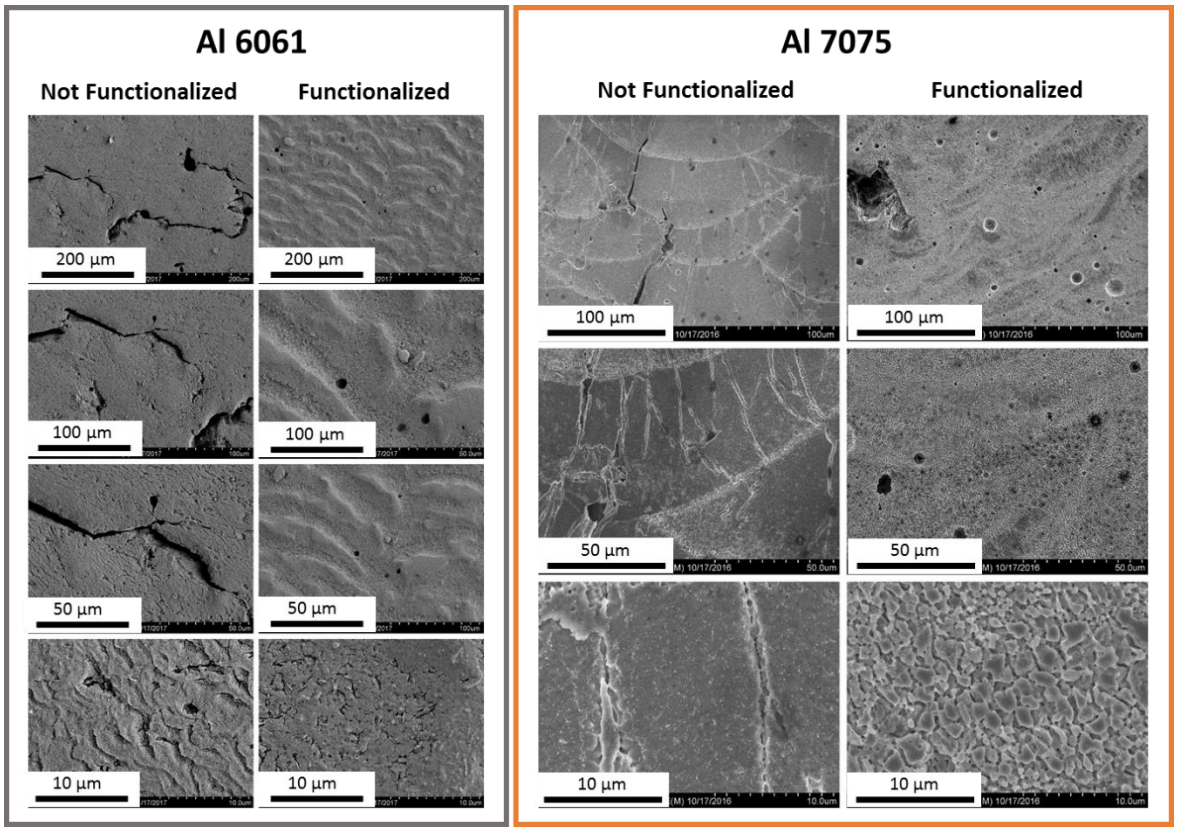

Figure 5.4: Scanning electron microscopy images of etched microstructures. Etched Al 6061 (**Grey Box**) processed as built indicating large cracking (**Left**) and with the addition of nanoparticle Zr showing no observable cracking, but some residual porosity (**Right**). Al 7075 (**Orange Box**) processed as built indicating large networks of cracks (**Left**) and with the addition of nanoparticle Zr showing no cracking but some residual porosity (**Right**).

In contrast, the 7075 and 6061 alloys manufactured with grain refining nanoparticles show no cracking. Upon melting, zirconium particulates are pulled into the melt pool and react to form Al_3Zr. The 1 vol% (>2wt%) zirconium added is above the 0.28 wt% peritectic point shown in **Figure 4.3** in order to induce a similar reaction and inoculation behavior to the Al-Ta system described in Chapter 4. Al_3Zr has over 20 matching interfaces in the [100] family of planes with the primary FCC aluminum phase exhibiting less than 0.52% lattice mismatch and 1% variation in atomic density, providing an ideal low energy heterogeneous nucleation site. Nucleation of new grains ahead of the solidification front requires both an energetically favorable condition and a high number of nucleation sites to ensure new grains can form prior to the main solidification front overtaking new grains. The columnar growth demonstrated in the unmodified material indicates that undercooling is present providing an energetically favorable condition for a nucleation event to occur; however without additional nucleation sites, homogenous nucleation is required at a substantially higher energy barrier. The high number of low energy barrier heterogeneous nucleation sites ahead of the solidification front induce a fine equiaxed structure under the same processing conditions as the unmodified powder. This results in crack-free microstructure with grain sizes on the order of 5 μm, 100 times smaller than the grains in the unmodified material **(Figure 5.1e,f)**. The nucleant particles are uniformly incorporated into the microstructure which can provide additional strengthening and resistance to grain growth due to pinning effects.

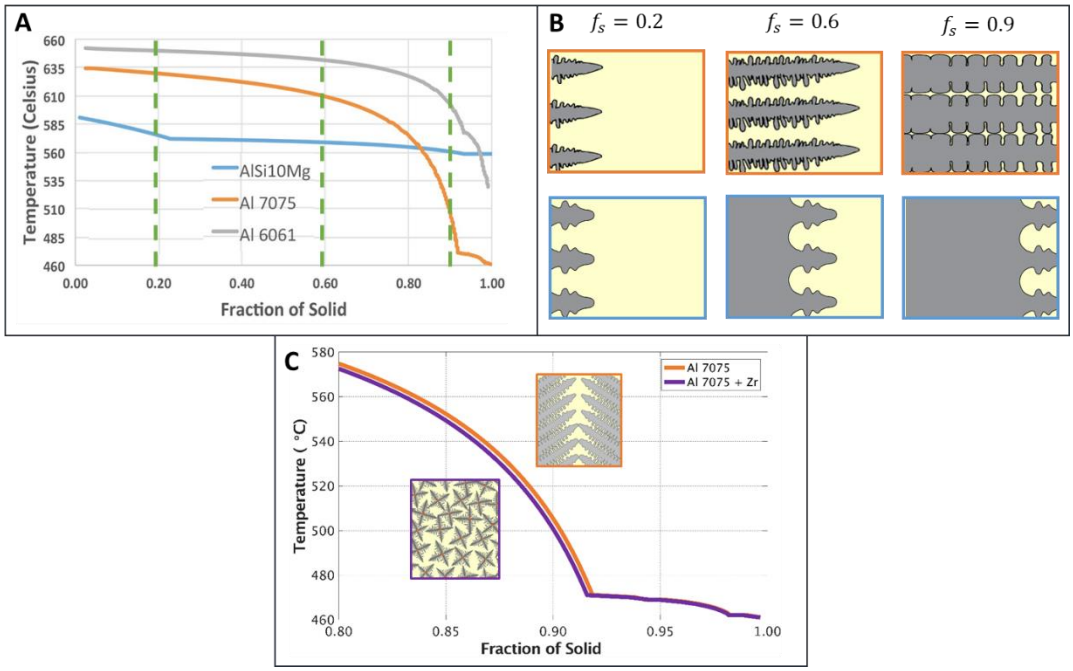

Figure 5.5: Solidification behavior of additive aluminum alloys. a, Scheil solidification curves for Al7075, Al6061, and conventional 3D printed aluminum, AlSi10Mg. **b,** Graphical representation of solidification indicating how the large solidification temperature range leads to long channels of interdendritic fluid which result in cracking (top), while a small solidification range leads to short interdendritic regions which can easily be backfilled (bottom). **c,** Adding zirconium to Al7075 has little impact on the solidification behavior at high solid fractions where alloys are the most tear and crack susceptible.

Observed cracking in the stock material appears consistent with the described mechanisms of the RDG model[173]. Columnar grains grow in the direction of the heat flux leaving a thin layer of interdendritic fluid leading to cavity formation (**Figure 5.5b**). Further thermal shrinkage allows this initial cavity to "unzip" and propagate through interdendritic colonies resulting in large cracks oriented parallel to the columnar grains[173]. The simplest form of the model utilizes a growing columnar front (**Figure 5.5b**) and calculates the pressure change in the interdendritic liquid dictated by the deformation of the solid and the ability of the liquid to backfill into the interdendritic channels. The amount and rate of solid deformation is dominated by the material dependent shrinkage factor (6% for aluminum) and solidification velocity, while the ability to back fill is related to the viscosity of the liquid and secondary dendrite arm spacing which is used in a Carmen-Kozeny

approximation to calculate pressure drop of the fluid during backfilling[173]. A higher pressure change indicates a higher tendency for cracking as the chance of void cavitation and growth is higher.

While the RDG model does not explicitly describe the effects of equiaxed microstructure on crack susceptibility, the shift to equiaxed growth drastically reduces the impact of entrapped liquid as the grains begin to behave as a low resistance granular solid[179]. Fine equiaxed semi-solid structures allow easier grain rotation and deformation, providing a means to accommodate strain in the semisolid state, thus preventing crack initiation and growth. The observed complete elimination of cracks is attributed to the change in microstructure. Hot-tearing models, including the RDG model, are dominated by the final stage of solidification when the fraction of solid is greater than 0.8[181]. Many tear resistant materials can be identified through observation of their solidification curves (**Figure 5.5a**). The shapes of these curves are dictated by the compositions of the constituent alloys and can be described using a Scheil-Gulliver solidification model based on the equilibrium phase diagram[182]. Thermo-Calc software was used to simulate sequential steps from the liquidus temperature to an approximate solidus temperature calculating the fraction of solid and composition of the new liquid at each point. Susceptible alloys have large solidification ranges between the liquidus and solidus temperatures and sharp turnover in the solidification curves at high fractions of solid. The sharp turnover is typically associated with the high levels of strengthening solute that strongly partitions between the solid and liquid during solidification. Associated thermal shrinkage leads to tearing and cavitation in thin films of interdendritic liquid present at the high solid fraction. Decreasing the solid fraction at which the turnover occurs or reducing the difference

between the solidus and liquidus temperatures will improve resistance to tearing[52]. A conventional additive aluminum alloy such as AlSi10Mg has both an early turnover and small difference in liquidus and solidus temperature leading to a low tendency for cracking during solidification. This stands in stark contrast to 7075 and 6061.

The shape of these curves can be shifted with increasing solidification velocity due to the non-equilibrium partition coefficients, however this work showed no evidence of significant departure from equilibrium[76]. The addition of zirconium might be expected to shift the solidification into a more favorable shape (e.g. shorter solidification range or lower slope in the high volume fraction of solid), however as shown in **Figure 5.5c** this is not the case. As described in Chapter 4, the Al-Zr binary phase diagram indicates a peritectic reaction at high mass fractions of aluminum[130]. As such, any Al-Zr reactions occur at the beginning of solidification where tear resistance is not critical due to the low volume fraction of solid. More importantly the addition of zirconium does not significantly alter the shape of the solidification curve at high fractions of solid, where hot tearing is initiated. As discussed above, the early inclusion of zirconium induces equiaxed growth which can more easily accommodate the thermal contractions strains associated with solidification, ultimately resulting in an alloy system that is highly tear resistant, despite conventional wisdom.

5.3 Mechanical Properties of Additive Al7075

Prior to mechanical testing, samples were heat treated to a T6 condition. This consisted of solutionizing at 480^{o}C in air with a ramp rate of 5^{o}C/minute for 2 hours and then quenching with water at 25^{o}C. Subsequently, an aging study was completed were aged at 120^{o}C with a ramp rate of 4^{o}C/minute in air for 6, 12, 18, and 24 hours at 120^{o}C. Vickers

hardness measurements were used to determine a range of appropriate aging time around 18 hours, results are summarized in **Figure 5.6**.

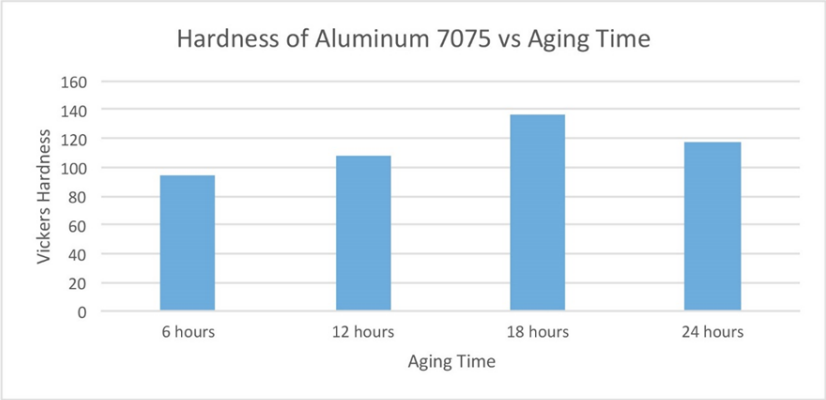

Figure 5.6: Aging Behavior of Additive Al7075. Tests conducted using 200g load on a Vickers microhardness tester. Data shown is an average of five samples taken at the stated aging time after a homogenization treatment and water quench.

Based on these results it was determined that 18 hours provided an approximate T6 peak aged condition and all tensile samples were heat treated to this condition. These times and temperatures were chosen based on typical heat treatment conditions for wrought Al7075 plate material[40]. Because the starting microstructure from the additive process is different than that of the wrought plate, additional study is likely needed in determining the appropriate heat treatment methods for additively manufactured high strength aluminum alloys beyond what was completed here.

Tensile tests were performed on a servo-electric INSTRON 5960 frame equipped with a 50kN load cell. Samples were clamped by the ends of the dog-bone samples. Dog bones had an approximate gauge cross section of 2mm x 7.5mm and a gauge length of 20mm. As built material from which the dog bones where excised via EDM are shown in **Figure 5.3**. The extension rate was 0.2mm/min and samples were loaded until fracture.

Testing was conducted following ASTM E8 specifications. A U-joint was used to account for any misalignment in the sample.

As cracks tended to orient parallel to the build direction all tensile testing was conducted perpendicular to the expected crack orientation. This ensured that any residual cracks would have the maximum impact on the tensile properties. The measured ductility in the nanofunctionalized material, ranging from 3% to 17%, indicates an elimination of deleterious cracking.

Table 5.1: Material Properties of Tested Materials and Comparable Wrought Literature Values.

Material	Yield Strength (MPa)	Ultimate Strength (MPa)	Elastic Modulus (GPa)	Elongation (%)
AM Al 7075 - T6[167]	N/A	25.5	N/A	0.4
AM AlSi10Mg[183]	209	315	69.4	7.3
AM Al 7075 + Zr - T6[167]	325 – 373	383 – 417	63 – 66	3.8 – 5.4
AM Al 7075 + Zr HIP T6[170]	325 – 375	450 – 475	69 – 70	15 – 17
AM Al 7075 + Zr Low LED T6[170]	410 – 425	450 – 475	69 – 70	3 – 5
Wrought Al 7075 - T6 [Plate][19]	372 – 469	462 - 538	71.7	3 – 9

Tensile results were compared against equivalent specimens produced from unmodified powder to verify the crack free nature of the additively manufactured material. **Figure 5.8** displays typical stress strain curves for each material and associated yield strength, modulus, ultimate tensile strength and elongation to failure are summarized in **Table 5.1**. As shown, conventional 7075 retains almost no strength due to the large volume of cracks caused by hot tearing. Conventional AlSi10Mg shows about 7% ductility but less

than half the strength of the wrought 7075 system consistent with data provided by multiple selective laser melting companies. In comparison, additively manufactured 7075 with the incorporation of Al_3Zr nucleant particles shows an 80% increase in strength over AlSi10Mg, and is within the expected bounds for its wrought counterpart. The modified Al7075 exhibits Luders banding during deformation, which is indicative of an aluminum alloy with grain sizes below 10 µm (**Figure 5.8**)[184]. The yield strength and elongation of functionalized Al7075 was produced within reported ranges of wrought Al7075 (**Table 5.1),** however the ultimate strength difference and lower limit of yield strength can be explained by strain softening from the reduced grain size and zinc and magnesium, both major strengthening elements, evaporation during the laser melting process. Composition changes from the powder to the printed parts are shown in **Figure 5.7**.

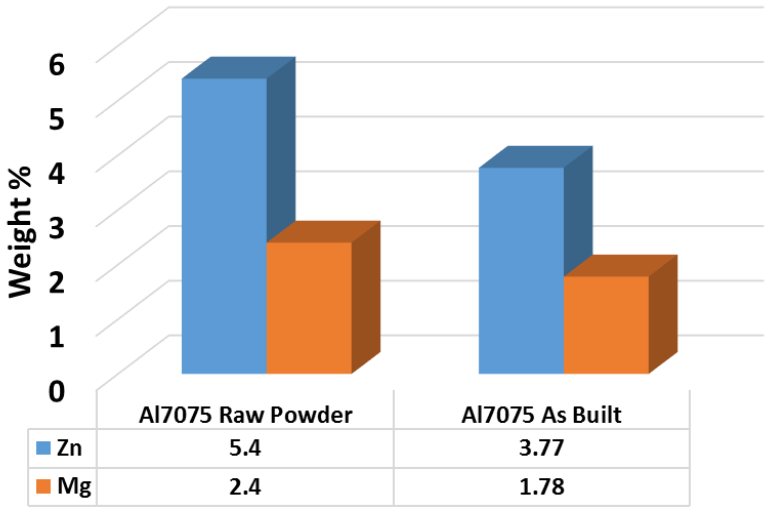

Figure 5.7: Composition change of as received and as processed material. Zinc and Magnesium are highlighted as the only elements with noticeable change in composition from the initial composition measured by ICP-OES.

Differences in composition between additively manufactured Al7075 and conventional wrought material can be remedied by increasing the zinc concentration in the feedstock powder to improve strength and optimizing the heat treatment to target an

optimum final grain size to eliminate strain softening. Likewise, ductility and elastic modulus can be increased by improving processing parameters to reduce porosity caused by excessive laser energy density and trapped gas, a feature that was not fully optimized in this study. Additively manufactured metal parts are often hot isostatic pressed (HIP) to reduce porosity and improve properties. This process involves subjecting the parts to high pressure (>10ksi) at temperatures near the solidus point (~480℃ for Al7075) at which point the applied isostatic pressure exceeds the yield point of the material and deforms to close up the internal porosity. Additionally manipulating the parameters and lowering the laser energy density (LED) could decrease the evaporation rates of Zn and Mg in the alloy. Decreasing the applied volumetric LED can decrease the temperature of the melt pool, potentially decreasing the vaporization of the volatile Mg and Zn alloying elements. The effects of HIPing and decreasing the energy density by 10% were tested independently and the results are shown in **Figure 5.8**. As with the standard build parameters, exact values for thebuild parameters (e.g. power, hatch spacing, etc.) were not explicitly known and the value for the applied power was adjusted by 10%.

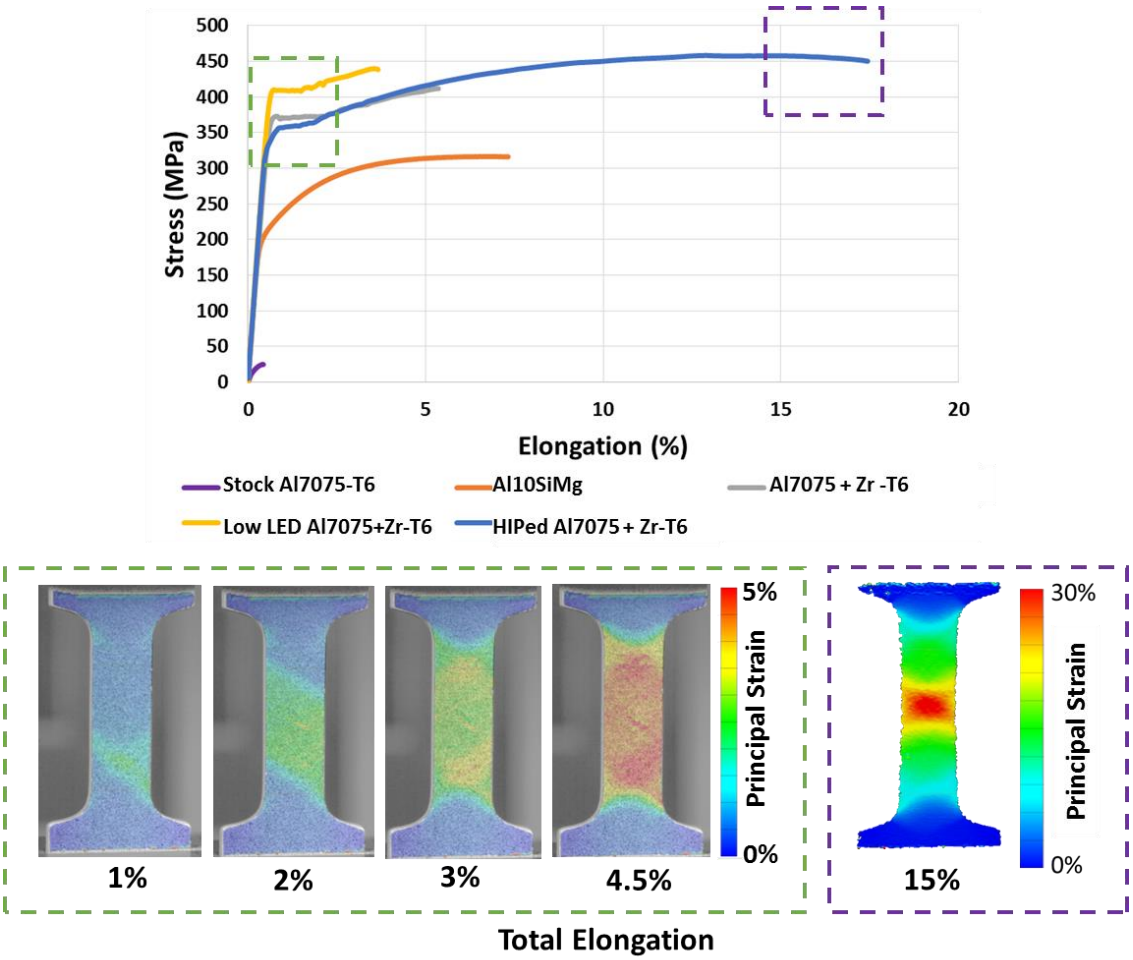

Figure 5.8: Tensile behavior of additive aluminum. (Top) Typical stress strain curves for tested materials. **(Bottom)** Principal strain maps at highlighted regions of the tensile curves. **(Bottom-Left)** Representative deformation behavior of Al7075+Zr indicating Luders band propagation indicative of the refined grain size. **(Bottom-Right)** HIP treatment reduces porosity and results in a 3X increase in elongation to failure and high local accumulations of strain exceeding 30%.

Decreasing the laser energy density by 10% resulted in a >75% retention of the strengthening elements and a 10% increase in yield and ultimate tensile strength over the nanofunctionalized Al7075 with the Al10SiMg parameters. While retaining additional alloying elements may lead to higher crack susceptibility in conventional processing, the nanofunctionalized material still completely eliminates the hot cracking tendency. Additionally, utilizing nanofunctionalized Al7075 processed with AlSi10Mg parameters and applying an industry standard HIP treatment, elongation increased by 3X and the elastic

modulus increased by 5%, both indicating an elimination of residual porosity which promotes early fracture and decreases the effective cross-section area during tensile testing. The combined effect of these results indicates crack free high strength aluminum alloys can be processed via additive manufacturing with equivalent properties to the wrought counterpart without significant manipulation of laser parameters and scan strategies.

Nanofunctionalization of aluminum alloys with ZrH_2 particulates has been utilized for the first time in additive manufacturing to induce grain refinement of high strength aluminum alloys of wrought compositions producing a crack free material with strengths double that of the most common additively manufactured aluminum alloys. This new metallurgical approach is applicable to other industrially relevant crack susceptible alloys and can be extended to new families of additive manufacturing materials, such as nonweldable nickel alloys, superalloys and intermetallics. Furthermore, this breakthrough provides a new metallurgical tool for metals processing opening a rich portfolio of diverse alloys for additive manufacturing, accelerating broad adoption of additive processes, and enabling design of new alloy systems specifically for additive processing.

Chapter 6

Conclusions and Future Work

A new process, designated as *nanofunctionalization*, has been demonstrated as an effective method to introduce inoculants into additively manufactured alloys. This was shown to be an effective method of microstructure control during additive manufacturing beyond parametric control previously attempted in additive manufacturing[33,58,135,170]. Furthermore the control of solidification has been demonstrated as an effective method to eliminate hot cracking susceptibility of typically unweldable alloys[135]. This is the first demonstrated case of a 7000 series aluminum alloy being effectively processing in additive manufacturing demonstrating the applicability of additive manufacturing beyond castable and weldable alloy systems. This has produced a material with material specific strengths above the most conventional additive aluminum alloy (Al10SiMg), and rivals that of costly alloy systems such as titanium, maraging steel, and scandium alloyed aluminum (**Figure 6.1**).

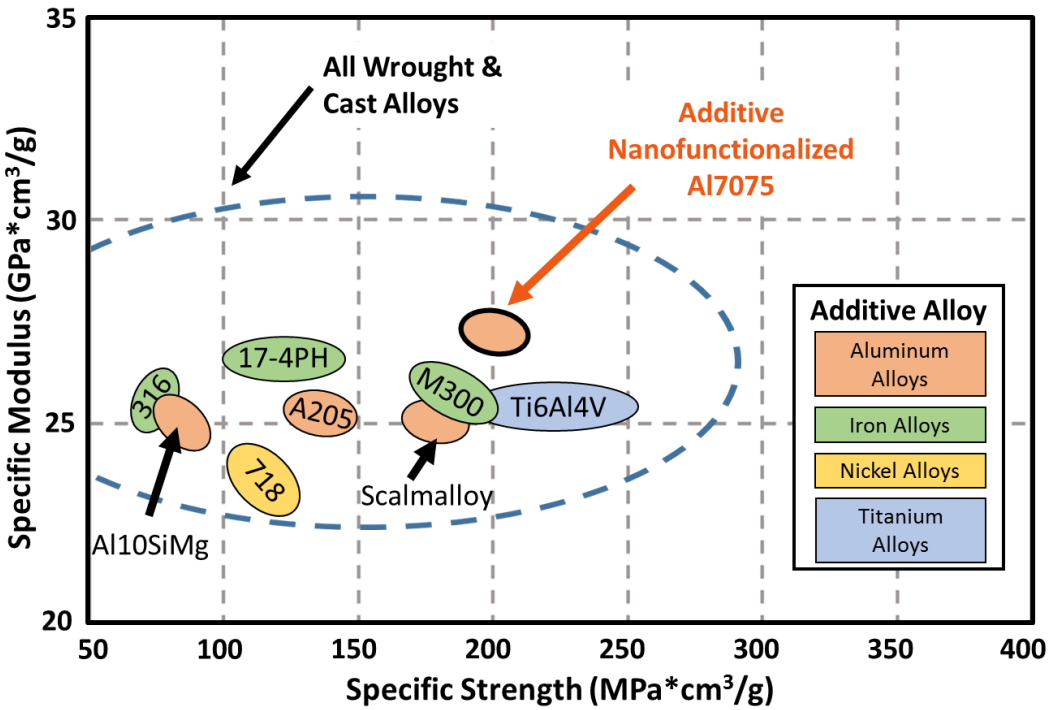

Figure 6.1: Specific Properties of Additive Alloys vs Conventionally Processed Alloys. Material properties of all wrought and cast alloy systems is based on an evaluation of common material properties in the Materials Handbook Desk Edition[19]. Additive alloy material properties are based on an evaluation of reported material properties in the Senvol Additive Materials database[20] as well as this study.

Hot cracking has been a significant issue in the processing of metal alloy systems for over a century[26]. Typically this is attributed to the composition of the alloy, and extensive studies have shown this link over casting and welding conditions[27,28]. This study has defined a new path to circumvent this paradigm, combing the unique features of additive manufacturing with the phenomena of inoculation to the evolution of crack susceptibility[135]. Decreasing the grain size during solidification and by extension increasing the solid fraction at which coherency occurs produces a semi-solid structure which can more easily accommodate the strains produced during solidification[135,174,185]. This will be important for not only the expansion of additive manufacturing to other crack-susceptible alloys, but also the design of new alloys specifically for additive manufacturing. With appropriate microstructure control, either

through inoculation, thermal control, or both, more alloy systems may be amenable to additive manufacturing.

6.1 Inoculation in Additive Alloys

The reduction of hot cracking and control of microstructure via inoculation in additive manufacturing presents many opportunities. However these can only be properly used if the mechanism by which this is accomplished is well understood. As described in Chapter 2 the additive process can produce large columnar microstructures with highly anisotropic properties. This is not ideal for implementation in most industrial applications. The parametric control of microstructures has been difficult to implement broadly across all alloy systems and processes[144,186]. The ability to inoculate metals during additive manufacturing provides a new, more effective mechanism which may be applied broadly across many alloy systems. This has the potential to improve the isotropic properties of material and reduce location specific variability across different build geometries.

The nanofunctionalization methodology provides additional freedom for inoculant selection. Other methodologies require in situ atomization with inoculants, which may be extremely difficult or impossible as described in Chapter 3 or require mechanical milling which would deform the particulate making particle flow and/or spreading difficult. Nanofunctionalization provides a route to introduce inoculants of arbitrary size, composition, or concentration into the additive process. This can enable rapid screening of these factors without the difficulty of atomization or milling. It has also been demonstrated that compositions, particularly hyperperitectic aluminum alloys, can be processed in this fashion. These are typically not processed due to the high liquidus temperature, but due to the high laser energy density and fast quenching enable compositions to be processes which

were not previously considered possible. The short times in the liquidus state also present potential opportunities to utilize inoculant systems which may not be fully stable in the melt. As the analysis in Chapter 4 showed, understanding dissolution rates of the included particulate can allow design of nanofunctionalized systems which can incorporate targeted particulates if the dissolution rates are properly controlled.

6.2 Role of Hyperperitectic Nucleation in Additive Aluminum Alloys

The ability to process materials in the hyperperitectic region of the Al-Ta and Al-Zr compositions has provided a new understanding of the mechanism of grain refinement from the Al_3Ta and Al_3Zr intermetallic systems. The high degree of lattice registry in the Al_3Zr system has been known, however the effectiveness of zirconium as an aluminum grain refiner has been limited. Instead the role of tantalum or zirconium has been limited to hypoperitectic compositions where the effect on nucleation behavior is dominated by the solute effects on undercooling rather than discrete nucleation events on the aforementioned intermetallics.

As described in Chapter 4, shifting to hyperperitectic compositions provides readily available Al_3Ta intermetallic nucleants which can provided high lattice registry interfaces for nucleation while in thermodynamic equilibrium with the FCC-aluminum phase producing a condition which can easily nucleate and grow. These compositions have not been investigated in the literature, partially for their high liquidus temperatures, but also due to processing difficulties where the dwell time in the two phase liquid and intermetallic region of the phase diagram leads to intermetallic coarsening. Additive manufacturing provides a unique processing condition which can effectively form a liquid and transit through the two phase liquid-intermetallic region of the phase diagram quickly enough to

avoid coarsening and provide a number density and size of intermetallic which is ideal for nucleation and growth.

The proposed mechanism of hyperperitectic nucleation in aluminum alloys indicates that solidifying though the Liquid + Al_3X region of the phase diagram into the Liquid + Al region of the phase diagram may not be as effective due to thermodynamic and kinetic impacts from the Al_3X to Al phase change. Additional experimental and first principles modeling work is likely necessary to validate this. Studies including in situ melting and solidification experiments utilizing synchrotron imaging and diffraction may provide insight into whether the phase transformation is impacting the growth velocity of the FCC-aluminum phase on previously seeded Al_3X intermetallic, or if the thermal transition through the Liquid + Al_3X region of the phase diagram is too short to nucleate a sufficient density of intermetallic species for nucleation to occur on a large enough scale to affect the microstructure.

Molecular dynamics simulations of the solidification process through the Liquid + Al_3X region of the phase diagram into the Liquid + Al region may indicate whether the associated thermodynamic and kinetic effects are of an order which could impact the nucleation and growth rates. While these are fundamental questions related to the exact mechanism of the specific alloy systems investigated here, there is additionally a spectrum of future work which should be investigated related to the practical implications of the high strength aluminum alloys produced and the expansion of the inoculant discover methodology's accuracy and applicability to other alloy systems.

6.3 Future Work

The research reported in this document serves as an initial proof of concept for the use of inoculants in additive manufacturing. While the results are promising for broader applicability, more research is needed to validate the demonstrated systems (e.g. Al 7075) for true industrial applicability, where material specifications and factors of safety are required for component design, and extend the nanofunctionalization process and inoculation to other alloy systems.

6.3.1 Additional Material Testing for High Strength Additive Aluminum

The use of high strength aluminum alloys with additive manufacturing has several significant benefits as previously described. However the results presented here focus mostly on the quasi-static tensile properties. This is only one property considered when implementing metal alloys in a true service application. Furthermore the results indicate that additional improvements to processing parameters may further improve the tested properties as well.

Initial work should focus on improving the additive manufacturing processing parameters to limit porosity in additive Al 7075. This is typically accomplished through multiple build iterations and parametric experimental designs, followed by response surface mapping to identify critical parameters. Current results indicate porosity, rather than lack of fusion, is the main detrimental defect. This indicates that laser energy density may be too high, or the powder size distribution may be incompatible with the machine configured layer height. The laser energy density issue is further complicated by the vaporization of zinc and magnesium alloying elements, which may be contributing to additional porosity. Balancing

the full fusion of material along with limiting vaporization of alloying elements is an area for future investigations.

Following the improvement of as built material quality, attention should be directed to understanding the heat treatment response. The tested heat treatment approach presented was limited and should be extended to investigate multiple common tempers in wrought aluminum alloys. It is likely that the change in compositions and thermomechanical history will impact solutionizing and aging time and temperatures. Analysis of as built material with differential scanning calorimetry can provide indications of shifts in liquidus temperature or any secondary reactions which may occur during these processes and inform appropriate heat treatment conditions.

Finally the material property analysis must be expanded beyond simple tensile results. The full spectrum of material properties which must be quantified will ultimately depend on the application. However typical aluminum alloy properties of particular interest are fatigue life, corrosion resistance, and stress corrosion cracking resistance. In many applications for complex geometry additive components local fatigue is likely and understanding the fatigue limits of that additive material will be crucial to understanding design life. Wrought aluminum alloys, specifically 7000 series alloys, are also susceptible to corrosion and stress corrosion cracking. Corrosion and fatigue can also be greatly impacted by the surface finish of the component. This is a major issue in laser powder bed additive manufacturing due to the fusion of residual powder to the component surface creating high surface areas susceptible to corrosion and fatigue crack growth[187]. It is also unclear how the change in microstructure as well as minor change in chemistry will impact these properties, but this will also be critical in selecting potential service conditions for

additive components and associated design life. Additionally the aforementioned processing and post processing conditions may impact these properties as well. It is likely that multiple iterations will be needed to optimize multiple properties due to the interconnected process-structure-property relationship and the multitude of variables which can be introduced in the additive process.

6.3.2 Improved Inoculant Discovery Algorithm

The proposed selection criteria for identifying nucleants and experimental results indicate the importance of the lattice matching effect on selecting effective inoculants. This is, however, a simplified approach and does not include many other physical phenomenon which could impact the nucleation event. It is likely that this analytical technique can be further improved by incorporating additional physics to eliminate the identification of false positives and negatives.

The first goal would be to introduce thermal effects into the model to account for thermal induced lattice expansion at the associated solidification conditions. While full coefficient of thermal expansion data across all crystallographic interfaces has not been calculated for all potential elements and compounds, analysis of the elastic constants of candidate material systems could provide an approximation of this effect as the elasticity of a material is related to the coefficient of thermal expansion. More detailed TEM studies of orientation relationships between inoculant particles and the aluminum matrix may also yield additional data to provide additional information for the inoculant selection criterion.

It may also be necessary to account for the attachment kinetics of material and solute effects. These are interrelated as solute can affect the surface energy of the solid liquid interface and in some cases adsorb or react with the target inoculant leading to a poisoning

effect. This could become important for more complex alloy systems where two candidate inoculants may be equivalent based on the lattice matching criteria but could have different effects based on the associated solidification conditions. This is a difficult effect to fully quantify, however modeling techniques such as molecular dynamics (**Figure 6.2**) can be leveraged to understand how introduction of solute elements may impact the critical nucleant undercooling and growth velocities during the solidification process on an inoculant.

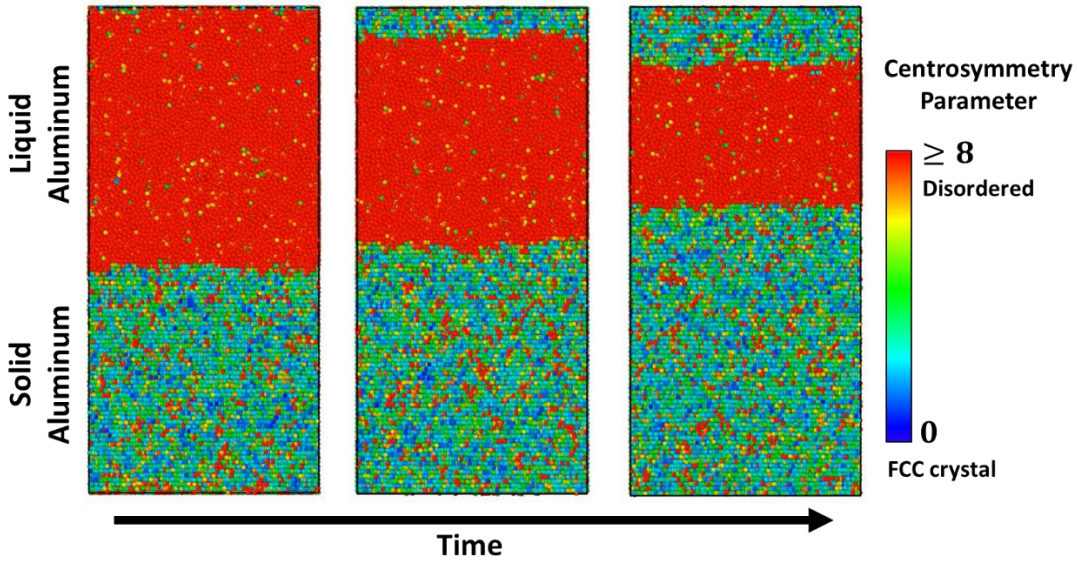

Figure 6.2: Molecular Dynamic Simulations of Aluminum Solidification. The simulation was conducted using >200,000 atoms with periodic boundary conditions. The liquid and solid sections were simulated independently then brought to a 5°C undercooling and combined into the same simulation to allow for solidification to occur epitaxially from the FCC aluminum substrate. The centrosymmetry parameter is used for visualization as a mechanism to track the velocity of the solidification front. A similar simulation could be conducted with different substrates and undercooling to effectively model the nucleation and growth conditions during heterogeneous nucleation.

6.3.3 Applicability to Other Alloy Systems

This dissertation has focused on aluminum alloys, however applicability of this nanofunctionalization approach to other systems is likely. There are several candidate systems which suffer many of the same solidification issues as hot crack susceptibility 7000

series aluminum alloys. One of particular interest is MAR-M-247, (**Figure 6.3**), which exhibits extensive cracking during additive processing. This particular nickel superalloy system, when processed conventionally, exhibits excellent properties at elevated temperatures, including high oxidation and creep resistance. These properties extend well beyond the best available additive superalloy, Inconel 718, and would enable several enhanced operational capacity of additive alloys[18,146].

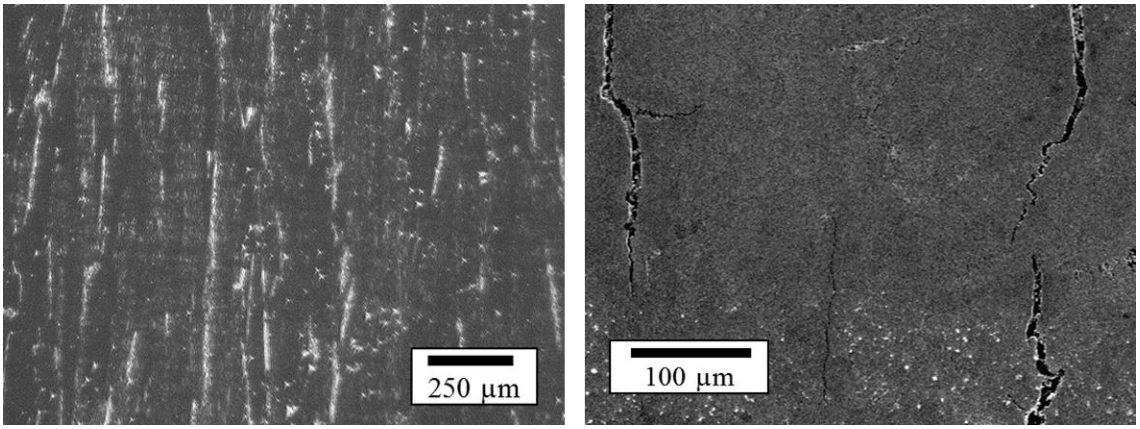

Figure 6.3: Additively Manufactured MAR-M-247. MAR-M-247 powder obtained from Praxair was processed using typical Inconel 718 parameter sets provided by Concept Laser on a Concept Laser M2 system. The resulting microstructure was severely cracked with long vertical cracking in the build orientation.

The cracking in MAR-M-247 tends to occur in the interdendritic regions vertically oriented with the build direction in a similar mechanism to the processed Al 7075 in Chapter 5. It is possible that identifying an appropriate nucleant for this system could allow for processing by increasing the solid fraction at which dendrite coherency occurs and reducing the interdendritic stress during solidification. While MAR-M-247 is a specific example, the nanofunctionalization and inoculation approach may be applicable across any crack susceptible system, but must be experimentally validated.

The opportunity to uniformly incorporate particulate in additive manufacturing is also important in the potential processing of metal matrix composites (MMC)[1,188]. Recently an Al10SiMg and tungsten carbide was demonstrated utilizing the

nanofunctionalization process[136]. While just a proof of concept, the material property increases at relatively low volume contents were impressive, with a 2X improvement in wear properties at 1 vol% particulate. These material property improvements could be extended to a variety of other alloy systems through production of a variety of MMC alloy systems. Additionally this is an important advancement due to the difficulty in processing complex geometry MMC systems from either processing or machining limitations.

Ultimately the nanofunctionalization process offers a variety of opportunities for new alloy development and expansion of available alloys for additive manufacturing. The initial demonstrations are promising, however more work is needed to understand the full capabilities and limitations of this process across not only the presented aluminum alloy systems, but other alloy systems as well.

References

[1] D. Herzog, V. Seyda, E. Wycisk, C. Emmelmann, Additive manufacturing of metals, Acta Mater. 117 (2016) 371–392. doi:10.1016/j.actamat.2016.07.019.

[2] J.J. Lewandowski, M. Seifi, Metal Additive Manufacturing: A Review of Mechanical Properties, Annu. Rev. Mater. Res. 46 (2016) 151–186. doi:10.1146/annurev-matsci-070115-032024.

[3] W.E. Frazier, Metal additive manufacturing: A review, J. Mater. Eng. Perform. 23 (2014). doi:10.1007/s11665-014-0958-z.

[4] B.H. Jared, M.A. Aguilo, L.L. Beghini, B.L. Boyce, B.W. Clark, A. Cook, B.J. Kaehr, J. Robbins, Additive manufacturing: Toward holistic design, Scr. Mater. 135 (2017) 141–147. doi:10.1016/j.scriptamat.2017.02.029.

[5] C.W. Hull, Apparatus for production of three-dimensional objects by stereolithography, 4575330, 1984.

[6] K. Cooper, Rapid Prototyping Technology: Selection and Application, Marcel Dekker, Inc., New York, NY, 2001. https://books.google.com.my/books?id=H50qMZFN4JEC.

[7] J.J. Beaman, C.R. Deckard, Selective Laser Sintering with Assisted Powder Handling, 4938816, 1989.

[8] Market for Aluminum Alloys in Additive Manufacturing : 2018 to 2028, An opportunity analysis and ten-year forecast, February 2, SmartechMarkets Publishing, 2018.

[9] Thomas Kellner, How 3D Printing Will Change Manufacturing - GE Reports, GE Reports. (2017). https://www.ge.com/reports/epiphany-disruption-ge-additive-chief-explains-3d-printing-will-upend-manufacturing/ (accessed July 15, 2018).

[10] First titanium 3D-printed part installed into serial production aircraft, Airbus. (2017). https://www.airbus.com/newsroom/press-releases/en/2017/09/first-titanium-3d-printed-part-installed-into-serial-production-.html (accessed July 15, 2018).

[11] Norsk Titanium Delivers First FAA-Certified, Additive Manufactured Ti64 Structural Aviation Components, Nor. Titan. (2017). http://www.norsktitanium.com/media/press/norsk-titanium-delivers-first-faa-certified-additive-manufactured-ti64-structural-aviation-components (accessed July 15, 2018).

[12] W. Associates, ed., Whohlers Report 2018: 3D Printing and Additive Manufacturing State of the Industry, Annual Worldwide Progress Report, Wohlers Associates, 2017.

[13] T. Mukherjee, J.S. Zuback, A. De, T. DebRoy, Printability of alloys for additive manufacturing., Sci. Rep. 6 (2016) 19717. doi:10.1038/srep19717.

[14] S. Moylan, J. Slotwinski, A. Cooke, K. Jurrens, M.A. Donmez, Lessons learned in establishing the NIST metal additive manufacturing laboratory, NIST Tech. Note 1801. (2013) 40. doi:10.6028/NIST.TN.1801.

[15] E. Incorporated, Measurement Science Roadmap for Metal-Based Additive Manufacturing, Natl. Inst. Stand. Technol. Rep. (2013) 86. doi:10.1007/s13398-014-0173-7.2.

[16] H. Ding, S.S. Dwaraknath, L. Garten, P. Ndione, D. Ginley, K.A. Persson,

Computational Approach for Epitaxial Polymorph Stabilization through Substrate Selection, ACS Appl. Mater. Interfaces. 8 (2016) 13086–13093. doi:10.1021/acsami.6b01630.
[17] N.T. Aboulkhair, N.M. Everitt, I. Maskery, I. Ashcroft, C. Tuck, Selective laser melting of aluminum alloys, MRS Bull. 42 (2017) 311–319. doi:10.1557/mrs.2017.63.
[18] S. Das, D.L. Bourell, S.S. Babu, Metallic materials for 3D printing, MRS Bull. 41 (2016) 729–741. doi:10.1557/mrs.2016.217.
[19] H.E. Boyer, T.L. Gail, Materials Handbook Desk Edition, ASM International, 1985.
[20] Senvol LLC, Material Database, (2018). http://senvol.com/material-search/ (accessed July 14, 2018).
[21] Renishaw and Aeromet work to optimise high-performance alloy, (2017). http://www.renishaw.com/en/renishaw-and-aeromet-work-to-optimise-high-performance-alloy--42645 (accessed July 19, 2018).
[22] MatWeb Material Property Data, (2016). www.matweb.com (accessed January 23, 2016).
[23] AP Works, Material Data Sheet- Scalmalloy, 2016.
[24] N. Kaufmann, M. Imran, T.M. Wischeropp, C. Emmelmann, S. Siddique, F. Walther, Influence of Process Parameters on the Quality of Aluminium Alloy EN AW 7075 Using Selective Laser Melting (SLM), Phys. Procedia. 83 (2016) 918–926. doi:10.1016/j.phpro.2016.08.096.
[25] M.L. Montero Sistiaga, R. Mertens, B. Vrancken, X. Wang, B. Van Hooreweder, J.P. Kruth, J. Van Humbeeck, Changing the alloy composition of Al7075 for better processability by selective laser melting, J. Mater. Process. Technol. 238 (2016) 437–445. doi:10.1016/j.jmatprotec.2016.08.003.
[26] W. Nelson, Duralumin Welding, Natl. Advis. Comm. Aeronaut. (1927).
[27] W.I. Pumphrey, J. V Lyons, Cracking During the Casting and Welding of the more common binary aluminum alloys, J. Inst. Met. 74 (1948) 439–455. papers3://publication/uuid/2DA83F1B-E935-4D3F-B24C-E04DA96A1CB6.
[28] P.H. Singer, A.R. & Jennings, Hot-Shortness of the Aluminum Silicon Alloys of Commercial Purity.pdf, J. Inst. Met. 73 (1946) 197–212.
[29] D. Bourell, J.P. Kruth, M. Leu, G. Levy, D. Rosen, A.M. Beese, A. Clare, Materials for additive manufacturing, CIRP Ann. - Manuf. Technol. 66 (2017) 659–681. doi:10.1016/j.cirp.2017.05.009.
[30] ISO / ASTM52900-15, Standard Terminology for Additive Manufacturing – General Principles – Terminology, ASTM International, West Conshohocken, PA, 2015. doi:10.1520/ISOASTM52900-15.
[31] Senvol LLC, Machine Database, (2018). http://senvol.com/machine-search/ (accessed July 19, 2018).
[32] J. Trapp, A.M. Rubenchik, G. Guss, M.J. Matthews, In situ absorptivity measurements of metallic powders during laser powder-bed fusion additive manufacturing, Appl. Mater. Today. 9 (2017) 341–349. doi:10.1016/j.apmt.2017.08.006.
[33] N. Raghavan, R. Dehoff, S. Pannala, S. Simunovic, M. Kirka, J. Turner, N. Carlson, S.S. Babu, Numerical modeling of heat-transfer and the influence of process parameters on tailoring the grain morphology of IN718 in electron beam additive

manufacturing, Acta Mater. 112 (2016) 303–314. doi:10.1016/j.actamat.2016.03.063.
[34] S. Catchpole-Smith, N. Aboulkhair, L. Parry, C. Tuck, I.A. Ashcroft, A. Clare, Fractal scan strategies for selective laser melting of 'unweldable' nickel superalloys, Addit. Manuf. 15 (2017) 113–122. doi:10.1016/j.addma.2017.02.002.
[35] S. Kou, Welding Metallurgy, Wiley-Interscience, 2003. doi:10.1016/j.theochem.2007.07.017.
[36] V. Ploshikhin, A. Prikhodovsky, M. Makhutin, A. Ilin, H. Zoch, Integrated Mechanical-Metallurgical Approach to Modeling of Solidification Cracking in Welds, (n.d.).
[37] F.R. Collins, J.H. Dudas, Preventing Weld Cracks in High-Strength Aluminum Alloys, Weld. J. 45 (1966) 241..
[38] J.N. DuPont, Fundamentals of Weld Solidification, ASM Handb. Vol 6, Welding, Brazing Solder. 6 (2011) 96–114. doi:10.1361/asmhba000.
[39] D.M. Stefanescu, Science and Engineering of Casting Solidification, Springer, 2009. doi:10.1007/s13398-014-0173-7.2.
[40] J.R. Davis, Aluminum and Aluminum Alloys, Light Met. Alloy. (2001) 66. doi:10.1361/autb2001p351.
[41] H.-S. Kim, Y.-T. Im, M. Geiger, Prediction of Ductile Fracture in Cold Forging of Aluminum Alloy, J. Manuf. Sci. Eng. 121 (1999) 336. doi:10.1115/1.2832686.
[42] M. Jain, J. Allin, M.J. Bull, Deep drawing characteristics of automotive aluminum alloys, Mater. Sci. Eng. A. 256 (1998) 69–82. doi:10.1016/S0921-5093(98)00845-4.
[43] S. Lee, P.B. Berbon, M. Furukawa, Z. Horita, M. Nemoto, N.K. Tsenev, R.Z. Valiev, T.G. Langdon, Developing superplastic properties in an aluminum alloy through severe plastic deformation, Mater. Sci. Eng. A. 272 (1999) 63–72. doi:10.1016/S0921-5093(99)00470-0.
[44] J.P. Davim, Machining : fundamentals and recent advances, Springer, 2008.
[45] M. Schmidt, M. Merklein, D. Bourell, D. Dimitrov, T. Hausotte, K. Wegener, L. Overmeyer, F. Vollertsen, G.N. Levy, Laser based additive manufacturing in industry and academia, CIRP Ann. - Manuf. Technol. 66 (2017) 561–583. doi:10.1016/j.cirp.2017.05.011.
[46] H. Ali, H. Ghadbeigi, K. Mumtaz, Effect of scanning strategies on residual stress and mechanical properties of Selective Laser Melted Ti6Al4V, Mater. Sci. Eng. A. 712 (2018) 175–187. doi:10.1016/j.msea.2017.11.103.
[47] S.H. Sun, K. Hagihara, T. Nakano, Effect of scanning strategy on texture formation in Ni-25 at.%Mo alloys fabricated by selective laser melting, Mater. Des. 140 (2018) 307–316. doi:10.1016/j.matdes.2017.11.060.
[48] L. Thijs, B. Vrancken, J. Kruth, J. Van Humbeeck, The influence of process parameters and scanning strategy on the texture in Ti6Al4V part produced by selective laser melting, Adv. Mater. Process. Appl. Addit. Manuf. Mater. Sci. Technol. Montr. Canada, 27-31 Oct. (2013) 21–28.
[49] M.M. Kirka, P. Nandwana, Y. Lee, R.R. Dehoff, Solidification and solid-state transformation sciences in metals additive manufacturing, Scr. Mater. 135 (2017) 130–134. doi:10.1016/j.scriptamat.2017.01.005.
[50] W. Kurz, D.J. Fisher, Fundamentals of Solidification, Trans Tech Publications Ltd., 1998.
[51] J.A. Dantzig, M. Rappaz, Solidification, EPFL Press, 2009.

[52] S. Kou, A criterion for cracking during solidification, Acta Mater. 88 (2015) 366–374. doi:10.1016/j.actamat.2015.01.034.
[53] S. Karagadde, P.D. Lee, B. Cai, J.L. Fife, M.A. Azeem, K.M. Kareh, C. Puncreobutr, D. Tsivoulas, T. Connolley, R.C. Atwood, Transgranular liquation cracking of grains in the semi-solid state, Nat. Commun. 6 (2015) 8300. doi:10.1038/ncomms9300.
[54] E. Chauvet, P. Kontis, E.A. Jägle, B. Gault, D. Raabe, J.-J. Blandin, R. Dendievel, B. Vayre, S. Abed, G. Martin, C. Tassin, Hot cracking mechanism affecting a non-weldable Ni-based superalloy produced by Selective Electron Beam Melting, Acta Mater. 142 (2017) 82–94. doi:10.1016/j.actamat.2017.09.047.
[55] J. Wannasin, R. Canyook, S. Wisutmethangoon, M.C. Flemings, Grain refinement behavior of an aluminum alloy by inoculation and dynamic nucleation, Acta Mater. 61 (2013). doi:10.1016/j.actamat.2013.03.029.
[56] S. Thangaraju, M. Heilmaier, B.S. Murty, S.S. Vadlamani, On the Estimation of True Hall-Petch Constants and Their Role on the Superposition Law Exponent in Al Alloys, Adv. Eng. Mater. 14 (2012) 892–897. doi:10.1002/adem.201200114.
[57] J. Beuth, J. Fox, J. Gockel, C. Montgomery, R. Yang, H. Qiao, S. Emrecan, P. Reeseewatt, A. Anvari, S. Narra, N. Klingbeil, Process mapping for qualification across multiple direct metal additive manufacturing processes, in: Proc. SFF Symp. Austin, TX, 2013. doi:10.1017/CBO9781107415324.004.
[58] R.R. Dehoff, M.M. Kirka, W.J. Sames, H. Bilheux, A.S. Tremsin, L.E. Lowe, S.S. Babu, Site specific control of crystallographic grain orientation through electron beam additive manufacturing, Mater. Sci. Technol. 31 (2015) 931–938. doi:10.1179/1743284714Y.0000000734.
[59] A.L. Greer, Grain refinement of alloys by inoculation of melts, Philos. Trans. R. Soc. A. 361 (2003) 479–495.
[60] W. King, A.T. Anderson, R.M. Ferencz, N.E. Hodge, C. Kamath, S.A. Khairallah, Overview of modelling and simulation of metal powder bed fusion process at Lawrence Livermore National Laboratory, Mater. Sci. Technol. 31 (2015) 957–968. doi:10.1179/1743284714Y.0000000728.
[61] M.M. Kirka, K.A. Unocic, N. Raghavan, F. Medina, R.R. Dehoff, S.S. Babu, Microstructure Development in Electron Beam-Melted Inconel 718 and Associated Tensile Properties, Jom. 68 (2016) 1012–1020. doi:10.1007/s11837-016-1812-6.
[62] Y. Ding, J.A. Muñiz-Lerma, M. Trask, S. Chou, A. Walker, M. Brochu, Microstructure and mechanical property considerations in additive manufacturing of aluminum alloys, MRS Bull. 41 (2016) 745–751. doi:10.1557/mrs.2016.214.
[63] S.M. Thompson, L. Bian, N. Shamsaei, A. Yadollahi, An overview of Direct Laser Deposition for additive manufacturing; Part I: Transport phenomena, modeling and diagnostics, Addit. Manuf. 8 (2015) 36–62. doi:10.1016/j.addma.2015.07.001.
[64] V. Gunenthiram, P. Peyre, M. Schneider, M. Dal, F. Coste, I. Koutiri, R. Fabbro, Experimental analysis of spatter generation and melt-pool behavior during the powder bed laser beam melting process, J. Mater. Process. Technol. 251 (2018) 376–386. doi:10.1016/j.jmatprotec.2017.08.012.
[65] E. Schleip, R. Willnecker, D.M. Herlach, G.P. Görler, Measurements of ultrarapid solidification rates in greatly undercooled bulk melts with a high speed photosensing device, Mater. Sci. Eng. 98 (1988) 39–42. doi:10.1016/0025-5416(88)90122-X.
[66] D. Turnbull, Kinetics of solidification of supercooled liquid mercury droplets, J.

Chem. Phys. 20 (1952) 411–424. doi:10.1063/1.1700435.
[67] D. Turnbull, Kinetics of heterogeneous nucleation, J. Chem. Phys. 18 (1950) 198–203. doi:doi:10.1063/1.1747588.
[68] D. Turnbull, J.C. Fisher, Rate of nucleation in condensed systems, J. Chem. Phys. 17 (1949) 71–73. doi:10.1063/1.1747055.
[69] J.D. Hunt, Steady State Columnar and Equiaxed Growth of Dendrites and Eutectic, Mater. Sci. Eng. 65 (1984) 75–83.
[70] W. Kurz, C. Benzencon, M. Gaumann, Columnar to Equiaxed Transition in Solidification Processing, Sci. Technol. Adv. Mater. 2. (2001) 185–191.
[71] J.R. Davis & Associates., ASM International. Handbook Committee., Aluminum and aluminum alloys, ASM International, 1993.
[72] Thermo-Calc Software, TCAL4 Aluminum Alloy Database V4, (2016).
[73] T.B. Massalski, The Al-Cu (Aluminum-Copper) System, J. Phase Equilibria. 1 (1980) 27–33.
[74] R.W. Balluffi, S. Allen, W.C. Carter, Kinetics of Materials, Wiley, 2005. https://books.google.com/books/about/Kinetics_of_Materials.html?id=QNTxYPvovCEC&pgis=1 (accessed January 22, 2016).
[75] P.M. Smith, R. Reitano, M.J. Aziz, Solute Trapping in Metals, in: Mater. Res. Soc. Syposium, 1993: pp. 749–754.
[76] M.J. Aziz, Model for solute redistribution during rapid solidification, J. Appl. Phys. 53 (1982) 1158–1168. doi:10.1063/1.329867.
[77] M. Gäumann, R. Trivedi, W. Kurz, Nucleation ahead of the advancing interface in directional solidification, Mater. Sci. Eng. A. 226–228 (1997) 763–769. doi:10.1016/S0921-5093(97)80081-0.
[78] M.A. Easton, D. St John, An analysis of the relationship between grain size, solute content, and the potency and number density of nucleant particles, Metall. Mater. Trans. A Phys. Metall. Mater. Sci. 36 (2005) 1911–1920. doi:10.1007/s11661-005-0054-y.
[79] R.E. Rudd, W.H. Cabot, K.J. Caspersen, J. a. Greenough, D.F. Richards, F.H. Streitz, P.L. Miller, Self-diffusivity and interdiffusivity of molten aluminum-copper alloys under pressure, derived from molecular dynamics, Phys. Rev. E. 85 (2012) 031202. doi:10.1103/PhysRevE.85.031202.
[80] B. Zhang, a. Griesche, a. Meyer, Diffusion in Al-Cu melts studied by time-resolved X-ray radiography, Phys. Rev. Lett. 104 (2010) 2–5. doi:10.1103/PhysRevLett.104.035902.
[81] E.A. Brandes, G.B. Brook, Smithells Metals Reference Book, 7th ed., Reed Educational and Professional Publishing Ltd, 1992.
[82] M. Gunduz, J.D. Hunt, The Measurment of Solid-Liquid Surface Energies in the Al-Cu, Al-Si, and Pb-Sn Systems, Acta Met. 33 (1985) 1651–1672.
[83] P. André, D. Jácome, N. Von Paraski, A.F. Ferreira, A. Garcia, I.L. Ferreira, Evolution of Surface Tension and Gibbs-Thomson Coefficient During Aluminum Alloys Solidification, 7th Brazilian Congr. Manuf. Eng. (2013).
[84] P.M. Smith, M.J. Aziz, Solute Trapping in Aluminum Alloys, Acta Met. Mater. 42 (1994) 3515–3525.
[85] A.L. Greer, A.M. Bunn, A. Tronche, P. V. Evans, D.J. Bristow, Modelling of inoculation of metallic melts: application to grain refinement of aluminium by Al-Ti-

B, Acta Mater. 48 (2000) 2823–2835. doi:10.1016/S1359-6454(00)00094-X.
[86] C. xia SHI, G. guang CHENG, Z. jun LI, P. ZHAO, Solidification Structure Refining of 430 Ferrite Stainless Steel With TiN Nucleation, J. Iron Steel Res. Int. 15 (2008) 57–60. doi:10.1016/S1006-706X(08)60126-0.
[87] M. Zielińska, J. Sieniawski, M. Poręba, Microstructure and mechanical properties of high temperature creep resisting superalloy Rene 77 modified CoAl2O4, Arch. Mater. …. 28 (2007) 629–632. http://yadda.icm.edu.pl/baztech/element/bwmeta1.element.baztech-article-BWAN-0002-0013.
[88] T.E. Quested, A.L. Greer, The effect of the size distribution of inoculant particles on as-cast grain size in aluminium alloys, Acta Mater. 52 (2004) 3859–3868. doi:10.1016/j.actamat.2004.04.035.
[89] S. Suresh, N.S.V. Moorthi, Aluminium- Titanium diboride (Al-TiB2) metal matrix composites: Challenges and opportunities, Procedia Eng. 38 (2012) 89–97. doi:10.1016/j.proeng.2012.06.013.
[90] M.X. Zhang, P.M. Kelly, M.A. Easton, J.A. Taylor, Crystallographic study of grain refinement in aluminum alloys using the edge-to-edge matching model, Acta Mater. 53 (2005) 1427–1438. doi:10.1016/j.actamat.2004.11.037.
[91] F. Wang, D. Qiu, Z.L. Liu, J. Taylor, M. Easton, M.X. Zhang, Crystallographic study of Al3Zr and Al3Nb as grain refiners for Al alloys, Trans. Nonferrous Met. Soc. China (English Ed. 24 (2014) 2034–2040. doi:10.1016/S1003-6326(14)63309-4.
[92] P. Schumacher, A.L. Greer, J. Worth, P. V. Evans, M. a. Kearns, P. Fisher, a. H. Green, New studies of nucleation mechanisms in aluminium alloys: implications for grain refinement practice, Mater. Sci. Technol. 14 (1998) 394–404. doi:10.1179/026708398790301241.
[93] a M. Bunn, P. Schumacher, M. a Kearns, C.B. Boothroyd, a L. Greer, Grain refinement by Al–Ti–B alloys in aluminium melts: a study of the mechanisms of poisoning by zirconium, Mater. Sci. …. 15 (1999) 1115–1123. doi:10.1179/026708399101505158.
[94] D. Wearing, A.P. Horsfield, W. Xu, P.D. Lee, Which wets TiB2inoculant particles: Al or Al3Ti?, J. Alloys Compd. 664 (2016) 460–468. doi:10.1016/j.jallcom.2015.12.203.
[95] M.A. Easton, D. Stjohn, Grain Refinement of Aluminum Alloys : Part I . The Nucleant and Solute Paradigms — A Review of the Literature, Metall. Mater. Trans. A. 30 (1999) 1613–1623. doi:10.1007/s11661-999-0098-5.
[96] M.A. Easton, D. StJohn, Grain refinement of aluminum alloys: Part II. Confirmation of, and a mechanism for, the solute paradigm, Metall. Mater. Trans. A. 30 (1999) 1625–1633. doi:10.1007/s11661-999-0099-4.
[97] M.X. Zhang, P.M. Kelly, Edge-to-edge matching and its applications: Part I. Application to the simple HCP/BCC system, Acta Mater. 53 (2005) 1073–1084. doi:10.1016/j.actamat.2004.11.007.
[98] J. Schmitz, J. Brillo, I. Egry, R. Schmid-Fetzer, Surface Tension of Liquid Al – Cu Binary Alloys, Int. J. Mat. Res. 100 (2009) 1529–1535.
[99] A.L. Greer, T.E. Quested, Heterogeneous grain initiation in solidification, Philos. Mag. 86 (2006) 3665–3680. doi:10.1080/14786430500198486.
[100] A. Basak, S. Das, Epitaxy and Microstructure Evolution in Metal Additive

Manufacturing, Annu. Rev. Mater. Res. 46 (2015) annurev-matsci-070115-031728. doi:10.1146/annurev-matsci-070115-031728.
[101] A.L. Greer, Overview: Application of heterogeneous nucleation in grain-refining of metals, J. Chem. Phys. 145 (2016) 211704. doi:10.1063/1.4968846.
[102] L.E. Lindgren, A. Lundbäck, M. Fisk, R. Pederson, J. Andersson, Simulation of additive manufacturing using coupled constitutive and microstructure models, Addit. Manuf. 12 (2016) 144–158. doi:10.1016/j.addma.2016.05.005.
[103] W.E. King, A.T. Anderson, R.M. Ferencz, N.E. Hodge, C. Kamath, S.A. Khairallah, A.M. Rubenchik, Laser powder bed fusion additive manufacturing of metals; physics, computational, and materials challenges, Appl. Phys. Rev. 2 (2015) 041304. doi:10.1063/1.4937809.
[104] M.J. Matthews, G. Guss, S.A. Khairallah, A.M. Rubenchik, P.J. Depond, W.E. King, Denudation of metal powder layers in laser powder bed fusion processes, Acta Mater. 114 (2016) 33–42. doi:10.1016/j.actamat.2016.05.017.
[105] S.A. Khairallah, A.T. Anderson, A. Rubenchik, W.E. King, Laser powder - bed fusion additive manufacturing: physics of complex melt flow and formation mechanisms of pore s , spatter , and denudation zone s, Acta Mater. 108 (2016) 1–25.
[106] U. Scipioni Bertoli, G. Guss, S. Wu, M.J. Matthews, J.M. Schoenung, In-situ characterization of laser-powder interaction and cooling rates through high-speed imaging of powder bed fusion additive manufacturing, Mater. Des. 135 (2017) 385–396. doi:10.1016/j.matdes.2017.09.044.
[107] S. Ly, A.M. Rubenchik, S.A. Khairallah, G. Guss, M.J. Matthews, Metal vapor micro-jet controls material redistribution in laser powder bed fusion additive manufacturing, Sci. Rep. 7 (2017) 1–12. doi:10.1038/s41598-017-04237-z.
[108] P.C. Collins, D.A. Brice, P. Samimi, I. Ghamarian, H.L. Fraser, Microstructural Control of Additively Manufactured Metallic Materials, Annu. Rev. Mater. Res. 46 (2016) 63–91. doi:10.1146/annurev-matsci-070115-031816.
[109] T.M. Rodgers, J.D. Madison, V. Tikare, Simulation of metal additive manufacturing microstructures using kinetic Monte Carlo, Comput. Mater. Sci. 135 (2017) 78–89. doi:10.1016/j.commatsci.2017.03.053.
[110] F. Wang, D. Qiu, Z.L. Liu, J.A. Taylor, M.A. Easton, M.X. Zhang, The grain refinement mechanism of cast aluminium by zirconium, Acta Mater. 61 (2013) 5636–5645. doi:10.1016/j.actamat.2013.05.044.
[111] Z. Chen, H. Kang, G. Fan, J. Li, Y. Lu, J. Jie, Y. Zhang, T. Li, X. Jian, T. Wang, Grain refinement of hypoeutectic Al-Si alloys with B, Acta Mater. 120 (2016) 168–178. doi:10.1016/j.actamat.2016.08.045.
[112] J. Wang, A. Horsfield, U. Schwingenschlogl, P.D. Lee, Heterogeneous Nucleation of Solid Al from the melt by TiB2 and Al3Ti, an ab initio molecular dynamics study, Phys. Rev. B. 82 (2010). doi:10.1016/j.jallcom.2013.09.179.
[113] W.-S. Tian, Q.-L. Zhao, R. Geng, F. Qiu, Q.-C. Jiang, Improved creep resistance of Al-Cu alloy matrix composite reinforced with bimodal-sized TiC p, Mater. Sci. Eng. A. (2017). doi:10.1016/j.msea.2017.12.071.
[114] S.H. Seyed Ebrahimi, M. Emamy, Effects of Al-5Ti-1B and Al-5Zr master alloys on the structure, hardness and tensile properties of a highly alloyed aluminum alloy, Mater. Des. 31 (2010) 200–209. doi:10.1016/j.matdes.2009.06.031.
[115] B.S. Murty, S. a. Kori, M. Chakraborty, Grain refinement of aluminium and its alloys

by heterogeneous nucleation and alloying, Int. Mater. Rev. 47 (2002) 3–29. doi:10.1179/095066001225001049.
[116] A.T. Thomas, R. Parameshwaran, A. Muthukrishnan, M.A. Kumaran, Development of Feeding & Stirring Mechanisms for Stir Casting of Aluminium Matrix Composites, Procedia Mater. Sci. 5 (2014) 1182–1191. doi:10.1016/j.mspro.2014.07.415.
[117] F. Wang, D. Eskin, J. Mi, T. Connolley, J. Lindsay, A refining mechanism of primary Al3Ti intermetallic particles by ultrasonic treatment in the liquid state, Acta Mater. 116 (2016) 354–363. doi:10.1016/j.actamat.2016.06.056.
[118] D.K. Koli, G. Agnihotri, R. Purohit, Properties and Characterization of Al-Al 2 O 3 Composites Processed by Casting and Powder Metallurgy Routes (Review), Int. J. Latest Trends Eng. Technol. 2 (2013) 486–496.
[119] P. Xiao, Y. Gao, C. Yang, Z. Liu, Y. Li, F. Xu, Microstructure, mechanical properties and strengthening mechanisms of Mg matrix composites reinforced with in situ nanosized TiB 2 particles, Mater. Sci. Eng. A. 710 (2018) 251–259. doi:10.1016/j.msea.2017.10.107.
[120] M.N. Ahsan, A.J. Pinkerton, R.J. Moat, J. Shackleton, A comparative study of laser direct metal deposition characteristics using gas and plasma-atomized Ti–6Al–4V powders, Mater. Sci. Eng. A. 528 (2011) 7648–7657. doi:10.1016/J.MSEA.2011.06.074.
[121] A. Ünal, Liquid break-up in gas atomization of fine aluminum powders, Metall. Trans. B. 20 (1989) 61–69. doi:10.1007/BF02670350.
[122] X. gang Li, U. Fritsching, Process modeling pressure-swirl-gas-atomization for metal powder production, J. Mater. Process. Technol. 239 (2017) 1–17. doi:10.1016/j.jmatprotec.2016.08.009.
[123] A. Allimant, M.P. Planche, Y. Bailly, L. Dembinski, C. Coddet, Progress in gas atomization of liquid metals by means of a De Laval nozzle, Powder Technol. 190 (2009) 79–83. doi:10.1016/j.powtec.2008.04.071.
[124] I. Uslan, S. Saritas, T.J. Davies, Effects of variables on size and characteristics of gas atomised aluminium powders, Powder Metall. 42 (1999) 157–163. doi:10.1179/003258999665512.
[125] A. Ünal, Effect of processing variables on particle size in gas atomization of rapidly solidified aluminium powders, Mater. Sci. Technol. 3 (1987) 1029–1039. doi:10.1179/mst.1987.3.12.1029.
[126] Y. Kakinuma, M. Mori, Y. Oda, T. Mori, M. Kashihara, A. Hansel, M. Fujishima, Influence of metal powder characteristics on product quality with directed energy deposition of Inconel 625, CIRP Ann. 65 (2016) 209–212. doi:10.1016/J.CIRP.2016.04.058.
[127] A.B. Spierings, M. Voegtlin, T. Bauer, K. Wegener, Powder flowability characterisation methodology for powder-bed-based metal additive manufacturing, Prog. Addit. Manuf. 1 (2016) 9–20. doi:10.1007/s40964-015-0001-4.
[128] I.E. Anderson, R.L. Terpstra, Progress toward gas atomization processing with increased uniformity and control, Mater. Sci. Eng. A. 326 (2002) 101–109. doi:10.1016/S0921-5093(01)01427-7.
[129] S. Lagutkin, L. Achelis, S. Sheikhaliev, V. Uhlenwinkel, V. Srivastava, Atomization process for metal powder, Mater. Sci. Eng. A. 383 (2004) 1–6.

doi:10.1016/j.msea.2004.02.059.
[130] J. Murray, A. Peruzzi, J.P. Abriata, The Al-Zr (Aluminum-Zirconium) System, J. Phase Equilibria. 13 (1992) 277–291.
[131] C.C. Koch, Materials Synthesis by Mechanical Alloying, Annu. Rev. Mater. Sci. 19 (1989) 121–143. doi:10.1146/annurev.ms.19.080189.001005.
[132] C. Suryanarayana, Mechanical alloying and milling, Prog. Mater. Sci. 46 (2001) 1–184. doi:10.1016/S0079-6425(99)00010-9.
[133] D.E. Cooper, N. Blundell, S. Maggs, G.J. Gibbons, Additive layer manufacture of Inconel 625 metal matrix composites, reinforcement material evaluation, J. Mater. Process. Technol. 213 (2013) 2191–2200. doi:10.1016/j.jmatprotec.2013.06.021.
[134] D. Gu, H. Wang, F. Chang, D. Dai, P. Yuan, Y.C. Hagedorn, W. Meiners, Selective laser melting additive manufacturing of TiC/AlSi10Mg bulk-form nanocomposites with tailored microstructures and properties, Phys. Procedia. 56 (2014) 108–116. doi:10.1016/j.phpro.2014.08.153.
[135] J.H. Martin, B.D. Yahata, J.M. Hundley, J.A. Mayer, T.A. Schaedler, T.M. Pollock, 3D printing of high-strength aluminium alloys, Nature. 549 (2017). doi:10.1038/nature23894.
[136] J.H. Martin, B.D. Yahata, E.C. Clough, J.A. Mayer, J.M. Hundley, T.A. Schaedler, Additive manufacturing of metal matrix composites via nanofunctionalization, MRS Commun. (2018). doi:10.1557/mrc.2018.95.
[137] Z. Fan, An epitaxial model for heterogeneous nucleation on potent substrates, Metall. Mater. Trans. A Phys. Metall. Mater. Sci. 44 (2013) 1409–1418. doi:10.1007/s11661-012-1495-8.
[138] M.A. Easton, M. Qian, A. Prasad, D.H. StJohn, Recent advances in grain refinement of light metals and alloys, Curr. Opin. Solid State Mater. Sci. 20 (2015) 13–24. doi:10.1016/j.cossms.2015.10.001.
[139] S.P. Ong, W.D. Richards, A. Jain, G. Hautier, M. Kocher, S. Cholia, D. Gunter, V.L. Chevrier, K. Persson, G. Ceder, Python Materials Genomics (pymatgen) : A Robust, Open-Source Python Library for Materials Analysis., Comput. Mater. Sci. 68 (2013) 314–319. doi:10.1016/j.commatsci.2012.10.028.
[140] A. Jain, G. Hautier, S.P. Ong, C. Moore, C. Fischer, K. Persson, G. Ceder, Formation enthalpies by mixing GGA and GGA + U calculations., Phys. Rev. B. 84 (2011) 045115. doi:10.1103/PhysRevB.84.045115.
[141] S.S. Sih, J.W. Barlow, The prediction of the emissivity and thermal conductivity of powder beds, Part. Sci. Technol. 22 (2004) 427–440. doi:10.1080/02726350490501682.
[142] J. Goicoechea, C. Garcia-Cordovilla, E. Louis, A. Pamies, Surface tension of binary and ternary aluminium alloys of the systems Al-Si-Mg and Al-Zn-Mg, J. Mater. Sci. 27 (1992) 5247–5252. doi:10.1007/PL00020247.
[143] F. Abe, M. Shiomi, K. Osakada, Solidifying Behaviour of Metallic Powder in Selective Laser Melting Process, Procedia Eng. 207 (2017) 1188–1193. doi:10.1016/j.proeng.2017.10.1051.
[144] J. Gockel, L. Sheridan, S.P. Narra, N.W. Klingbeil, J. Beuth, Trends in Solidification Grain Size and Morphology for Additive Manufacturing of Ti-6Al-4V, JOM. 69 (2017) 2706–2710. doi:10.1007/s11837-017-2601-6.
[145] J.H. Martin, B.D. Yahata, J.M. Hundley, J.A. Mayer, T.A. Schaedler, T.M. Pollock,

3D printing of high-strength aluminium alloys, Nature. (2017). doi:10.1038/nature23894.
[146] M.M. Attallah, R. Jennings, X. Wang, L.N. Carter, Additive manufacturing of Ni-based superalloys: The outstanding issues, MRS Bull. 41 (2016) 758–764. doi:10.1557/mrs.2016.211.
[147] F. Wang, Z. Liu, D. Qiu, J.A. Taylor, M.A. Easton, M.X. Zhang, Revisiting the role of peritectics in grain refinement of Al alloys, Acta Mater. 61 (2013) 360–370. doi:10.1016/j.actamat.2012.09.075.
[148] M. Johnsson, A Critical Survey of the Grain Refining Mechanisms in Aluminium, Stockholm University, 1993.
[149] M.A. Easton, D.H. Stjohn, A model of grain refinement incorporating alloy constitution and potency of heterogeneous nucleant particles, Acta Mater. 49 (2001) 1867–1878. doi:10.1016/S1359-6454(00)00368-2.
[150] Y. Du, R. Schmid-Fetzer, Thermodynamic Modeling of the Al-Ta System, J. Phase Equilibria. 17 (1996) 311–324.
[151] V.T. Witusiewicz, A.A. Bondar, U. Hecht, J. Zollinger, V.M. Petyukh, O.S. Fomichov, V.M. Voblikov, S. Rex, Experimental study and thermodynamic re-assessment of the binary Al-Ta system, Intermetallics. 18 (2010) 92–106. doi:10.1016/j.intermet.2009.06.015.
[152] V.N. Yerembnko, Y. V. Natanzon, V.I. Dybkov, Interaction of the refractory metals with liquid aluminium, J. Less-Common Met. 50 (1976) 29–48. doi:10.1016/0022-5088(76)90251-4.
[153] M. Qian, P. Cao, M.A. Easton, S.D. McDonald, D.H. StJohn, An analytical model for constitutional supercooling-driven grain formation and grain size prediction, Acta Mater. 58 (2010) 3262–3270. doi:10.1016/j.actamat.2010.01.052.
[154] Z. Fan, Y. Wang, Y. Zhang, T. Qin, X.R. Zhou, G.E. Thompson, T. Pennycook, T. Hashimoto, Grain refining mechanism in the Al/Al-Ti-B system, Acta Mater. 84 (2015) 292–304. doi:10.1016/j.actamat.2014.10.055.
[155] O. Zinovieva, A. Zinoviev, V. Ploshikhin, Three-dimensional modeling of the microstructure evolution during metal additive manufacturing, Comput. Mater. Sci. 141 (2018) 207–220. doi:10.1016/j.commatsci.2017.09.018.
[156] E. Pascal, S. Singh, P.G. Callahan, B. Hourahine, C. Trager-Cowan, M. De Graef, Energy-weighted dynamical scattering simulations of electron diffraction modalities in the scanning electron microscope, Ultramicroscopy. 188 (2018) 101. doi:10.1016/j.ultramic.2018.03.026.
[157] P.G. Callahan, M. De Graef, Dynamical Electron Backscatter Diffraction Patterns. Part I: Pattern Simulations, Microsc. Microanal. 19 (2013) 1255–1265. doi:10.1017/S1431927613001840.
[158] M. De Graef, Introduction to conventional transmission electron microscopy, Cambridge University Press, 2003.
[159] L. Han, Y. Sui, Q. Wang, K. Wang, Y. Jiang, Effects of Nd on microstructure and mechanical properties of cast Al-Si-Cu-Ni-Mg piston alloys, J. Alloys Compd. 695 (2017) 1566–1572. doi:10.1016/j.jallcom.2016.10.300.
[160] D. Hull, D.J. Bacon, Introduction to Dislocations, 5th Editio, Elsevier Ltd., 2011.
[161] K. Wierzbanowski, M. Kotra, M. Wronski, K. Sztwiertnia, S. Wronski, A. Lodini, Modeling of recrystallization texture of aluminium: Symmetric and asymmetric

rolling, IOP Conf. Ser. Mater. Sci. Eng. 82 (2015). doi:10.1088/1757-899X/82/1/012039.
[162] J. Hjelen, R. Orsund, E. Nes, On the Origin of Recrystallization Textures in Aluminum, Acta Metall. Mater. 39 (1991) 1377–1404. doi:Doi 10.1016/0956-7151(91)90225-P.
[163] L.P. Kurilekh, Recrystallization behavior of solid solutions of metals, Metalloved. i Term. Obrab. 1 (1959) 35–38. doi:10.1007/BF00813841.
[164] A. Jain, S.P. Ong, G. Hautier, W. Chen, W.D. Richards, S. Dacek, S. Cholia, D. Gunter, D. Skinner, G. Ceder, K.A. Persson, Commentary: The Materials Project: A materials genome approach to accelerating materials innovation, APL Mater. 1 (2013) 011002. doi:10.1063/1.4812323.
[165] V.M. Glazov, G.P. Lazarev, G.A. Korol'kov, The Solubility of Certain Transition Metals in Aluminum, Metalloved. i Term. Obrab. (1959) 51–54.
[166] V.N. Yeremenko, Y. V. Natanzon, V.I. Dybkov, Interaction of the Refractory Metals with Liquid Aluminium, J. Less-Common Met. 50 (1976) 29–48.
[167] J.H. Martin, B.D. Yahata, J.M. Hundley, J.A. Mayer, T.A. Schaedler, T.M. Pollock, 3D printing of high-strength aluminium alloys, Nature. 549 (2017) 365–369. doi:10.1038/nature23894.
[168] E.A. Starke, J.T. Staley, Application of modern aluminum alloys to aircraft, Prog. Aerosp. Sci. 32 (1996) 131–172. doi:10.1016/0376-0421(95)00004-6.
[169] J. Liu, S. Kou, Crack susceptibility of binary aluminum alloys during solidification, Acta Mater. 110 (2016) 84–94. doi:10.1016/j.actamat.2016.03.030.
[170] J.H. Martin, B.D. Yahata, E.C. Clough, R.D. Mone, J.A. Mayer, E. Stonkevitch, R.C. Schubert, J.A. Miller, J.M. Hundley, T.A. Schaedler, T.M. Pollock, Recent advances in additive manufacturing of high strength 7000 series aluminum, Adv. Mater. Process. 176 (2018).
[171] H. Zhang, H. Zhu, T. Qi, Z. Hu, X. Zeng, Selective laser melting of high strength Al-Cu-Mg alloys: Processing, microstructure and mechanical properties, Mater. Sci. Eng. A. 656 (2016) 47–54. doi:10.1016/j.msea.2015.12.101.
[172] N. Coniglio, C.E. Cross, Initiation and growth mechanisms for weld solidification cracking, Int. Mater. Rev. 58 (2013) 375–397. doi:10.1179/1743280413Y.0000000020.
[173] M. Rappaz, J. Drezet, M. Gremaud, A New Hot-Tearing Criterion, 30 (1999) 449–455.
[174] L. Yuan, C. O'Sullivan, C.M. Gourlay, Exploring dendrite coherency with the discrete element method, Acta Mater. 60 (2012) 1334–1345. doi:10.1016/j.actamat.2011.11.042.
[175] K. Schmidtke, F. Palm, A. Hawkins, C. Emmelmann, Process and mechanical properties: Applicability of a scandium modified Al-alloy for laser additive manufacturing, Phys. Procedia. 12 (2011) 369–374. doi:10.1016/j.phpro.2011.03.047.
[176] J.P. Immarigeon, R.T. Holt, A.K. Koul, L. Zhao, W. Wallace, J.C. Beddoes, Lightweight materials for aircraft applications, Mater. Charact. 35 (1995) 41–67. doi:10.1016/1044-5803(95)00066-6.
[177] W.. Miller, L. Zhuang, J. Bottema, a. . Wittebrood, P. De Smet, a Haszler, a Vieregge, Recent development in aluminium alloys for the automotive industry, Mater. Sci. Eng. A. 280 (2000) 37–49. doi:10.1016/S0921-5093(99)00653-X.

[178] Society of Automotive Engineers., American Society for Testing and Materials., Metals and Alloys in the Unified Numbering System (UNS), 12th ed., ASTM International, Warrendale PA, 2012.
[179] C.M. Gourlay, a K. Dahle, Dilatant shear bands in solidifying metals., Nature. 445 (2007) 70–73. doi:10.1038/nature05426.
[180] M.A. Martorano, C. Beckermann, C.-A. Gandin, A solutal interaction mechanism for the columnar-to-equiaxed transition in alloy solidification, Metall. Mater. Trans. A. 34A (2003) 1657–1674. doi:10.1007/s11661-004-0101-0.
[181] D.G. Eskin, Suyitno, L. Katgerman, Mechanical properties in the semi-solid state and hot tearing of aluminium alloys, Prog. Mater. Sci. 49 (2004) 629–711. doi:10.1016/S0079-6425(03)00037-9.
[182] Thermo-Calc TCAL4-TCS Al-based alloy database, (2016).
[183] Concept Laser, CL 30AL / CL 31AL, 12 (2015). http://www.conceptlaserinc.com/wp-content/uploads/2014/10/CL-AL30_31AL_Englisch.pdf.
[184] C.Y. Yu, P.W. Kao, C.P. Chang, Transition of tensile deformation behaviors in ultrafine-grained aluminum, Acta Mater. 53 (2005) 4019–4028. doi:10.1016/j.actamat.2005.05.005.
[185] L. Arnberg, G. Chai, L. Backerud, Determination of dendritic coherency in solidifying melts by rheological measurements, Mater. Sci. Eng. A. 173 (1993) 101–103. doi:10.1016/0921-5093(93)90195-K.
[186] S.P. Narra, R. Cunningham, J. Beuth, A.D. Rollett, Location specific solidification microstructure control in electron beam melting of Ti-6Al-4V, Addit. Manuf. 19 (2018) 160–166. doi:10.1016/j.addma.2017.10.003.
[187] T.B. Sercombe, X. Xu, V.J. Challis, R. Green, S. Yue, Z. Zhang, P.D. Lee, Failure modes in high strength and stiffness to weight scaffolds produced by Selective Laser Melting, Mater. Des. 67 (2015) 501–508. doi:10.1016/j.matdes.2014.10.063.
[188] P. Wang, C. Gammer, F. Brenne, T. Niendorf, J. Eckert, S. Scudino, A heat treatable TiB 2 /Al-3.5Cu-1.5Mg-1Si composite fabricated by selective laser melting: Microstructure, heat treatment and mechanical properties, Compos. Part B Eng. (2018). doi:10.1016/j.compositesb.2018.04.026.
[189] A.L. Greer, A.M. Bunn, A. Tronche, P. V Evans, D.J. Bristow, Modelling of Inoculation of Metallic Melts- Application to Grain Redinement of Aluminum by Al-Ti-B, Acta Mater. 48 (2000) 2823–2835.
[190] J.J. Valencia, Quested P.N, Thermophysical properties, ASM Handb. Cast. 15 (2008) 468–481. doi:10.1361/asmhba0005240.

Appendix

A variety of data was utilized in the calculations for this dissertation. Below are several tables which indicate the values and references used in order to provide some additional background information and data in the event further expansion of this research is attempted.

Table A.1: Values for Pure Aluminum. See Chapter 2 & 4

Quantity	Symbol Used	Value Used	Reference
Heat of Fusion	H_f	9.5 x 10^8 J/m^3	Greer et. al.[189]
Entropy of Fusion	S_f	1.11 x 10^8 J/m^3 K^{-1}	Quested and Greer[88]
Gibbs-Thomson Coefficient	Γ_{sl}	9.12 x 10^{-8} K m	Dantzig and Rappaz[51]
Solid-Liquid Surface Energy	γ_{sl}	0.093 J/m^2	Dantzig and Rappaz[51]
Melting Point	T_m	933 K	Dantzig and Rappaz[51]
Atomic Attachment Frequency	$v_0 p_c$	10^{13} s^{-1}	Dantzig and Rappaz[51]
Heat Capacity	C_p	1180 J/kg K	ASM Handbook[190]
Density	ρ	2.385	ASM Handbook[190]
Molar Volume	V_m	1.138 x 10^{-5} m^3/mol	Dantzig and Rappaz[51]
Thermal Conductivity	k	211 W/m K (Solid) 91 W/m K (Liquid)	ASM Handbook[190]

Table A.2: Values for Aluminum- 3 wt% Copper. See Chapter 2 & 4

Quantity	Symbol Used	Value Used	Reference
Heat of Fusion	H_f	9.5 x 10^8 J/m^3	Greer et. al.[189]
Gibbs-Thomson Coefficient	Γ_{sl}	2.4 x 10^{-7} m K	Dantzig and Rappaz[51]
Melting Point	T_m	922 K	Easton and StJohn[95]
Heat Capacity	C_p	1180 J/kg K	ASM Handbook[190]
Liquidus Slope	$\boldsymbol{m_l}$	-3.4 ℃/wt%	Easton and StJohn[95]
Thermal Diffusivity	$\alpha = k/(C_p * \rho)$	3.3 x 10^{-5} m^2/s	ASM Handbook[190]
Diffusion Velocity	V_D	6.7 m/s	Smith and Aziz[84]
Diffusivity	D	4.4 x 10^{-9} m^2/s	Smith and Aziz[84]
Equilibrium Partition Coefficient	k_0	0.17	Easton and StJohn[95]

Table A.3: Values for Al-7075 CET Calculation. See Chapter 2

Quantity	Symbol Used	Value Used	Reference
Growth Restriction Factor	$Q = C_0 m(k-1)$	20.4	Easton and StJohn[78]
Gibbs-Thomson Coefficient	Γ_{sl}	5 x 10^{-8} ℃ m	Approximation from Multiple Sources[51,82,83]
Diffusivity	D	5 x 10^{-9} m^2/s	Approximation from Multiple Sources[79–81]

Table A.4: Values Used in the Aluminum – Tantalum Dissolution[166]. See Chapter 4

Quantity	Symbol Used	Value Used
Arrhenius Equation Parameters for Dissolution Rate	k_0	1.48*10^3 m/s
	E_k	28 kJ/mol

Table A.5: Values for Calculation of Binary Aluminum Alloy Systems[95,153]**.** See Chapters 2-5 where values are either explicitly used or could be applied for additional analysis. Diffusivities are in liquid aluminum and it should be noted that in all cases presented they are within one order of magnitude of each other.

Element	k_0	m_l	Max Concentration (wt%)	Diffusivity at 923K (m^2s^{-1})
Ti	9	30.7	0.15	3.79×10^{-9}
Ta	2.5	70	0.1	Not Available
V	4	10	0.1	Not Available
Hf	2.4	8	0.5	Not Available
Mo	2.5	5	0.1	Not Available
Zr	2.5	4.5	0.11	Not Available
Nb	1.5	13.3	0.15	Not Available
Si	0.11	-6.6	12.6	2.69×10^{-9}
Cr	2.0	3.5	0.4	3.52×10^{-9}
Ni	0.007	-3.3	6	Not Available
Mg	0.51	-6.2	3.4	8.78×10^{-9}
Fe	0.02	-3	1.8	2.45×10^{-9}
Cu	0.17	-3.4	33.2	4.65×10^{-9}
Mn	0.94	-1.6	1.9	3.40×10^{-9}
Zn	~0.3	-2.5	95	2.84×10^{-9}